Electronic Properties of sp^2 Carbon Networks with Defects and Interfaces

Mina Maruyama

February 2017

Electronic Properties of sp^2 Carbon Networks with Defects and Interfaces

Mina Maruyama
Doctoral Program in Nano-Science and Nano-Technology

Submitted to the Graduate School of
Pure and Applied Sciences
in Partial Fulfillment of the Requirements
for the Degree of Doctor of Philosophy in
Science

at the
University of Tsukuba

Abstract

Graphene maintains premier position in the field of nanoscience and nanotechnology because of its simple geometric structure, which allows graphene a precursor for various nanoscale derivatives being applicable for future electronic devices by attaching and implanting imperfections in its hexagonal network. Imperfections, for instance, edges, defects, and interfaces, lead to various topological networks, resulting in interesting electronic properties which are absent in bulk graphene. Theoretical and experimental works corroborated that the strong correlation between the geometric and electronic properties of these two-dimensional sp^2 carbon networks. In this thesis, we aim to design and investigate novel two-dimensional carbon networks consisting of sp^2 carbon atoms which results in unusual electronic structures by first-principles total-energy calculations based on density functional theory.

We investigate geometric and electronic structures of a two-dimensional stable carbon allotrope consisting of pentagonal rings. We found that the sp^2 carbon sheet has a slightly higher total energy than C_{60} and retains its planar structure up to 1000 K, indicating that the sheet is both energetically and kinetically stable. The electronic structure of the sheet is found to be a metal with a flat dispersion band at the Fermi level, leading to spin polarization on the sheet. The polarized electron spin is ferromagnetically aligned and extends throughout the sheet with a spin moment of 0.62 μ_B/nm^2.

We investigate the geometric and electronic structures of porous graphene networks consisting of phenalenyl and phenyl groups, which are connected alternately with C_3 symmetry via single bonds to form a honeycomb network. The networks possess both Dirac cones and Kagome flat bands near the Fermi level because the phenalenyl and phenyl form hexagonal and Kagome lattices, respectively. Because of the large spacing between phenalenyl units, the networks possess very slow massless electrons/holes at the Fermi level, the Fermi velocity of which is a hundred times lower than that of graphene, leading to spin polarization on the networks with antiferromagnetic and ferromagnetic ordering as their stable states. Our calculations show the antiferromagnetic state is the ground state whose energy is lower by 14 meV than that of the ferromagnetic state. We also demonstrate that the electronic structure of the two-dimensional networks is sensitive to the rotation of the phenyl unit connecting phenalenyl units.

We study the energetics and magnetic properties of two graphene dots with triangular shapes embedded in an h-BN sheet. Our first-principles total-energy calculations show that the graphene dots in h-BN prefer the closest inter-dot spacing as their ground state arrangement. Furthermore, total energy of the heterosheet monotonically increases with increasing inter-dot spacing and immediately saturates at

0.21 and 0.12 eV for NC and BC borders, respectively, at the inter-dot spacing of 7.5 Å. We also find that ferrimagnetic spin polarization occurs on each graphene dot with $S = 1/2$ magnetic moment, which are aligned in singlet and triplet arrangement between two dots under inter-dot spacings of 5.0 Å or larger. The spin polarization energy saturates at approximately 100 meV per graphene dot at an inter-dot spacing of 8.0 Å. The spin–spin interaction J prefers an antiparallel spin coupling to a parallel one with an energy of 25 meV at an inter-dot spacing of 5.0 Å.

Contents

Chapter 1

Introduction

Carbon atom are known to form three orbital hybridizations, sp, sp^2, and sp^3, leading to various in its covalent bonds [Figure 1.1]. Accordingly, carbon possesses various allotropes which cover all dimensionality with metallic or insulating properties depending on their orbital hybrization. For instance, carbyne, graphite, and diamond are representative allotropes consisting of C atoms with sp, sp^2, and sp^3 hybridizations, respectively [Figure 1.2]. Graphite has a stacked layered structure of honeycomb sheets consisting of C atoms. Each C atom is connected to three adjacent atoms via σ covalent bond with a length of 1.42 Å and angle of 120° forming two-dimensional (2D) network. On the other hand, π states are distributed normal to the layer and are weakly overlap within and between layers, inducing a metallic electronic structure of graphite [Figure 1.3] [1]. In contrast to graphite, diamond is an insulator with a bandgap of 5.5 eV and a hard material with 10 Mohs. These electronical and mechanical properties are ascribed to its three-dimensional network of tetrahedrally, bonded C with sp^3 hybridization.

Structural flexibility of covalent bonds of C atoms allows us to have other allotropes. Figure 1.4 shows representative examples of novel carbon allotropes with nanoscale sizes. In 1985, Kroto, Smalley, and Curl have predicted the presence of hollow-cage carbon cluster, fullerene, in mass spectra of carbon cluster, in which they observed remarkable peak at the cluster size of 60 [2]. By combing the experimental fact and the structure of a soccer ball, they deduced the C_{60} cluster consisting of 12 pentagonal and 20 hexagonal rings with I_h symmetry. Following the macroscopic production of C_{60} and other large fullerenes, the I_h cage structure of C_{60} has been confirmed [3]. Soon later, in 1992, Iijima has discovered tubular forms of graphitic carbon with nanometer diameter (carbon nanotube: CNT) using transmission electron microscope [4]. In the case, owing to the boundary condition imposed on the electronic structure of monolayer graphite, CNT is either a metal or semiconductor depending on their atomic arrangement along its circumference [5, 6]. Furthermore, in 2004, graphene, a constituent atomic layer of graphite, has been exfoliated from bulk graphite by Novoselov and Geim [7, 8]. As has been already mentioned, the graphene has a pair of linear dispersion bands at the Fermi level (E_F) and K point due to their hexagonal atomic layer network [Figure 1.5]. Following the discoveries and synthesis of these novel carbon allotropes, they have been attracting much attention in both basic and applied sciences for the last three decades.

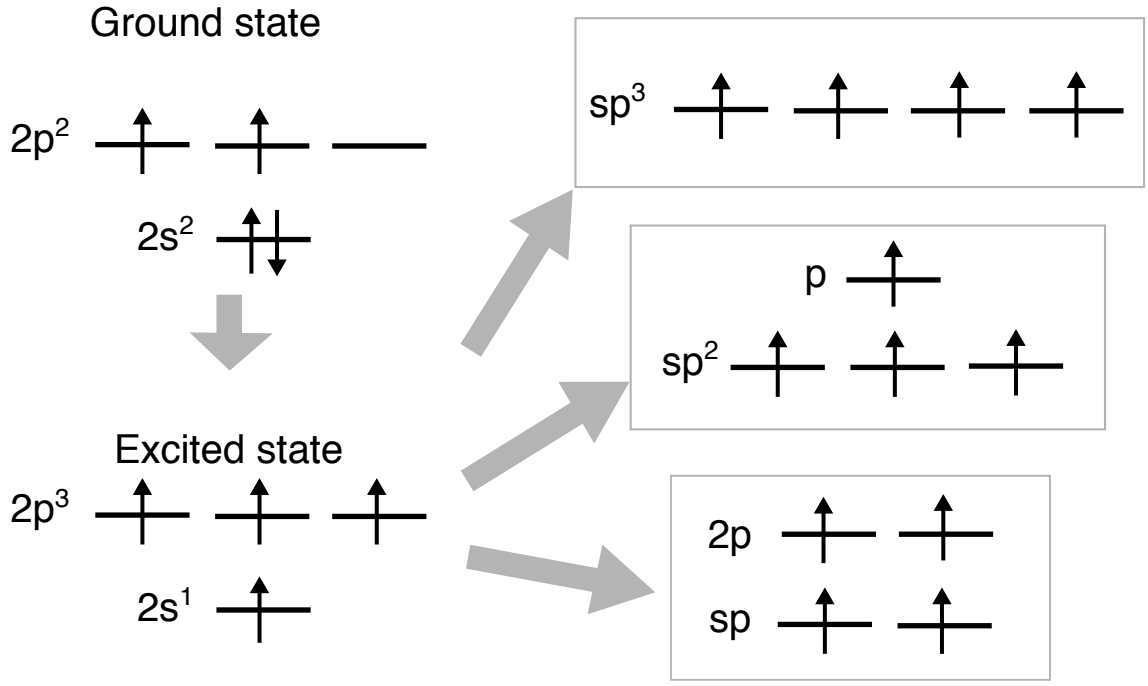

Figure 1.1: Electronic configurations of carbon.

Among these three novel carbon nanoallotropes, graphene is now keeping premier position in the field of nanoscience and nanotechnology because of its simple geometric structure, which allows graphene a precursor for various nanoscale derivatives being applicable for future electronic devices by attaching and implanting imperfections in its hexagonal network. By cutting the graphene along particular direction, we can construct the graphene ribbons with nanometer width (GNR) [Figure 1.6]. In the case, the energetics and electronic structure of the GNRs are sensitive to their width and edge atomic arrangement [9]. GNRs with armchair edge become semiconductors of which band gap asymptotically decreases with increasing their widths [10]. In addition, GNR with zigzag edges possesses flat dispersion bands at E_F and around the zone boundary, which are split into upper and lower branches under the infinitesimal on-site Coulomb interaction U, leading to the spin polarization near the edge atomic sites [11, 12]. These flat band states are known to be the edge states which are induced by the delicate balance among the π electron transfer near the edge atomic sites.

By imposing an additional open boundary condition normal to the ribbon direction on GNR, we can get graphene nanoflakes or hydrocarbon molecules. The electronic structure of the graphene nanoflake also depend on its flake size and shape. The molecules are ranging from the closed shell electronic structure to the open shell electronic structure with radical spins. The energies of small graphene nanoflakes or hydrocarbon molecules can be determined using the empirical procedure which is known to be the Huckel's rule: The hydrocarbon molecules containing $4k + 2$ C atoms are energetically stable where k is integer numbers. These molecules basically possess the finite energy gap between highest occupied (HO) and lowest unoccupied (LU) states, which is inversely proportional to the size of the molecule, although the

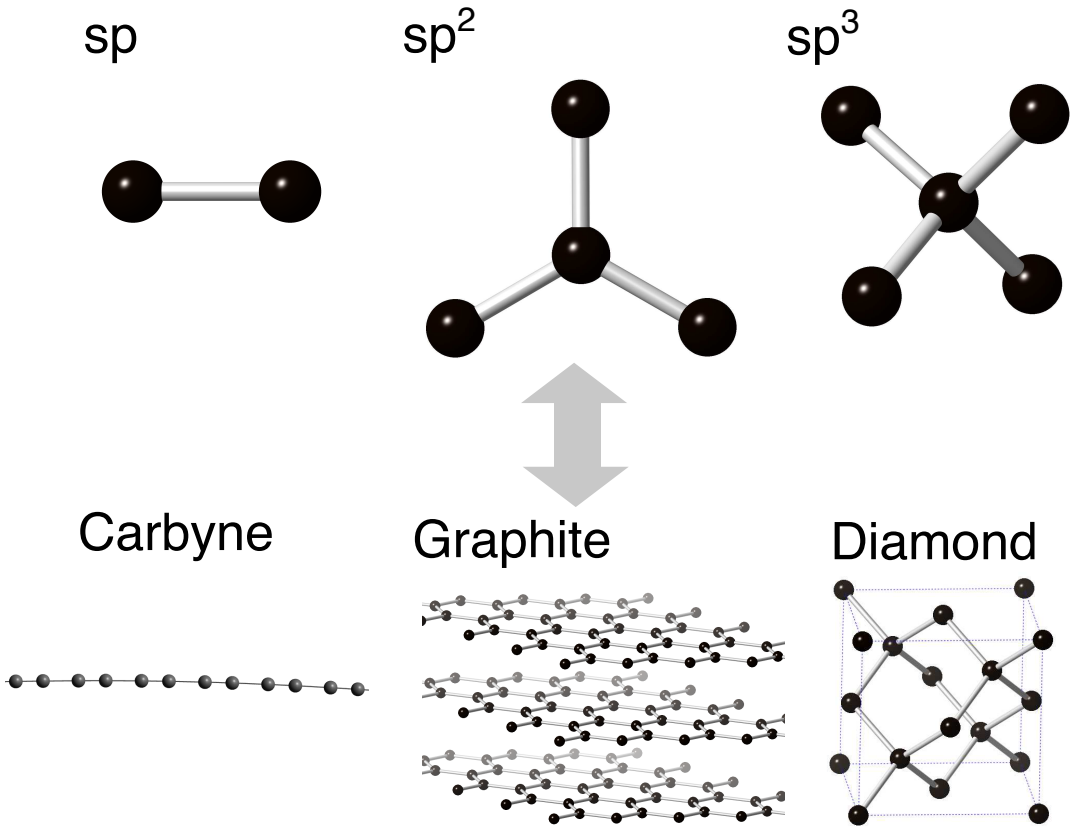

Figure 1.2: sp, sp^2, and sp^3 hybridized covalent bonds and carbon allotropes consisting of their bonds, respectively.

detailed electronic structure depends on their C-C network topology. On the other hand, the hydrocarbon molecules with triangular shape occasionally possess open-shell electronic structures possessing the number of half-filled zero energy modes with non-bonding nature associated with the sublattice imbalance of their networks [Figure 1.8] [13, 14]. For instance, phenalenyl is the smallest example of the hydrocarbon molecule with radical spin. It should be noted that these open shell graphene nanoflake are energetically unstable due to the partially filled electron state at E_F, causing to the large electron energy.

In addition to the periodic and open boundary conditions, the topological defects and interfaces with other 2D materials also terminate or modulate the π electron networks of the GNRs or graphene nanoflakes as the other possible boundary conditions on the sp^2 C networks [Figure 1.9] [15]. The topological line defects consisting of octagonal and a pair of pentagonal rings can terminate the π electron states near E_F leading to the localized state around the topological line defect as in the case of edge state in the GNR with zigzag edges. The topological defect is inherent in the domains boundary of the polycrystalline graphene experimentally synthesized [Figure 1.10] [16]. Interfaces between graphene and other layered materials also act as the open boundary condition on the graphitic π network. Early theoretical calculations demonstrated that the electronic structure of the interface between graphene and hexagonal boron nitride (h-BN), which is honeycomb sheet consisting

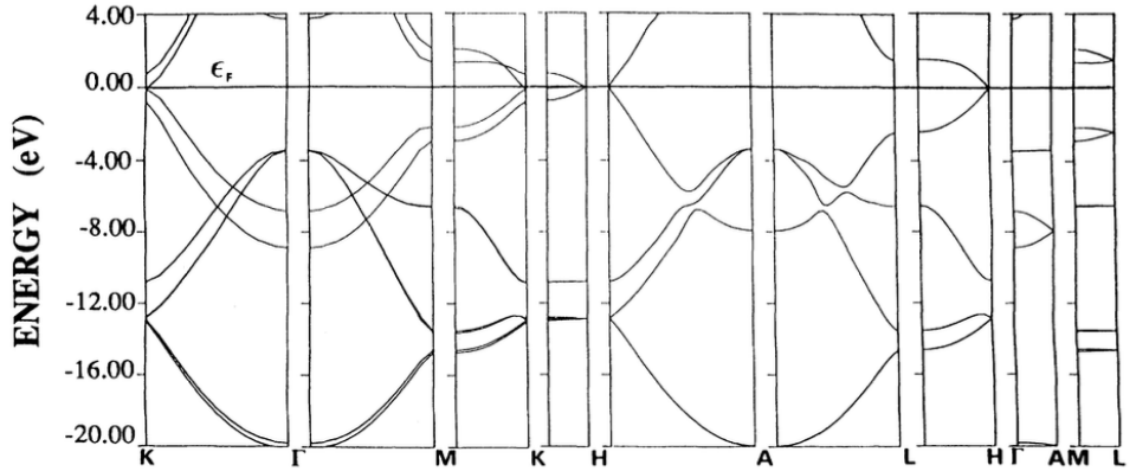

Figure 1.3: Electronic structures of graphite [1]. The energy is measured from that of the Fermi level.

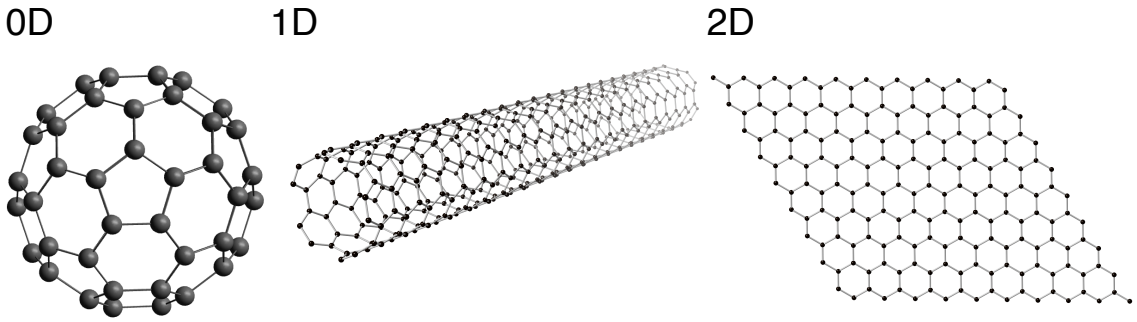

Figure 1.4: Geometric structures of fullerene, carbon nanotube, and graphene.

of boron and nitrogen with bond length of about 1.44 Å, depends on the detailed atomic arrangement at the interfaces: Interfaces with zigzag arrangement leads to the interface localized states near E_F with bonding and antibonding character of C and B/N atoms [Figure 1.11] [17]. In contrast, the localized state is absent at the interface with armchair shape. Furthermore, by designing the interface morphology, the graphene domains exhibit the spin polarization as in the cases of the graphene nanoflakes with sublattice imbalance or GNR with zigzag edges. Besides the foreign 2D materials, nanoscale vacancies also act as the boundary condition on the graphitic π networks of carbon, leading to the peculiar electron states at E_F, such as an isolated flat band state or the Kagome's flat band states at or near E_F [Figure 1.12] [18].

This thesis contains three following studies about electronic properties of graphene with topological defects, vacancies, and interfaces. Before showing our calculations, in chapter 2, we review calculation methods used in this thesis. We will show the geometric and electronic structure of a 2D carbon allotrope consisting of pentagonal rings in chapter 3. The 2D networks consisting of fused pentagonal rings is a metal with the flat dispersion band in the part of the 2D Brillouin zone leading to the ferromagnetic spin ordering throughout the sheet. We demonstrate the 2D

hydrocarbon network consisting of phenalenyl and phenyl which are alternately arranged with C_3 symmetry in chapter 4. The 2D hydrocarbon sheet possesses both Dirac cones and Kagome's flat bands near E_F, which are originated from the nonbonding states of the hexagonally arranged phenalenyl units and the HO state of the phenyl forming the Kagome lattice, respectively. Furthermore, the 2D hydrocarbon network also possesses spin polarization localized on the phenalenyl units. In chapter 5, we present the energetics and magnetic properties of two graphene dots (phenalenyl shape domain) embedded into a h-BN sheet. We found that ferrimagnetic spin polarization occurs on each graphene dot aligned in singlet and triplet arrangements between two dots with the short-range spin-spin interaction J. Finally, we summarized this thesis in chapter 6.

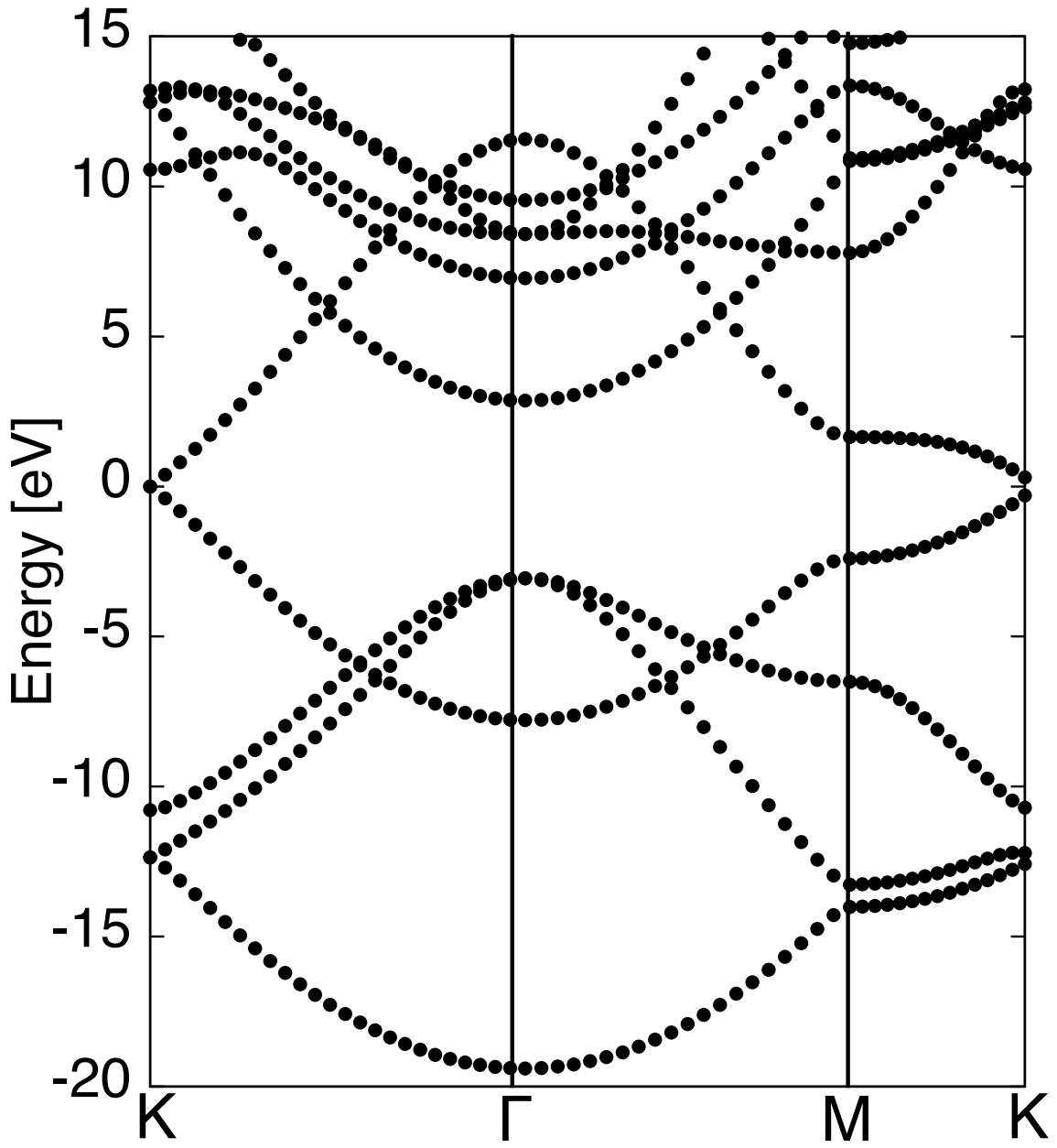

Figure 1.5: Electronic structure of graphene. The energy is measured from that of the Fermi level.

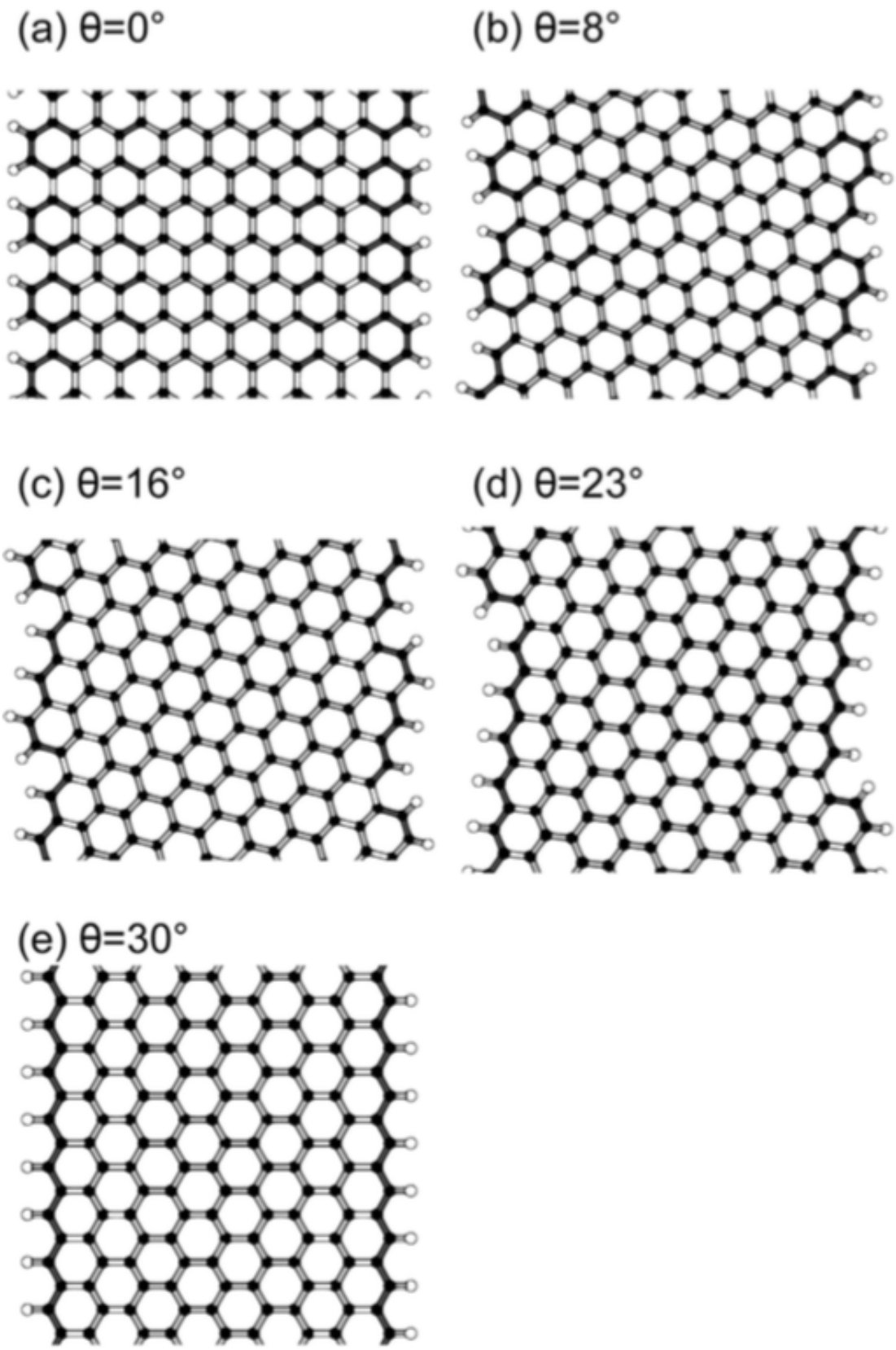

Figure 1.6: Geometric structures of graphene nanoribbon with edge angles of (a) 0° (armchair edge), (b) 8°, (c) 16°, (d) 23°, and (e) 30° (zigzag edge) [9].

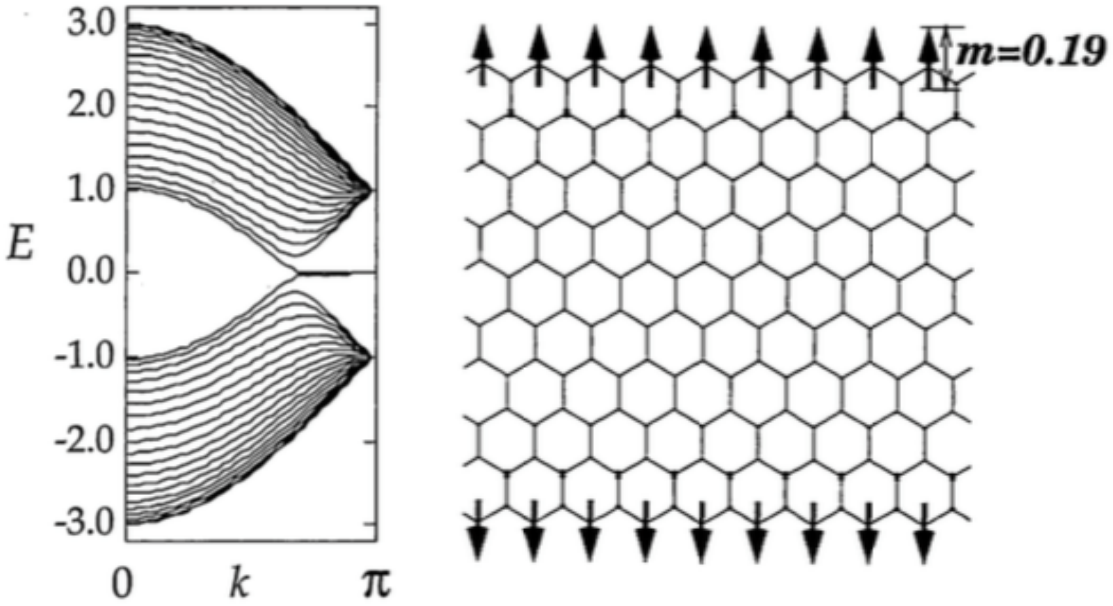

Figure 1.7: Electronic structure and spin moment of a graphene nanoribbon with zigzag edges. The energy is measured from that of the Fermi level [11].

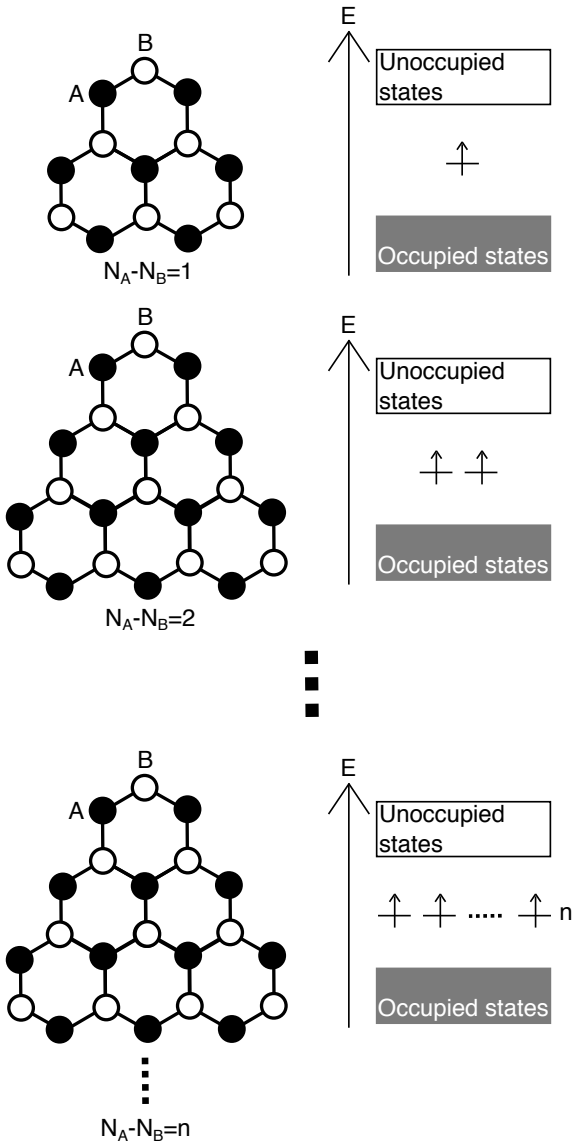

Figure 1.8: Schematic pictures of geometries and energy levels of triangular graphene flakes.

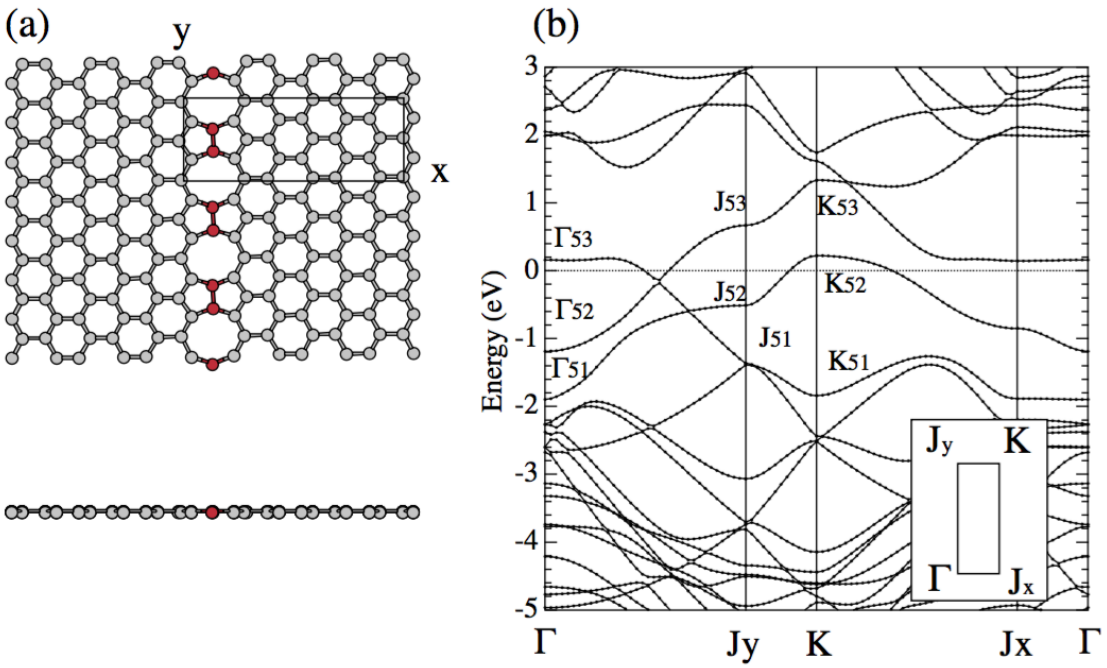

Figure 1.9: (a) Geometric and (b) electronic structures of graphene with topological line defect consisting of pentagonal and octagonal rings [15]. The energy is measured from that of the Fermi level.

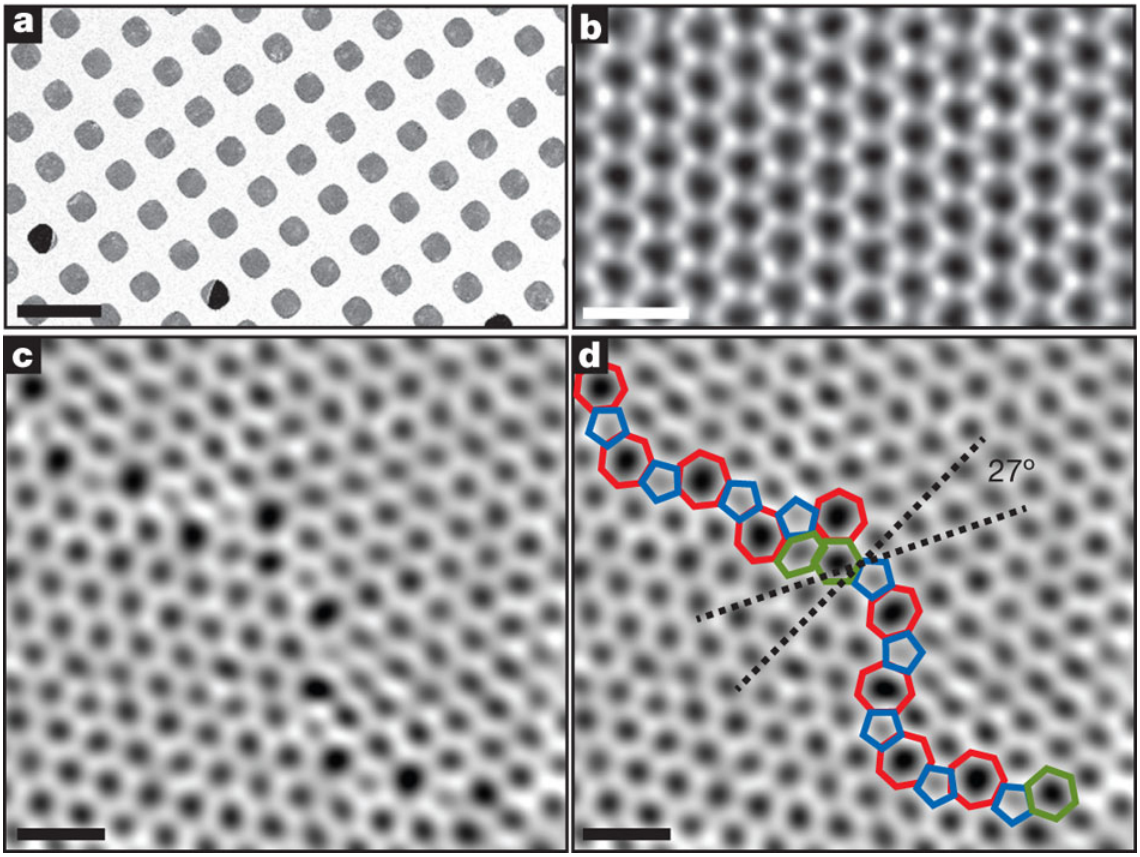

Figure 1.10: Scanning electron microscope images of graphene with grain boundary [16].

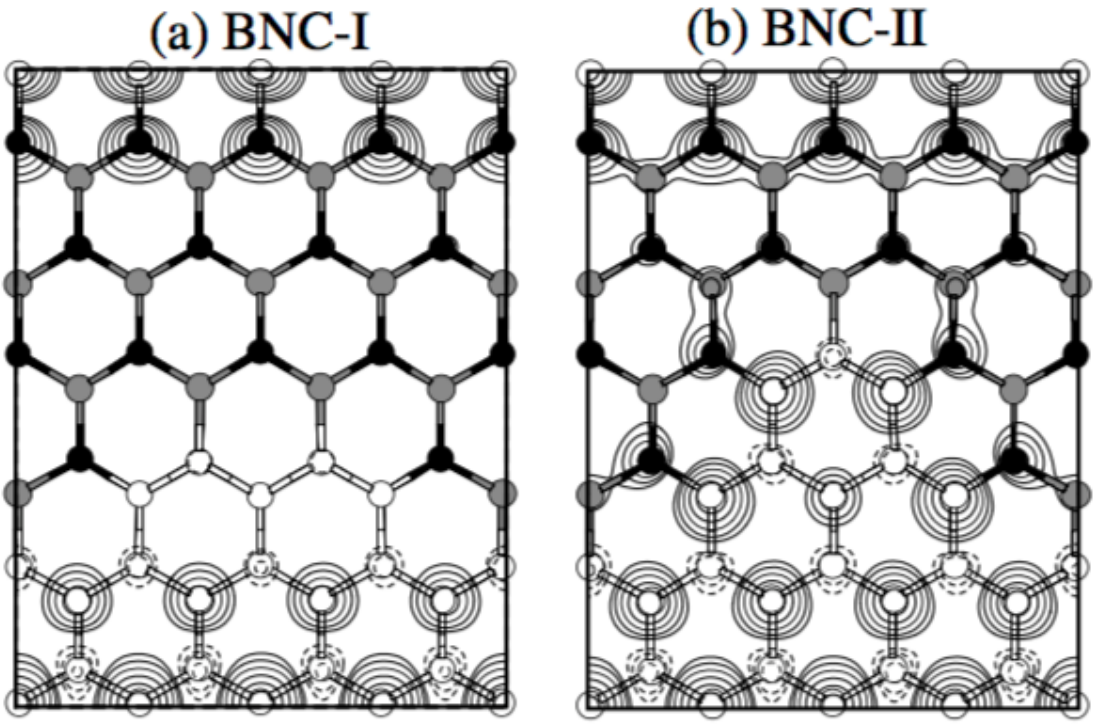

Figure 1.11: Contour plots of spin densities of heterosheet consisting of graphene and h-BN [17]. White, black, and gray balls denote carbon, nitrogen, and boron atoms, respectively.

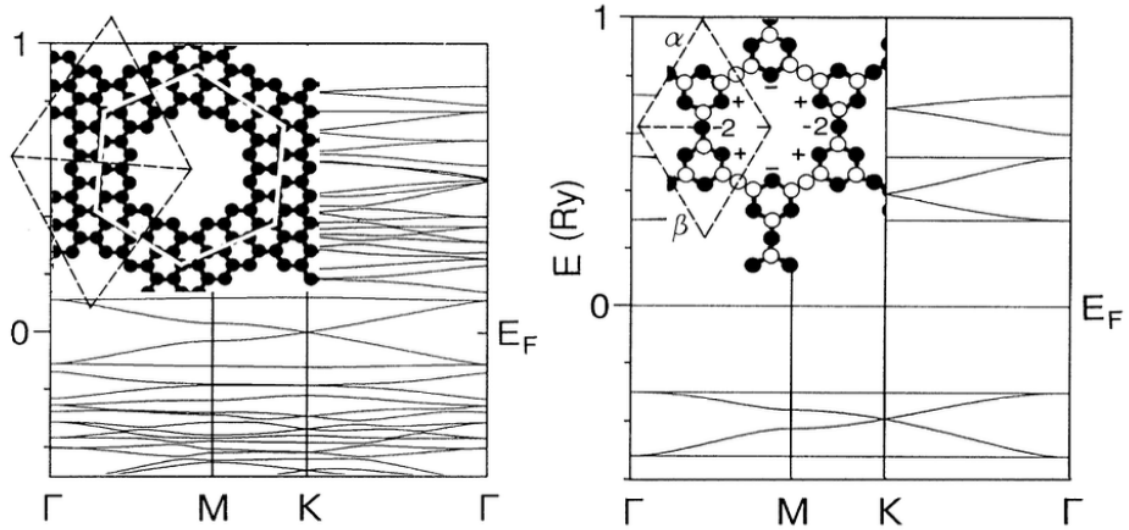

Figure 1.12: Geometric and electronic structures of porous graphene networks [18]. The energy is measured from that of the Fermi level.

Chapter 2

Calculation Method

In this chapter, we present calculation methods used in this thesis. All calculations were performed using the density functional theory. This chapter is organized as follows. In section 2.1, we describe the density functional theory. To adopt the density functional theory for the crystals, Bloch's theorem is briefly described in section 2.2. Plane wave basis set is described in section 2.3. To described interaction between electrons and nuclei, we use pseudopotential procedure which is explained in section 2.4. In the section 2.5, we describe the effective screening medium method to calculate the materials under the electric field within the density functional theory with plane wave method.

2.1 Density functional theory

The most widely used theory in the modern electronic structure calculations (with the simultaneous atomic-geometry optimization) is the density functional theory (DFT). The DFT is a principle theory of the electronic structures of atoms, molecules, and solids in their ground states, which are described using the electron density distribution $n(\mathbf{r})$ (Hohenberg and Kohn in 1964 [19] and Kohn and Sham in 1965 [20]). In this section, we describe two theorems, and derive self-consistent equations based on these two theorems. Approximations adopted in the equations are also explained in this section.

2.1.1 Hohenberg-Kohn theorems

The hamiltonian of N-electrons system,

$$\begin{aligned}
\mathcal{H} &= T + U + V && (2.1)\\
&= \sum_{i=1}^{N}\left(-\frac{\hbar}{2m}\nabla_i^2\right) + \frac{1}{2}\sum_{i\neq j}^{N}\frac{e^2}{|\mathbf{r}_i - \mathbf{r}_j|} + \sum_{i=1}^{N} v(\mathbf{r}_i) && (2.2)\\
T &= \sum_{i=1}^{N}\left(-\frac{\hbar}{2m}\nabla_i^2\right) && (2.3)\\
U &= \frac{1}{2}\sum_{i\neq j}^{N}\frac{e^2}{|\mathbf{r}_i - \mathbf{r}_j|} && (2.4)\\
V &= \sum_{i=1}^{N} v(\mathbf{r}_i) && (2.5)
\end{aligned}$$

is corresponded to Schrödinger equation of

$$\mathcal{H}\Psi(\mathbf{r}_1, \cdots, \mathbf{r}_N) = E\Psi(\mathbf{r}_1, \cdots, \mathbf{r}_N). \quad (2.6)$$

For solving the Schrödinger equation, electronic density $n(\mathbf{r})$ can be written

$$\begin{aligned}
n(\mathbf{r}) &= (\Psi, \hat{n}\Psi) && (2.7)\\
&= \int \Psi^*(\mathbf{r}_1, \cdots, \mathbf{r}_N)\hat{n}(\mathbf{r})\Psi(\mathbf{r}_1, \cdots, \mathbf{r}_N)d\mathbf{r}_1 \cdots d\mathbf{r}_N && (2.8)
\end{aligned}$$

where

$$\hat{n}(\mathbf{r}) = \sum_{i-1}^{N}\delta(\mathbf{r} - \mathbf{r}_i). \quad (2.9)$$

By using the $n(\mathbf{r})$, an expectation of V can be written

$$\begin{aligned}
(\Psi, V\Psi) &= \int \Psi^*\left[\sum_{i=1}^{N} v(\mathbf{r}_i)\right]\Psi d\mathbf{r}_1 \cdots d\mathbf{r}_N && (2.10)\\
&= \int \Psi^*\left[\int \sum_{i=1}^{N} v(\mathbf{r})\delta(\mathbf{r} - \mathbf{r}_i)d\mathbf{r}\right]\Psi d\mathbf{r}_1 \cdots d\mathbf{r}_N && (2.11)\\
&= \int v(\mathbf{r})n(\mathbf{r})d\mathbf{r}. && (2.12)
\end{aligned}$$

Kohn-Sham theorems are presented by using these premises following. In the DFT, for an interacting N-electron system, the ground state density $n(\mathbf{r})$ uniquely correspond to an external field $v(\mathbf{r})$:

$$v(\mathbf{r}) \Leftrightarrow n(\mathbf{r}). \quad (2.13)$$

This is true whether the ground state is non-degenerate or degenerate (In the latter case any of the possible ground state densities uniquely determines the potential $v(\mathbf{r})$). (First, the proof for non-degenerate ground states will be presented:)

Let $v(\mathbf{r})$ be the external potential of the system associated with ground state density $n(\mathbf{r})$, total number of particles $N = \int n(\mathbf{r})d\mathbf{r}$, Hamiltonian $\mathcal{H}$ and ground state Ψ and energy E,

$$v : \mathcal{H}, N, n(\mathbf{r}), \Psi, E. \tag{2.14}$$

Similarly, we consider a second system of v with

$$v' : \mathcal{H}', N', n'(\mathbf{r}), \Psi', E' \tag{2.15}$$

where $v' \neq v+C$ and $\Psi' \neq \Psi$. Then, by using the Rayleigh-Ritz variational principle

$$\begin{aligned} E = (\Psi, \mathcal{H}\Psi) &< (\Psi', \mathcal{H}\Psi') && (2.16)\\ &= (\Psi', (\mathcal{H}' - V' + V)\Psi') && (2.17)\\ &= E' + \int [v(\mathbf{r}) - v'(\mathbf{r})]n(\mathbf{r})d\mathbf{r} && (2.18) \end{aligned}$$

or

$$E < E' + \int [v(\mathbf{r}) - v'(\mathbf{r})]n'(\mathbf{r})d\mathbf{r}. \tag{2.19}$$

The inequality follows from the fact that $\Psi' \neq \Psi$. Similarly,

$$E' < E + \int [v'(\mathbf{r}) - v(\mathbf{r})]n(\mathbf{r})d\mathbf{r}. \tag{2.20}$$

Adding the inequalities Eqs.(2.19) and (2.20) gives

$$(E + E') < (E + E') + \int [v(\mathbf{r}) - v'(\mathbf{r})][n'(\mathbf{r}) - n(\mathbf{r})]d\mathbf{r}. \tag{2.21}$$

The possibility $n'(\mathbf{r}) \equiv n(\mathbf{r})$ is excluded since Eq.(2.21) would result in $0 < 0$. Thus any potential $v'(\mathbf{r})$ except $v(\mathbf{r}) + c$, lead to an $n'(\mathbf{r}) \not\equiv n(\mathbf{r})$.

Since $n(\mathbf{r})$ determines $v(\mathbf{r})$ and N, it determines $\mathcal{H}$; hence, implicitly, also all properties derivable from $\mathcal{H}$, such as the many electron ground state wave function $\Psi(\mathbf{r}_1 \cdots \mathbf{r}_N)$ and energy E, excited state wave functions and energies, Green's functions etc.

The total ground state energy of a system can be written as

$$E = (\Psi, V\Psi) + (\Psi, (T + U)\Psi) \tag{2.22}$$

where the terms on the right hand side are the expectation values of the external potential, kinetic energy, and interaction energy operators. Clearly

$$(\Psi, V\Psi) = \int v(\mathbf{r})n(\mathbf{r})d\mathbf{r} \tag{2.23}$$

while the quantity

$$F[n] \equiv (\Psi, (T+U)\Psi) \tag{2.24}$$

is a functional of $n(\mathbf{r})$. Thus, E is written as,

$$E \equiv E_{v(\mathbf{r})}[n(\mathbf{r})] \equiv \int v(\mathbf{r})n(\mathbf{r})d\mathbf{r} + F[n(\mathbf{r})]. \tag{2.25}$$

Using the Rayleigh-Ritz principle for the ground state energy leads to the conclusion that, for a given $v(\mathbf{r})$, the expression Eq.(2.25) is a minimum for the correct ground state density $n(\mathbf{r})$:

Let Ψ' be a non degenerated trial state with energy E_0. Then, by the conventional Rayleigh-Ritz principle,

$$E[\Psi'] \equiv (\Psi', (T+V+U)\Psi') \geq E_0 \tag{2.26}$$

or

$$E_v[n'(\mathbf{r})] \equiv \int v(\mathbf{r})n'(\mathbf{r})d\mathbf{r} + F[n'(\mathbf{r})] \geq E_0 \tag{2.27}$$

The equality sign holds only if $\Psi' = \Psi$. This is the Hohenberg-Kohn energy variational principle.

The proof can be extended to degenerate ground states, leading again to Eq.(2.27). The equality is now obtained for any $n'(\mathbf{r})$ of one of the many ground states. By the conventional Rayleigh-Ritz principle, we have

$$E_0 = \min_{\psi'}(\Psi', \mathcal{H}\Psi'). \tag{2.28}$$

We now sort all trial functions into classes according to the densities $n'(\mathbf{r})$ to which they give rise. We then minimize in two stages

$$E_0 \equiv \min_{n'(\mathbf{r})} \min_{\Psi'(n'[\Psi']=n'(\mathbf{r}))}(\Psi', \mathcal{H}\Psi') \tag{2.29}$$

$$= \min_{n'(\mathbf{r})} \left[\int v(\mathbf{r})n'(\mathbf{r})d\mathbf{r} + F[n'(\mathbf{r})] \right], \tag{2.30}$$

where

$$F[n'(\mathbf{r})] \equiv \min\Psi'(n'[\Psi'] = n'(\mathbf{r}))(\Psi', (T+U)\Psi'), \tag{2.31}$$

i.e. $F[n'(\mathbf{r})]$ is the minimum subject to the constraint $n[\Psi'] = n'(\mathbf{r})$. Note that the definition of $F[n'(\mathbf{r})]$ applies only to densities which are ground state densities, while the definition Eq.(2.31) pertains to a broader class of densities. Further, degenerate states are automatically covered. Thus if the functional $F[n(\mathbf{r})]$ is known with sufficient accuracy, the ground state energy and density for any electronic system, no matter the number of electrons, can be determined by minimizing Eq.(2.27) with respect to the three-dimensional $n'(\mathbf{r})$. (The crudest Ansatz for $F[n(\mathbf{r})]$ gives the familiar Thomas-Fermi approximation.)

2.1.2 Kohn-Sham equation

The functional $F[n]$ represents the kinetic and interaction energies. It is advantageous to write it as

$$F[n] \equiv T_s[n] + \frac{1}{2}\int \frac{n(\mathbf{r})n(\mathbf{r}')}{|\mathbf{r}-\mathbf{r}'|}d\mathbf{r}d\mathbf{r}' + E_{xc}, \tag{2.32}$$

where $T_s[n]$ is the kinetic energy of non-interacting electrons of density $n(\mathbf{r})$, the next term is the classical electron-electron interaction energy, and $E_{xc}[n]$ is the remaining part of $F[n]$. Eq.(2.21) lead to the Kohn-Sham self-consistent equations,

$$\left[-\frac{\hbar^2}{2m}\nabla^2 + v(\mathbf{r}) + \int \frac{n(\mathbf{r}')}{|\mathbf{r}-\mathbf{r}'}d\mathbf{r}' + v_{xc}(\mathbf{r})\right]\varphi_j(\mathbf{r}) = \epsilon_j\varphi_j(\mathbf{r}) \tag{2.33}$$

where

$$v_{xc}(\mathbf{r}) \equiv \frac{\delta E_{xc}[n(\mathbf{r})]}{\delta n(\mathbf{r})} \tag{2.34}$$

and

$$n(\mathbf{r}) = \sum_1^N |\varphi_j(\mathbf{r})|.^2 \tag{2.35}$$

The total energy is

$$E = \sum_{j=1}^N \epsilon_j - \frac{1}{2}\int \frac{n(\mathbf{r})n(\mathbf{r}')}{|\mathbf{r}-\mathbf{r}'|}d\mathbf{r}d\mathbf{r}' - \int v(\mathbf{r})n(\mathbf{r})d\mathbf{r} + E_{xc}[n(\mathbf{r})] \tag{2.36}$$

In principle, if the exact $E_{xc}[n]$ were used in these equations, the resulting self-consistent density $n(\mathbf{r})$ and energy E would be exact, including all many body effects. Of course, in practical application, one must content oneself with approximations for E_{xc}. Figure 2.1 shows each step to solve the Kohn-Sham equation. The first step is to chose an initial structure of the system and its charge density $n_{in}(\mathbf{r})$. Then, by using the initial charge density, we evaluate the v_{eff} and solve the Kohn-Sham equation. Finally, we generate the n_{in} by a new charge density n_{out} and repeat the same procedure until $n_{in} = n_{out}$.

2.1.3 Local density approximation

The Hohenberg-Kohn theorem provides some motivation for using approximate methods to describe the exchange-correlation energy as a function of the electron density. The simplest method for describing the exchange-correlation energy of interacting electron systems is to use the local density approximation (LDA). The LDA is widely used in total-energy calculations [21, 22]. In the LDA, the exchange-correlation energy of the electron system is constructed by assuming that the exchange-correlation energy per electron at a point $\mathbf{r}$ in the electron gas $\varepsilon_{xc}(\mathbf{r})$

is equal to the exchange-correlation energy per electron in a homogeneous electron gas ε_{xc}^{hom} that has the same density as the electron gas at point $\mathbf{r}$. Thus

$$E_{xc}[n(\mathbf{r})] = \int \varepsilon_{xc}[n(\mathbf{r})]n(\mathbf{r})d\mathbf{r} \tag{2.37}$$

and

$$\frac{\delta E_{xc}[n(\mathbf{r})]}{\delta n(\mathbf{r})} = \frac{\delta[n(\mathbf{r})\varepsilon_{xc}(\mathbf{r})]}{\delta n(\mathbf{r})} \tag{2.38}$$

with

$$\varepsilon_{xc}(\mathbf{r}) = \varepsilon_{xc}^{hom}[n(\mathbf{r})]. \tag{2.39}$$

The LDA assumes that the exchange-correlation energy functional is local.

2.1.4 Generalized gradient approximation

The LDA has been used successfully in solid state physics: The ground state properties of atoms, molecules, and solids agree with these obtained by experiments. In addition, functional forms for the exchange-correlation energy including an additional information about the electron gas of slowly varying density have been developed. In these functional forms called "generalized gradient approximation (GGA)", the effects of the charge gradient $\nabla n(\mathbf{r})$ are included [23]. The exchange correlation functional $E_{xc}[n(\mathbf{r})]$ of the GGA is with the form

$$E_{xc}[n(\mathbf{r})] = \int f(n(\mathbf{r}), \nabla n(\mathbf{r}))d\mathbf{r} \tag{2.40}$$

This semilocal functional has improved results obtained by the LDA: In comparison with the LDA, the GGA tend to improve the total energies, atomization energies, and geometric structure. In this thesis, we use a functional form parameterized by Perdew, Burke, and Ernzerhof (GGA-PBE).

2.1.5 Spin density functional theory

Under the external magnetic field, atoms, molecules, and solids possess Zeeman energy between magnetization densities $m(\mathbf{r})$ depended on external magnetic field and electron spin. The energy of these systems can be written by electron density, $n(\mathbf{r})$, and additional magnetization density $m(\mathbf{r})$. We separate the density n into that of αspin $n_\alpha(\mathbf{r})$ and β spin densities $n_\beta(\mathbf{r})$. By tacking into account of the spin degree of freedom, Kohn-Sham equation is written as

$$\left[-\frac{1}{2}\nabla^2 + v_{ext,\sigma}(\mathbf{r}) + \int \frac{n(\mathbf{r}')}{|\mathbf{r}-\mathbf{r}'|}d\mathbf{r}' + \frac{\delta E_{xc}[n_\alpha, n_\beta]}{\delta n_\sigma(\mathbf{r})}\right]\phi_{i\sigma}(\mathbf{r}) \equiv \epsilon_{i\sigma}\phi_{i\sigma}(\mathbf{r}) \tag{2.41}$$

$$n_\sigma(\mathbf{r}) \equiv \sum_i |\phi_{i\sigma}(\mathbf{r})|^2 \tag{2.42}$$

used by

$$F[n_\alpha, n_\beta] \equiv T_s[n_\alpha, n_\beta] + \frac{1}{2}\int\int \frac{n(\mathbf{r})n(\mathbf{r})}{|\mathbf{r}-\mathbf{r}'|} d\mathbf{r}d\mathbf{r}' E_{xc}[n_\alpha, n_\beta] \tag{2.43}$$

corresponding to Eq.(2.31) where $n = n_\alpha + n_\beta$. In the DFT including spin degree of freedom, the exchange-correlation energy is written as

$$E_{xc}^{LSDA}[n_\alpha, n_\beta] = \int d^3\mathbf{r} n \varepsilon_{xc}^{unif}(n_\alpha, n_\beta), \tag{2.44}$$

for the LDA and

$$E_{xc}^{GGA}[n_\alpha, n_\beta] = \int d^3\mathbf{r} f(n_\alpha, n_\beta, \nabla n_\alpha, \nabla n_\beta), \tag{2.45}$$

for GGA.

2.2 Bloch's theorem

Bloch's theorem was formulated by Bloch in 1928 to describe wave function of an electron in a periodic potential system. Bloch's theorem states that the energy eigenfunction for the periodic potential system can be written using a periodic function, $u_{n\mathbf{k}}(\mathbf{r})$, that has the same periodicity as the potential.

$$\Phi_{n\mathbf{k}}(\mathbf{r}) = e^{i\mathbf{k}\cdot\mathbf{r}} u_{n\mathbf{k}}(\mathbf{r}) = u_{n\mathbf{k}}(\mathbf{r}+\mathbf{R}) \tag{2.46}$$

where $\mathbf{k}$ is the wave vector and $\mathbf{R}$ is a lattice vector. The energy eigenvalues $\varepsilon_n(\mathbf{k})$ corresponding to $\mathbf{k}$ exhibit periodicity by a reciprocal lattice vector $\mathbf{G}$ which is defined as $\mathbf{G}\cdot\mathbf{R} = 2\pi m$ for all $\mathbf{R}$, where m is an integer.

$$\varepsilon(\mathbf{k}) = \varepsilon_n(\mathbf{k}+\mathbf{G}) \tag{2.47}$$

Note that all states corresponding to $\mathbf{k}$ and any $\mathbf{k}+\mathbf{G}$ are equal, which means that $\Phi_{n\mathbf{k}}(\mathbf{r})$ is periodic in the reciprocal space, $\Phi_{\mathbf{k}}(\mathbf{r}) = \Phi_{\mathbf{k}+\mathbf{G}}(\mathbf{r})$. The energies associated with the index n vary continuously with wave vector $\mathbf{k}$ and form an energy band identified by the band index n. The eigenvalues for given n are periodic in $\mathbf{k}$, thereby all distinct values of $\varepsilon_n(\mathbf{k})$ occur within the first Brillouin zone of the reciprocal lattice.

2.3 Plane-wave basis set

Bloch's theorem states that each electronic wave function in the periodic system can be written as the product of a cell-periodic part $u_{n\mathbf{k}}(\mathbf{r})$ and a wave-like part $e^{i\mathbf{k}\cdot\mathbf{r}}$. Therefore, the electronic wave functions can be expanded using a discrete plane-wave basis set.

The Kohn-Sham orbitals are expanded by using the plane-wave basis set as follows

$$\Psi_n(\mathbf{r}) = \frac{1}{\sqrt{\Omega}} \sum_{\mathbf{G}} C_{n,\mathbf{G}} e^{i\mathbf{G}\cdot\mathbf{r}} \tag{2.48}$$

where Ω is the volume of the unit cell. The cell-periodic part of the wave function $u_{n\mathbf{k}}(\mathbf{r})$ can be expanded using the basis set of a discrete set of plane waves. Therefore, each electronic wave function can be written as a sum of discrete plane waves.

$$\Psi_{n,\mathbf{k}}(\mathbf{r}) = \frac{1}{\sqrt{\Omega}} \sum_{\mathbf{G}} C_{n,\mathbf{k}}(\mathbf{G}) e^{i(\mathbf{k}+\mathbf{G})\cdot\mathbf{r}} \tag{2.49}$$

Plane-wave basis set provides several benefits for DFT calculations. First, plane waves are independent to the positions of the nuclei because they are origin less functions. Therefore, Pulay forces exactly vanish and drastically facilitate force calculations. Second, derivatives in real-space are simply multiplications in G-space, and real and reciprocal spaces can be efficiently connected via Fast Fourier Transforms. Therefore, one can easily evaluate operators in that space in which they are diagonal. Since plane waves are extended throughout the space, increasing the largest $|\mathbf{G}|$ vector in Eq.(2.49), which is called the energy cutoff, E_{cut}, is the only way in order to improve the quality of calculations.

2.4 Pseudopotential

Physical and chemical properties of atoms, molecules, and solids strongly depends on rearrangements of valence electrons. The core electrons are strongly bound to the nuclei and barely play a role in the chemical bond of materials. On the other hand, DFT calculations with all-electron system by using plane-wave basis set require a tremendous number of plane waves to express the tightly bound core orbitals and to follow the rapid oscillations of the wave functions of the valence electrons in the core region, which needs a vast amount of computational cost. In order to overcome the problem, the pseudopotential method has been proposed [24]. The pseudopotential method decreased the number of plane waves by replacing core electrons and the deep ionic potential with a shallow pseudopotential. In this section, we describe the pseudopotentials used in this thesis.

We introduce the exact solutions of the Schrödinger equation for the core electrons by $|\Psi_c>$, and those for the valence electrons by $|\Psi_v>$.

$$\mathcal{H}|\Psi_n> = E_n|\Psi_n> \tag{2.50}$$

with $n = c$ or v. The valence orbitals can be written as the sum of a smooth function $|\Psi_v>$ which is called the pseudo wave function, and an oscillating function that is obtained from the orthogonalization of the valence to the core orbitals.

$$|\Psi_v> = |\phi_v> + \sum_c \alpha_{cv}|\Psi_c> \tag{2.51}$$

where

$$\alpha_{cv} = -<\Psi_c|\phi_v> . \tag{2.52}$$

The pseudo wave functions $|\phi_v>$ satisfy a Schrödinger-like equation with a pseudopotential V^{PP}

$$\mathcal{H}|\phi_v> = E_v|\phi_v> + \sum_c (E_c - E_v)|\Psi_c><\Psi_c|\phi_v> \tag{2.53}$$

and then

$$(T + V^{PP})|\phi_v >= E_v|\phi_v > \tag{2.54}$$

where V^{PP} is defined as

$$V^{PP} = V - \sum_c (E_c - E_v)|\Psi_c >< \Psi_c| \tag{2.55}$$

where V is the true potential.

It is almost completely canceled between the large negative potential energy by a valence electron when it is inside the core of an atom, and its large positive kinetic energy which is inherent in the oscillations of its wave function $|\Psi_c >$. Therefore, the second term in Eq.(2.55) represents a nonlocal repulsive potential, making the pseudopotential much shallower than the true potential in the core. As a result, the pseudo wave functions $|\psi_V >$ are smooth and not oscillate in the core region.

2.4.1 Norm-conserving pseudopotentials

Norm-conserving pseudopotentials are constructed by forcing the pseudo wave functions to coincide with the true valence wave functions beyond a certain distance while they have the same norm with the true valence wave functions [25]. DFT calculations are generally employed to generate pseudopotentials for a free atom by comparing with a given reference electron configuration. To construct norm-conserving pseudopotentials, the following four general conditions should be satisfied.

First, the normalized atomic radial pseudo wave function $R_l^{\mathrm{PD}}$with angular momentum l is equal to the normalized radial all-electron wave function R_{nl}^{AD} with a principle quantum numbers n and l beyond a cuttoff radius r_c.

$$R_l^{\mathrm{PD}}(r) \;\; = \;\; R_{nl}^{AE}(r) \;\; (r \geq r_c). \tag{2.56}$$

Second, the norm enclosed within r_c for the two wave functions should be equal.

$$\int_0^{r_c} dr|R_l^{PD}(r)|^2 r^2 \;\; = \;\; \int_0^{r_c} |R_{nl}^{AE}(r)|^2 r^2 \tag{2.57}$$

Third, the valence all-electron and pseudopotential eigenvalues should be equal each other.

$$\epsilon_l^{PD} \;\; = \;\; \epsilon_{nl}^{AE} \tag{2.58}$$

Fourth, there should not be any nodes in the valence pseudo wave functions generated from the pseudopotential.

2.4.2 Ultrasoft pseudopotential

In the norm-conserving pseudopotential, the all-electron wave function is replaced by a soft nodeless pseudo wave function, which has the same norm as the all-electron wave function within the chosen core radius. For elements with strongly localized

orbitals, the pseudopotentials require a large plane-wave basis set. On the other hand, an ultrasoft pseudopotential, proposed by Vanderbil, provides the pseudo wave function allowed it be as soft as possible within the core region, leading to the signficant reduction of the cutoff energy required [26]. We briefly introduce a procedure to construct the ultrasoft pseudopotential.

All-electron calculations are carried out for a free atom by comparing with the reference configuration to calculate a screened potential $v^{AE}(r)$ and the all-electron wave function $|\Psi_i^{AE}>$.

$$(-\frac{1}{2}\nabla^2 + v^{AE} - \epsilon_i)|\Psi_i^{AE}> \;\; = \;\; 0 \tag{2.59}$$

where i indicates quantum numbers, $i = n,\ l,\ m$. Then, a pseudo wave function $|\psi_i^{PD}>$ and a local potential $v^{AE}(r)$ are constructed, where the pseudo wave function $|\Psi_i^{PD}>$should be smoothly connected at r_c.

$$\Psi_i^{PD}(r) \;\; = \;\; \Psi_i^{AE}(r)\ (r \geq r_c) \tag{2.60}$$

Here, norm-conseravatuin constraint is not imposed. Similarly, a smooth local potential, $v_{loc}^{PD}(r)$, is generated with the constraint that v_{loc}^{PD} matches smoothly to $v^{AE}(r)$ at a cutoff radius r_c

$$v_{loc}^{PD}(r) = v^{AE}(r)\ (r \geq r_c) \tag{2.61}$$

Next, orbitals $|\chi_i>$ are calculated to describe the ultrasoft pseudopotential using the pseudo wave function and the local potential.

$$|\chi_i> \;\; = \;\; (\epsilon_i + \frac{1}{2}\nabla^2 - v_{loc}^{PD})|\Psi_i^{PD}> . \tag{2.62}$$

By defining the matrix of inner products, $B_{ij} =< \Psi_i^{PD}|\chi_i >$, we can make a set of orbitals, β_i, which is dual to $|\Psi_i^{PD}>$,$< \beta_i|\Psi_j^{PD} >= \delta_{ij}$

$$|\beta_i> \;\; = \;\; \sum_j (B^{-1})_{ji}|\chi_j> . \tag{2.63}$$

We note that they form the projectors of the nonlocal operators. We further calculate the deficit charge density $Q_{ij}(r)$ defined as follows.

$$Q_{ij}(r) \;\; = \;\; \Psi_i^{*AE}(\mathbf{r})\Psi_j^{AE}(\mathbf{r}) - \Psi_i^{*PD}(\mathbf{r})\Psi_j^{PD}(\mathbf{r}) \tag{2.64}$$

$$Q_{ij} \;\; = \;\; \int d\mathbf{r} Q_{ij}(\mathbf{r}) \tag{2.65}$$

$Q_{ij}(\mathbf{r})$ corresponds to the deficient electron within the cutoff radius r_c. Although $Q_{ij}(\mathbf{r})$ is zero for the case that the norm is conserved, we now consider to the deficit charge density is not zero. Here, we construct another matrix, D_{ij}, defined as follows.

$$D_{ij} \;\; = \;\; B_{ij} + \epsilon_j Q_{ij}. \tag{2.66}$$

Then, $|\Psi_k^{PD}>$ obeys the secular equation.

$$(-\frac{1}{2}\nabla^2 + v_{loc}^{PD} + \sum_{ij} D_{ij}|\beta_i><\beta_j|)|\Psi_k^{PD}> \tag{2.67}$$

$$= \epsilon_k(1 + \sum_{ij} Q_{ij}|\beta_i><\beta_j|)|\Psi_k^{PD}> \tag{2.68}$$

where k is a composite index as in the index i and j. Then, we finally construct the ultrasoft pseudopotential as follows.

$$\hat{v}_{ion}^{PD} = v_{ion,loc}^{PD}(r) + \sum_{ij} |\beta_i > D_{ij}^{(0)} < \beta_j| \tag{2.69}$$

where $v_{ion,loc}^{PD}(r)$ and $D_{ij}^{(0)}$ are obtained from following equations,

$$v_{ion,loc}^{PD}(r) = v_{loc}^{PD}(r) - v_H^{PD}(r) - v_{xc}^{PD}(r) \tag{2.70}$$

$$D_{ij}^{(0)} = D_{ij} - \int d\mathbf{r} v_{loc}^{PD}(\mathbf{r}) Q_{ij}(\mathbf{r}) \tag{2.71}$$

where $v_H^{PD}(r)$ and $v_{xc}^{PD}(r)$ are the Hartree and exchange-correlation potentials, respectively, calculated from the valence pseudo wave functions. The ultrasoft pseudopotential significantly improves the norm-conserving pseudopotential by relaxing the norm-conservation condition that is usually imposed on the pseudopotential approach. Especially, this method allows first-row and transition-metal elements to be treated efficiently. Ultrasoft pseudopotentails are now adopted quite widely because of significant reduction of the computational cost.

2.5 Effective screening medium method

To inject carriers in surface/interface of materials, we use the effective screening medium (ESM) method developed by Otani and Sugino in 2006 [27]. Their approach consists of solving the generalized Poisson equation under various boundary conditions normal to the surfaces. This task is accomplished with the help of Green's function technique. The Kohn-Sham equation is solved in a cell with a finite length in the z direction imposing the periodic boundary condition. This treatment is allowed when the electrons are not extended much beyond the surface region, but are instead confined within a certain region near the surface of slabs.

By using a slab geometry, which is periodic in the direction parallel to the surface but is not periodic in the perpendicular direction, sandwiched by semi-infinite media, such as vacuum, an electrode, or an electrolyte, we can describe the surfaces and interfaces. We treat the slab part which consists of substrate and adsorbate atoms within DFT. While we treat the medium part using a continuum characterized by relative permittivity $\epsilon(\mathbf{r})$ and additional classical charge density $n_c(\mathbf{r})$. We assume that the electrons are confined to the region, say $z \in [-z_0, z_0]$, and that the wave functions are solved using the repeated slab of length $2z_0$, for which standard DFT with plan wave basis set programs are applicable.

The total-energy functional of the ESM model is

$$\begin{aligned} E[n_e, V] =& K[n_e] + E_{xc}[n_e] - \int d\mathbf{r} \frac{\epsilon(\mathbf{r})}{8\pi} |\nabla V(\mathbf{r})|^2 \\ &+ \int d\mathbf{r} [n_e(\mathbf{r}) + n_I(\mathbf{r})] V(\mathbf{r}) \end{aligned} \tag{2.72}$$

where $n_e(\mathbf{r})$ denotes the electron charge density, $n_I(\mathbf{r})$ is the nuclear charge density, and $V(\mathbf{r})$ is the electrostatic potential. In addition, K and E_{xc}, respectively, represent the kinetic and exchange-correlation energy functional of the electrons; $\epsilon(\mathbf{r})$ is the (nonuniform) relative permittivity of the ESM. In this equation, the classical charge density is omitted for simplicity. We also omit the entropic term of the electrons. By tacking the variation of the energy, the Kohn-Sham equation is obtained when the total-energy functional is varied by the Kohn-Sham orbital under the orthonormality constraint. When varied by the electrostatic potential, we obtain a Poisson equation in that the relative permittivity has a spatial dependence. Using a Green′s function for the Poisson equation

$$\nabla \cdot [\epsilon(\mathbf{r}) \nabla] G(\mathbf{r}, \mathbf{r}') = -4\pi \delta(\mathbf{r} - \mathbf{r}'). \tag{2.73}$$

Eq.(2.72) could be rewritten

$$\begin{aligned} E[n_e] =& K[n_e] + E_{xc}[n_e] + \frac{1}{2} \int \int d\mathbf{r} d\mathbf{r}' n_e(\mathbf{r}) G(\mathbf{r}, \mathbf{r}') n_e(\mathbf{r}') \\ &+ \int \int d\mathbf{r} \mathbf{r}' n_e(\mathbf{r}) G(\mathbf{r}, \mathbf{r}') n_I(\mathbf{r}') \\ &+ \frac{1}{2} \int \int d\mathbf{r} d\mathbf{r}' n_I(\mathbf{r}) G(\mathbf{r}, \mathbf{r}') n_I(\mathbf{r}') \end{aligned} \tag{2.74}$$

which has the well-known form for the DFT energy functional, expect that the electrostatic interaction is modified slightly from $1/r$ to that according to Eq.(2.73). The third, fourth, and fifth terms, respectively, correspond to Hartree energy (E_H), electron-ion interaction energy (E_{e-i}), and ion-ion interaction energy (E_{ion}). The term for interaction between the electrons and the nuclei

$$\int \int d\mathbf{r} \mathbf{r}' n_e(\mathbf{r}) G(\mathbf{r}, \mathbf{r}') n_I(\mathbf{r}'), \tag{2.75}$$

can be rewritten for the pseudopotential scheme as

$$\begin{aligned} &\int \int d\mathbf{r} d\mathbf{r}' n_e(\mathbf{r}) G(\mathbf{r}, \mathbf{r}') n_g(\mathbf{r}') + \int d\mathbf{r} n_e(\mathbf{r}) V_{loc}^{short}(\mathbf{r}) \\ &+ \sum_{\alpha} < \phi_{alpha} | \Delta V_{ps} | \phi_{\alpha} > \end{aligned} \tag{2.76}$$

in which the first, second, and third term correspond, respectively, to the long-range local, short-range local, and nonlocal part. In the first term, $n_g(\mathbf{r})$ is the effective nucleus charge localized near the nuclear position; $V_{loc}^{short}(\mathbf{r})$ is the short-range local potential; $\phi_{\alpha} s$ are the Kohn-Sham orbitals; and ΔV_{ps} is the nonlocal part of the

psudopotential, which has a finite range from the nuclear position. We call the sum of the first and second terms the local potential energy (E_{loc}) hereafter.

This paragraph shows a Green's function formulation for the solution of the Poisson equation, which is accomplished by imposing appropriate boundary conditions on Eq.(2.73) and expressing the solution as

$$V(\mathbf{r}) = \int d\mathbf{r}' G(\mathbf{r}, \mathbf{r}') n_{tot}(\mathbf{r}'). \tag{2.77}$$

For this purpose we consider the case in which relative permittivity depends only on z. Then the Poisson equation

$$\partial_z[\epsilon(z)\partial_z] - \epsilon(z)\nabla_{\parallel}^2 G(\mathbf{r}_{\parallel} - \mathbf{r}'_{\parallel}, z, z') = -4\pi\delta(z - z'), \tag{2.78}$$

becomes the following in the Laue representation:

$$\partial_z[\epsilon(z)\partial_z] - \epsilon(z) g_{\parallel}^2 G(\mathbf{g}_{\parallel}, z, z') = -4\pi\delta(z - z'), \tag{2.79}$$

where $\mathbf{g}_{\parallel}$ is a wave vector parallel to the surface and $g_{\parallel}$ indicates the absolute value of $\mathbf{g}_{\parallel}$. In this thesis, to inject hole/electron by the counter electrode, we use the ESM with the boundary conditions given following.

$$\begin{cases} V(\mathbf{g}_{\parallel}, z)|_{z=z_1} = 0 \\ \partial_z V(\mathbf{g}_{\parallel}, z)|_{z=-\infty} = 0 \end{cases}, \epsilon(z) = \begin{cases} 1 \ if \ |z| \leq z_1 \\ \infty \ if \ |z| \geq z_1 \end{cases} \tag{2.80}$$

In this boundary conditions, the metal electrode is put on only one side of the slab, as $z > z_1$. When the cell is consists of atomic layer materials, the system correspond to the top/back gate field effect transistor in which the metallic continuum that is separately located at $z > z_1$ plays the role of a counter gate electrode.

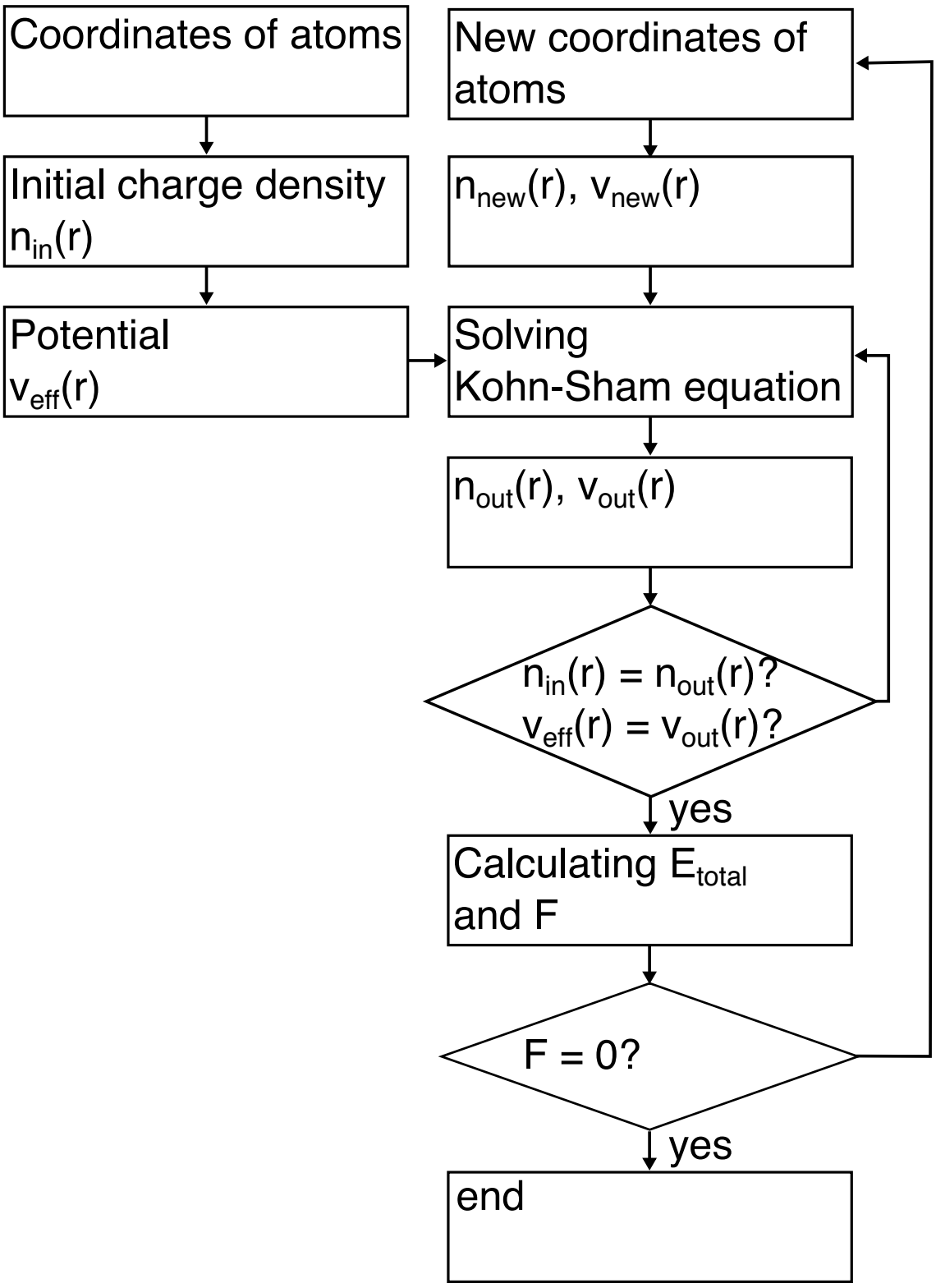

Figure 2.1: A flow-chart for solving the Kohn-Sham equation.

Chapter 3

Two-Dimensional sp^2 Carbon Network of Fused Pentagons: All Carbon Ferromagnetic Sheet

In this chapter, we investigate geometric and electronic structures of a two-dimensional stable carbon allotrope consisting of pentagonal rings.

3.1 Introduction

Pentagons embedded into hexagonal sp^2 (threefold-coordinated) carbon networks play a crucial role in determining the geometric and electronic properties of the resulting nanoscale carbon allotropes. By assembling the twelve pentagons with an appropriate number of hexagons, zero-dimensional hollow-cage carbon clusters of nanometer size can be obtained [2, 28]. Fullerenes possess a relatively deep lowest unoccupied state [29] compared with other carbon molecules comprised only of hexagons with a closed-shell electronic structure. Furthermore, they possess a common electronic feature that is characterized by the spherical harmonics Y_{lm} due to their nearly spherical π electron systems [30]. On the other hand, it is known that the detailed electronic structures of fullerene molecules are completely different from each other depending on the symmetry and local atomic arrangement on the nanoscale sphere, even though the molecules have the same size [31, 32].

In the planar hexagonal carbon network, pentagons should appear with the appropriate number of polygons. For example, an isolated pentagon embedded in graphene induces the formation of a heptagon adjacent to it to maintain a planar sp^2 network, as is found in Stone-Wales-type [33, 34] and fused-pentagon-type [15] topological defects. Since pentagons and other polygons disrupt the AB bipartite symmetry of graphene, such topological defects in graphene occasionally induce an unusual electronic structure at or near E_F in addition to the characteristic electronic structure of graphene. Localized states and flat dispersion bands associated with the topological defects are expected to emerge around them [18, 35]. The linearly aligned fused pentagons and octagons effectively terminate the π electron system near E_F, and leads to the flat dispersion band at the edges of the topological line

defects [15]. Furthermore, in the case of the topological line defects with the fused pentagons and octagons embedded in CNTs, the nanotubes exhibit ferromagnetic spin ordering along the topological line defects [36].

In general, the defect density strongly affects the physical properties of the host material. Therefore, it is interesting to explore the geometric structure and electronic properties of graphene containing many topological defects. In this chapter, we explore the geometric and electronic structures of a 2D sp^2 carbon allotrope consisting of pentagons and dodecagons, as a representative structure of the limit of topological defects in sp^2 hexagonal networks.

All calculations were performed within the framework of DFT [19, 20] using the Simulation Tool for Atom TEchnology (STATE) package [37]. For calculation of the exchange-correlation energy between electrons, we used the local spin density approximation (LSDA) with a functional form fitted to Monte-Carlo results for a homogeneous electron gas [21, 22]. A Vanderbilt ultrasoft pseudopotential was used to describe the electron-ion interaction [26]. The valence wave functions and charge density were expanded in terms of the plane-wave basis sets with cutoff energies of 25 and 225 Ry, respectively. The structural optimizations were performed until the forces on each atom were less than 5 mRy/Å for each lattice constant. Integrations in the first Brillouin zone were carried out using $6\times6\times1$ $\boldsymbol{k}$-points for the isolated sheet consisting of pentagons and dodecagons of C atoms. To investigate the interlayer interaction and the stacking geometries of the sheets, we performed $6\times6\times6$ $\boldsymbol{k}$-point sampling in the Brillouin zone.

Here, we consider a 2D sp^2 carbon sheet consisting of fused pentagon trimers (acepentalene structure [38]) of which three edges are shared by its three adjacent trimers. Accordingly, in the topological view, the network can be regarded as the honeycomb network of fused acepentalenes, which consists of fused pentagonal rings and large dodecagonal pores. With this choice of initial geometry, the resulting material has a honeycomb lattice containing 14 C atoms per unit cell, which forms a 2D covalent network of threefold-coordinated C atoms.

3.2 Energetics and optimized structure

Figure 3.1 shows the total energy per atom as a function of lattice parameter a of the fused pentagon network of threefold-coordinated C atoms. We found that the optimum lattice constant of the 2D fused pentagon network is $a = 7.1$ Å. The calculated total energy is 0.61 eV/atom with respect to the energy of graphene, which is slightly higher than that of the other carbon allotropes containing pentagons and other polygons [39, 40, 41].

At the optimized lattice parameter a, the fused pentagon network retains its planar structure [Figure 3.2], even though an isolated acepentalene molecule has a bowl-shaped conformation. The optimized bond lengths for the acepentalene unit are $d_1 = 1.40$ Å, $d_2 = 1.42$ Å, and $d_3 = 1.54$ Å. The bond lengths are different from those of the isolated acepentalene molecule because of the planar structure of the fused pentagon network. The lengths of the three bonds associated with the vertex of three pentagons (d_1) are close to that of the double bond of fullerene, indicating

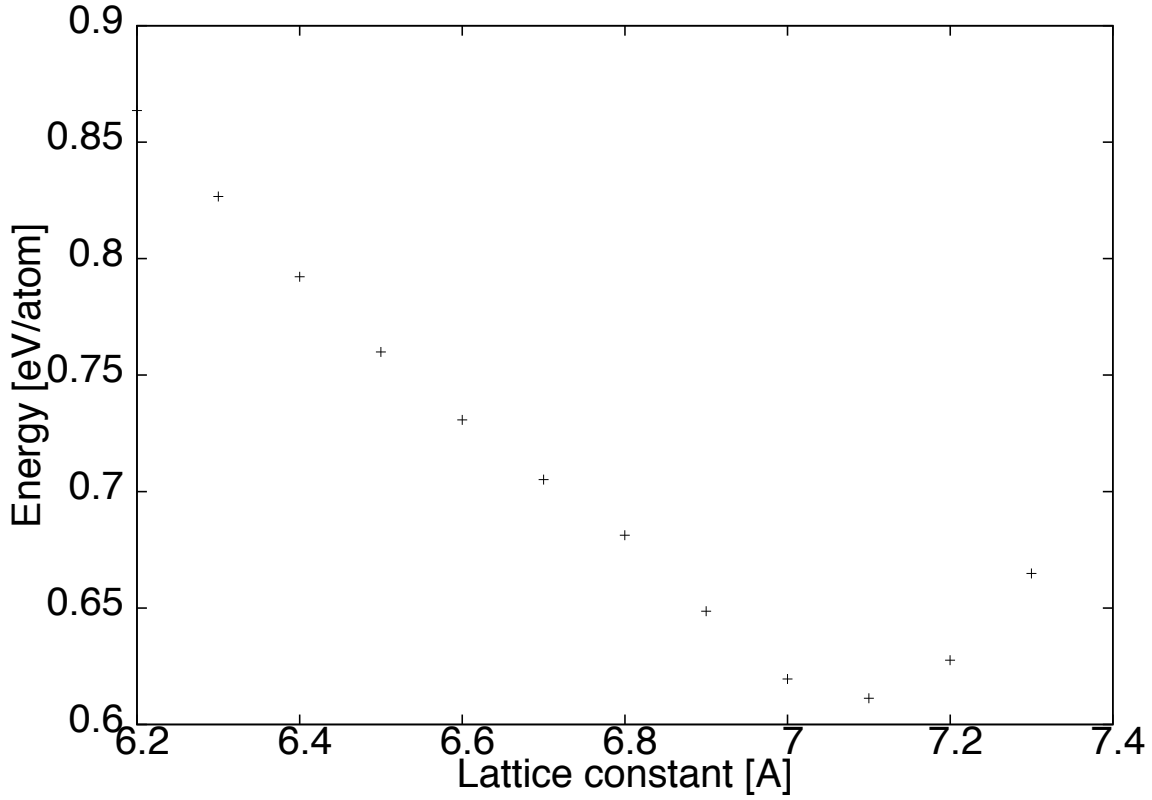

Figure 3.1: Total energy per atom of the fused pentagon network as a function of the lattice parameter a. The energies are measured with respect to the energy of isolated graphene.

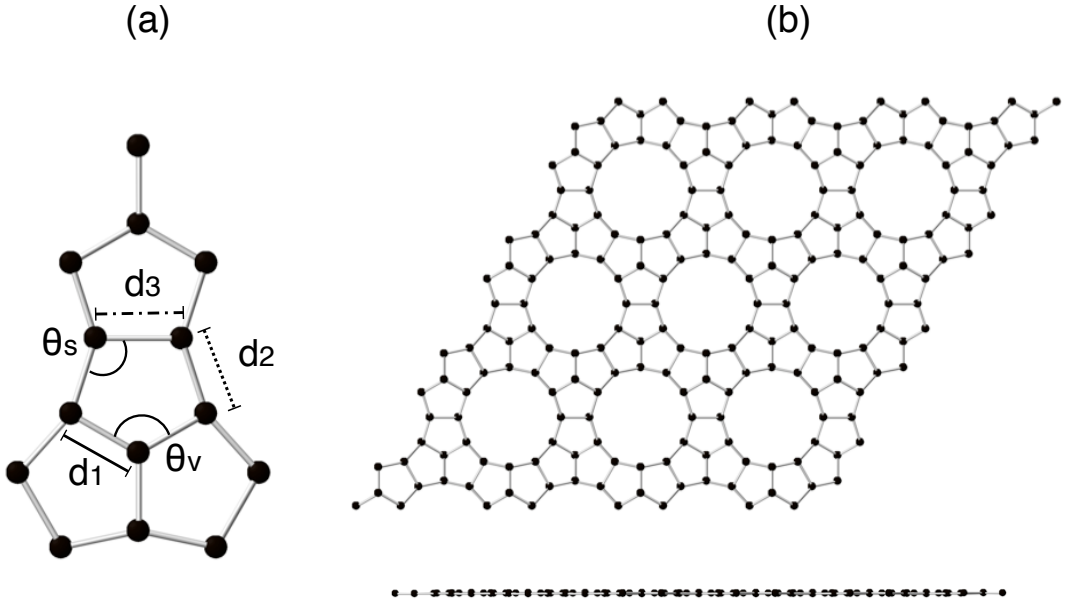

Figure 3.2: (a) Optimized structure of fused pentagon network in the unit cell. (b) Top and side views of the optimized geometry of the fused pentagon network of sp^2 C atoms with a lattice constant of 7.1 Å.

the fact that those bonds possess the double bond nature of sp^2 C atoms. Indeed, the angles of these bonds are exactly $\theta_v = 120°$. In contrast, the bond shared with two acepentalene units (d_3) is longer than that of the usual sp^2 bond and closer to that of the sp^3 bond of diamond. The bond angle associated with the bond is $\theta_s = 108°$, which is close to that of sp^3 network materials. Furthermore, the bonds at the edges of the dodecagon (d_2) also have the sp^2 covalent bond nature. The calculated atomic density of the sheet is 0.320 /Å^2, which is slightly less than the atomic density of graphene because of the large dodecagon pores. Therefore, the fused pentagon sheet is light sp^2 carbon allotropes with a planar structure.

The kinetic stability of the fused pentagon network is worth investigating. We investigated the geometric structure of the fused pentagon network at temperatures of 200, 400, 600, 800, and 1000 K by performing *ab initio* molecular dynamics simulations for a few picosecond simulation times. The simulations showed that the fused pentagon sheet retains its 2D planar covalent network structure at temperatures up to 1000 K. Therefore, once the sheet is synthesized by an appropriate experimental method, it is expected to retain its characteristic structure under ambient conditions.

3.3 Electronic strucutre

Figure 3.3 shows the electronic structure of the fused pentagon network with an equilibrium lattice constant of $a = 7.1$ Å. We found that the fused pentagon trimer sheet is a metal with a flat dispersion band that crosses E_F. The flat dispersion band has a dispersion of about 0.1 eV around the zone center Γ point. Thus, it is expected that the flat-band state induces spin polarization on the sheet according to E_F instability associated with the flat dispersion band. The flat dispersion band splits into lower and upper branches for the majority and minority spin states, respectively, indicating that the sheet exhibits magnetic ordering. The calculated exchange splitting between the branches of the flat dispersion band is about 0.10 eV, and the induced magnetic moment is 0.62 μ_B/nm^2.

Figure 3.4 shows the isosurfaces of the polarized electron spins of the fused pentagon network. We found that the polarized electron spins are ferromagnetically aligned and extend throughout the sheet. Therefore, the fused pentagon network is a 2D ferromagnet consisting of only sp^2 C atoms whose covalent bonds are fully saturated. Furthermore, the extended nature of the spin distribution indicates that the flat dispersion band is not induced by the localized state at certain atomic sites, but is induced by extended π electron states throughout the sheet. The wave function associated with the flat-band state at the Γ point exhibits the extended π electron nature [Figure 3.5(a)], indicating that the delicate balance among the extended π state of C atoms induces the flat dispersion band of the sheet. Furthermore, it should be noted that the spin distribution is similar to the wave function distribution of the electronic state labelled δ at K point [Figure 3.5 (c)]. Similar flat dispersion bands have also been observed in hexagonal network materials with zigzag edges or interfaces [11, 12, 17, 42]. Therefore, the fused pentagon network extends the research field associated with C allotropes with the flat dispersion band.

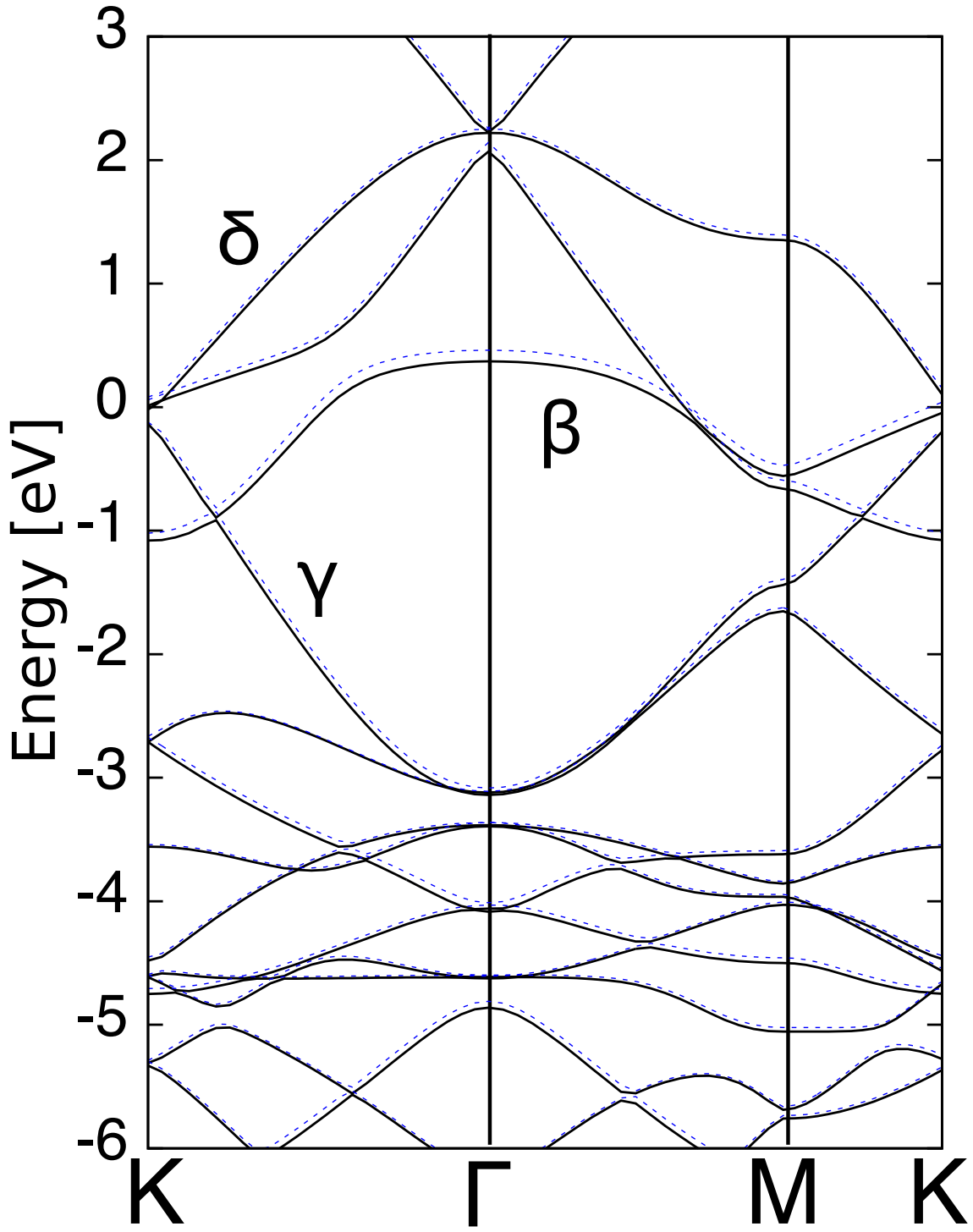

Figure 3.3: Electronic energy band of the fused pentagon network near the Fermi level. The solid and dashed lines indicate the majority and minority spin states, respectively. The energies are measured with respect to the Fermi level.

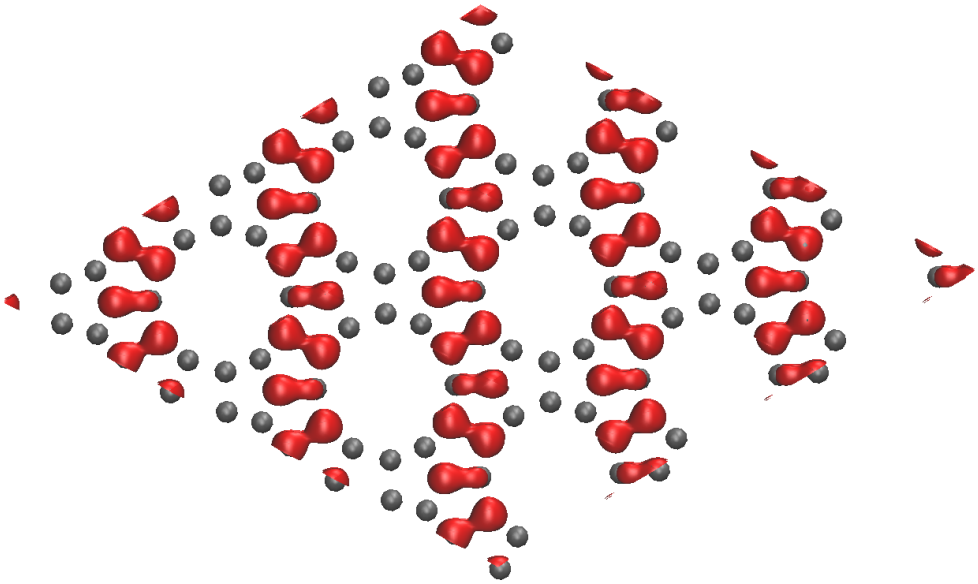

Figure 3.4: Isosurfaces of the spin density, $\Delta n(\boldsymbol{r}) = n_\alpha(\boldsymbol{r}) - n_\beta(\boldsymbol{r})$, of the fused pentagon sheet. The isosurfaces correspond to 0.001 e/au. Gray spheres indicate the atomic positions of the fused pentagon network.

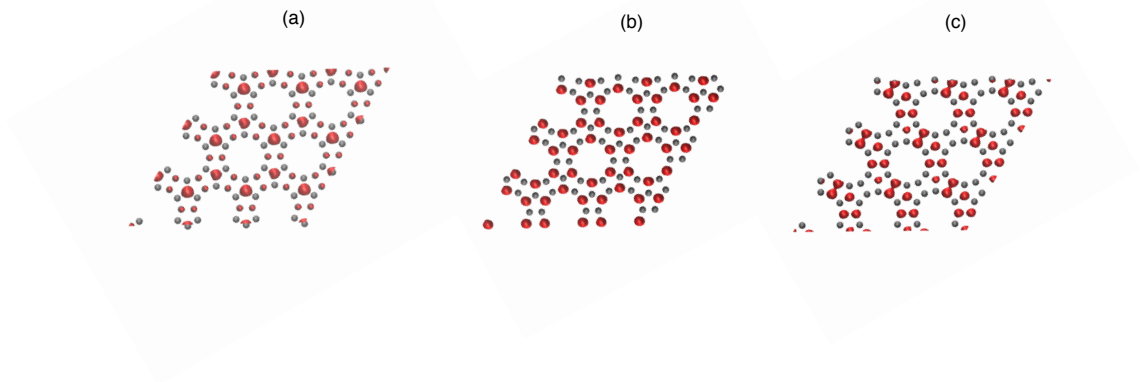

Figure 3.5: Isosurfaces of the squared wave function of (a) the flat dispersion band indicated by β at the Γ point in Fig. 3.3, (b) the dispersive band just above E_F indicated by γ at the K point in Fig. 3.3, and (c) the other dispersive band with higher energy indicated by δ at K point in Fig. 3.3. The isosurfaces correspond to 0.8 e/au. Gray spheres indicate the atomic position of the fused pentagon network.

Since the polarized spin has striped distribution along the zigzag direction of the honeycomb network of fused pentagons, the antiparallel spin distribution is expected to occur on this system. To corroborate the issues, we calculate the electronic structure of the sheet with double periodicity normal to the spin strips, which contains two strips of spin density in its unit cell. Under this extended unit cell, we compare the total energy of the ferromagnetic state with that of the antiparallel spin strip state. Our calculation shows that the antiparallel spin configuration between adjacent strips emerges as a metastable state in addition to the ferromagnetic state. Calculated total energy of the antiparallel state is higher than that of the ferromagnetic state by 2.6 meV/atom. Therefore, the ferromagnetic spin state is the ground state of the honeycomb network of the fused pentagons.

The fused pentagon network also exhibits another interesting feature in the electronic energy band near E_F, in addition to the flat dispersion band. Three states are bunching up together with a small gap of about 0.1 eV at the K point just above the flat dispersion band. Two of the three states possess almost linear dispersion with respect to the wave number, similar to the π and π^* states of graphene and graphite. Therefore, the massive Dirac electrons are expected to be located on the fused pentagon network, which does not contain any graphene-like hexagonal covalent network structure. The wave functions of these states exhibit a non-bonding nature as in the case of the π state of the graphene and graphite at the Dirac point. The lowest branch of the state is distributed on the atoms adjacent to the vertex of three pentagons [Figure 3.5(b)]. The upper branch is distributed on the atoms at the vertex of three pentagons and the atoms shared by the two acepentalene structures [Figure 3.5(c)]. This suggests that a graphene-like electronic structure is expected to occur in the honeycomb network material with internal geometric structures. However, further analytic investigation is required.

3.4 Stacking structure

The planar materials usually form a stacking structure similar to the case of graphite and transition-metal chalcogenides. Furthermore, because of the bowl shape of the isolated acepentalene molecule, the fused pentagon network sheet is expected to form covalent bonds with adjacent sheets, leading to the three-dimensional network structure. Therefore, we investigated the relative stability and geometric structures of the fused pentagon sp^2 carbon sheets having stacking structures. By changing the interlayer spacing, we found that the layered system comprising the fused pentagon sheets has an energy minimum at the interlayer spacing of 3.2 Å. The calculated energy gain that arises from the interlayer interaction is 20 meV/atom. At the equilibrium interlayer spacing, each fused pentagon sheet still retains its planar structure and does not form covalent bonds with adjacent layers.

3.5 Conclusion

We have investigated the geometric and electronic structures of a 2D sp^2 carbon allotrope consisting of pentagons and dodecagons by first-principles total energy calculations based on density functional theory. We found that the 2D sp^2 carbon allotrope retains its planar structure at the equilibrium lateral lattice parameter $a = 7.1$ Å. At the equilibrium lattice constant, the calculated total energy of the sheet is 0.66 eV/atom with respect to the energy of graphene, indicating that the structure is energetically stable. Further *ab initio* molecular dynamics simulations confirmed that the sheet was kinetically stable up to a temperature of 1000 K for simulation times of a few picoseconds. We found that the sheet is a metal with a flat dispersion band that crosses E_F. Owing to the flat dispersion band at E_F, the state is split into majority and minority spin states, leading to spin polarization on the sheet. The polarized electron spin is ferromagnetically ordered and distributed throughout the whole network of the sheet with a magnetic moment of 0.62 μ_B/nm^2. In addition to the magnetism arising from the flat dispersion band, although the network does not contain any hexagonal rings, the fused pentagon sp^2 carbon sheet has a pair of massive Dirac dispersion bands at the K point as in the case of graphene and graphite. Detailed analysis on the wave function indicated that the states possess a non-bonding π electron nature on the honeycomb network of fused pentagons.

Chapter 4

Coexistence of Dirac cones and Kagome flat bands in a porous graphene

In this chapter, we investigate the geometric and electronic structures of porous graphene networks consisting of phenalenyl and phenyl groups, which are connected alternately with C_3 symmetry via single bonds to form a honeycomb network.

4.1 Introduction

Polymerization and oligomerization of hydrocarbon molecules can provide structurally well-defined π electron networks with various dimensionalities. These low-dimensional or porous graphene networks have attracted much attention because of their high surface areas and electronic structure modulation, which are promising for application in energy and electronic devices in the near future [43, 44, 45, 46]. The electronic structures of such polymers and oligomers strongly depend on the combination of hydrocarbon molecules and polymer chains, which allows us to tailor their physical and chemical properties by fabrication under optimum external conditions [47, 48, 49, 50]. This indicates that porous magnetic C nanomaterials may be synthesized by polymerizing hydrocarbon molecules with radical spins. Phenalenyl is one possible candidate as a constituent unit of such magnetic materials [51, 52, 53, 54, 55]. Dimerization of triphenylphenalenyl and cyclodehydrogenated phenalenyl leads to complexes containing two phenalenyls possessing singlet and triplet spin coupling as their stable states [56, 57, 58, 59]. Despite intensive experimental and theoretical works on two phenalenyls connected via a covalent π network, the possible electronic structures of 2D networks consisting of phenalenyl molecules have not yet been investigated in detail. The three-fold symmetry of the phenalenyl network causes honeycomb networks of radical spins or non-bonding state to be distributed on phenalenyls with appropriate interconnect units, leading to interesting electron systems.

All calculations were performed within the framework of DFT [19, 20] using the STATE code [37]. To calculate the exchange-correlation energy among interacting

electrons, we used the GGA with the Perdew-Burke-Ernzerhof functional [23]. To investigate the spin-polarized states of the porous hydrocarbon sheets, the spin degree of freedom was taken into account for all calculations. Vanderbilt ultrasoft pseudopotentials were used to describe the electron-ion interaction [26]. The valence wave functions and charge density were expanded in terms of the plane waves with cutoff energies of 25 and 225 Ry, respectively, which sufficiently describe the electronic structure and energetics of hydrocarbon molecules and graphene-related materials [60]. To simulate an isolated porous hydrocarbon sheet, the sheet was separated by a vacuum spacing of 10.58 Å. Atomic structures of the sheets were optimized until the force acting on each atom was less than 1.33×10^{-3} HR/au. Integration over the Brillouin zone was carried out using an equidistance mesh of $2\times2\times1$ $\boldsymbol{k}$ points. To inject holes into the sheet, we used the ESM method to solve the Poisson equation under the field-effect-transistor structure with a counter gate electrode situated above the sheet with vacuum regions of 5.29 Å [27].

4.2 Energetics and optimized structures

Figure 4.1 shows the optimized structures of 2D porous hydrocarbon networks consisting of phenalenyl connected via phenyl with various arrangements under the hexagonal cell parameter of 19.4 Å. For all phenyl arrangements, the phenalenyl units retained a planar structure as their stable conformation. As illustrated in Fig. 4.1(a), two phenalenyl units per unit cell form a hexagonal lattice in which phenyl units connect adjacent phenalenyl units through covalent bonds like those of graphene. Simultaneously, three phenyl units form a Kagome lattice in which phenalenyl acts as an interunit bond. Because of the planar conformations of both phenyl and phenalenyl, the porous hydrocarbon sheet possesses a 2D π electron system. Rotation of phenyl modulates the π electron system: By rotating one of three phenyl units, the π electrons form a chain network in which the alternating phenalenyl and phenyl units form zigzag chains (chain structure in Fig. 4.1(b)). By rotating two phenyl units, π electrons are segmented into a phenalenyl dimer containing a phenyl unit (dimer structure in Fig. 4.1(c)). Finally, π electrons are localized on each phenalenyl and phenyl in the monomer structure depicted in Fig. 4.1(d).

The total energies of the porous hydrocarbon sheets with various phenyl conformations are listed in Table 4.1. Among the four structures, the planar structure is the least stable with a total energy higher by 0.8 eV per cell (16 meV/ C atom) than that of the ground state conformation. The total energy monotonically decreases by increasing the number of rotated phenyl units, although the π conjugation decreases. The decrease of the total energy with respect to the rotation of phenyl units is caused by the steric hindrance between hydrogen atoms attached to the phenyl and phenalenyl. Since the hydrogen atoms attached to the phenyl and phenalenyl are positively charged, the hydrogen atoms tend to separate each other to reduce the Coulomb's repulsive interaction. The thermal stability of the porous hydrocarbon sheets was investigated by *ab initio* molecular dynamics simulations conducted at a constant temperature up to 3000 K for simulation times of 1 ps. Under all temperatures, all structures retained their initial network topologies. On the other hand,

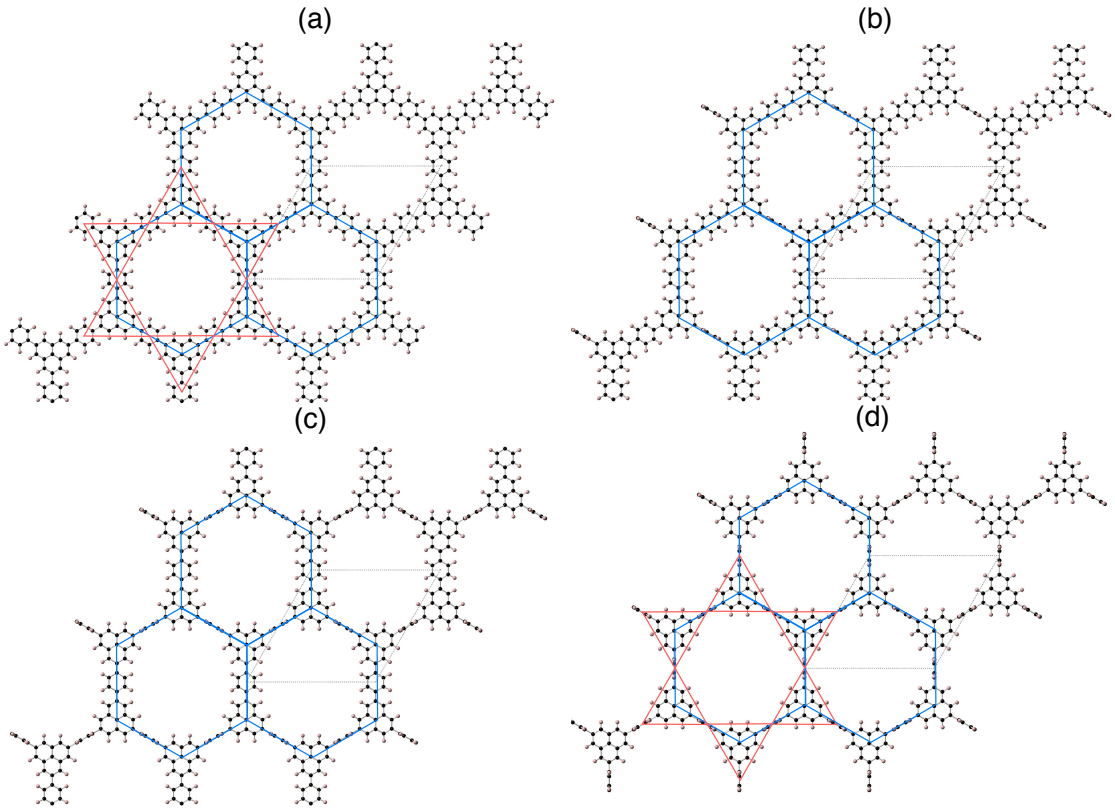

Figure 4.1: Optimized structures of porous hydrocarbon sheets consisting of phenalenyl and phenyl groups with (a) planar, (b) chain, (c) dimer, and (d) monomer conformation. Black and pink balls denote carbon and hydrogen atoms, respectively. Black dotted lines show the unit cell of each network. Blue hexagons and red triangles show hexagonal and Kagome networks of phenalenyl and phenyl units, respectively.

Table 4.1: Relative total energies of porous hydrocarbon sheets consisting of phenalenyl and phenyl groups with antiferromagnetic (AF), ferromagnetic (F), and non-magnetic (NM) states. The energies are measured from that with the planar conformation without spin polarization.

Structures	AF state [meV]	F state [meV]	NM [meV]
2D	803	817	1116
Chain	301	310	612
Dimer	159	163	471
Monomer	0	0	313

at the elevated temperatures, the phenyl units are tilted by angles of 20-40 degrees from the planar arrangement owing to the steric hindrance between hydrogen atoms attached to the phenalenyl and phenyl. Thus, we confirm that the 2D networks of phenalenyl and phenyl proposed here are both statically and dynamically stable and are expected to be stable under ambient conditions once they are synthesized experimentally.

4.3 Electronic structures

Figure 4.2 presents the electronic structures of 2D porous hydrocarbon sheets consisting of phenalenyl and phenyl. The planar structure possesses a characteristic feature around E_F [Figure 4.2(a)]. The porous hydrocarbon sheet is a zero-gap semiconductor with a pair of linear dispersion bands at E_F. In addition to the linear dispersion bands, we find three bunched states just above and below the linear dispersion bands. One of the three branches exhibits perfect flat band nature while the remaining two have finite band dispersion, consistent with their Kagome band structure. These observations indicate that Dirac cone and Kagome flat bands coexist in the porous hydrocarbon sheet of phenalenyl and phenyl with flat conformation. The Dirac cone is robust while the Kagome bands are fragile against the rotation of phenyl: A Dirac cone is observed for all porous hydrocarbon sheets, regardless of the phenyl conformation. In contrast, the Kagome flat bands are absent for the sheets with chain and dimer structures, because the electron system of the phenyl unit does not retain the symmetry of the Kagome lattice.

We evaluated tight-binding parameters of the Dirac cone and Kagome band in the different sheet conformations from their bandwidth. The calculated transfer integrals of the Dirac cone t_D are 17, 16, 14, and 10 meV for the planar, chain, dimer, and monomer conformations, respectively. Because of the narrow bandwidth, the Fermi velocities of the Dirac cone are 1.2×10^4, 1.4×10^4, 0.5×10^4, and 1.6×10^4 m/s for the planar, chain, dimer, and monomer conformations, respectively. Therefore, the porous hydrocarbon sheets are possible fields for strongly correlated electron systems that exhibit peculiar physical phenomena. A low Fermi velocity may cause large Fermi level instability even though the sheets possess zero density of states at E_F. For the Kagome bands, we also evaluated the transfer integral t_K. The calcu-

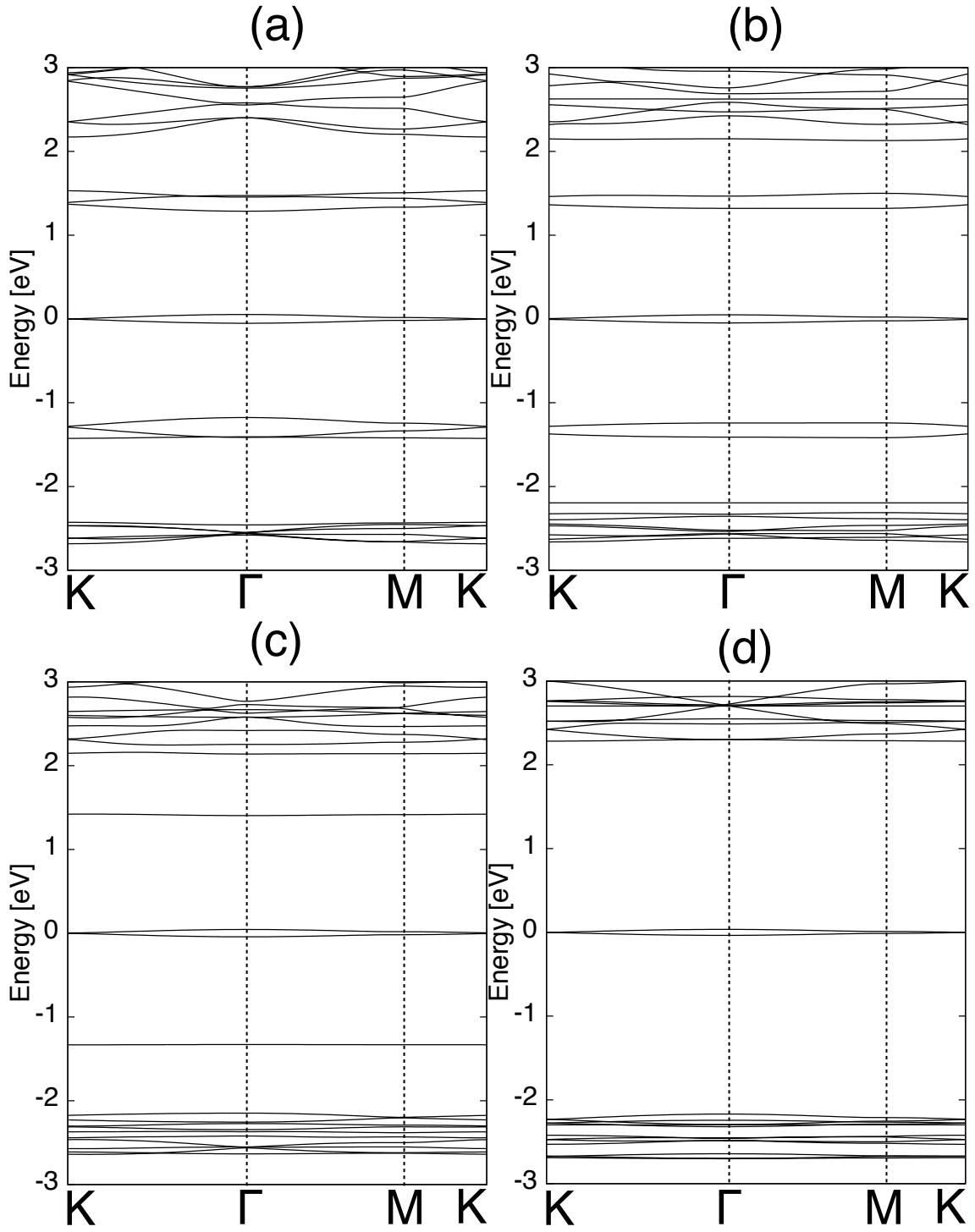

Figure 4.2: Electronic structures of porous hydrocarbon sheets consisting of phenalenyl and phenyl groups with (a) planar, (b) chain, (c) dimer, and (d) monomer conformation. Energies are measured from that of the Fermi level.

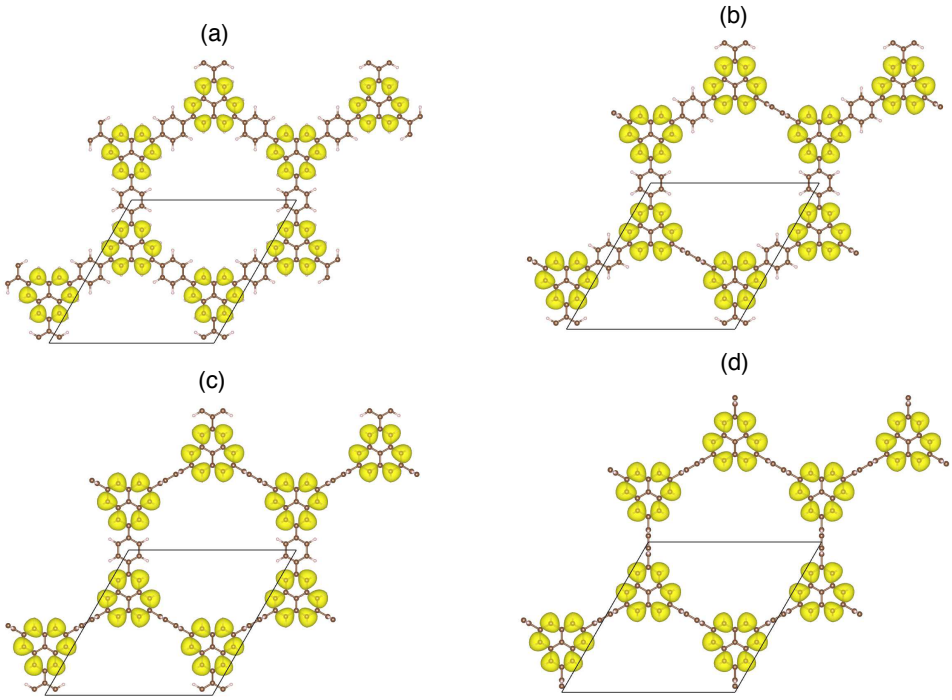

Figure 4.3: Isosurfaces of the wave function of the Dirac cone of porous hydrocarbon sheets consisting of phenalenyl and phenyl groups with (a) planar, (b) chain, (c) dimer, and (d) monomer conformation at the K point.

lated t_K are 27 and 21 meV for the planar and monomer conformations, respectively.

To clarify the physical origin of the Dirac cone in the planar system, we investigated the squared wave functions of the states at the K point [Figure 4.3(a)]. The wave functions are localized on phenalenyl units even though this porous hydrocarbon sheet possesses a 2D planar π electron network. By focusing on the wave function distribution within each phenalenyl, the state exhibits non-bonding nature in each phenalenyl unit. This indicates that the electron states associated with the Dirac cone can be ascribed to the singly occupied states of isolated phenalenyl monomers. In addition to the non-bonding nature within each phenalenyl unit, the wave function also exhibits non-bonding nature between adjacent phenalenyl units. Thus, the pair of linear dispersion bands at E_F is ascribed to the hexagonally arranged singly occupied state or a radical spin state of phenalenyl unit. Similar non-bonding nature within and between phenalenyl units was also found for the porous hydrocarbon sheets with chain, dimer, and monomer conformations [Figures 4.3(b)-4.3(d)].

Next, we examined the wave function associated with the Kagome band. Figure 4.4 shows the isosurfaces of the squared wave functions of the Kagome bands just below E_F at the Γ point. For the planar conformation, the wave functions are mainly distributed on the phenyl unit with the character of the HO states of phenyl molecules and are extended throughout the networks. Therefore, the flat dispersion band is ascribed to the delicate balance of the electron transfer among the HO state of the three phenyl units of the Kagome network, as in the case of the usual

Kagome flat band state. In contrast, for the chain and dimer conformations that lack the Kagome flat band, the states below E_F exhibit anisotropic nature, because of the orthogonality between the π states of the planar network and rotated phenyl units [Figures 4.4(b) and 4.4(c)]. For the monomer conformation, which possesses a Kagome flat band, the wave functions are more localized at the phenyl unit with the HO state nature and weakly extended throughout the network [Figure 4.4(d)]. This weak extended nature leads to the smaller t_K of the monomer conformation than that of the planar conformation.

4.4 Magnetic properties

The narrow band width of the Dirac cone of the porous hydrocarbon sheets results in a large density of states near E_F, which induces the Fermi level instability, causing magnetic ordering on the sheet, even though the sheets possess zero density of states at E_F because of the pair of linear dispersion bands at the K point. Figure 4.5 illustrates the spin density of the porous hydrocarbon sheets $n_s(\boldsymbol{r})$ evaluated by the equation

$$n_s(\boldsymbol{r}) = n_\alpha(\boldsymbol{r}) - n_\beta(\boldsymbol{r})$$

where $n_\alpha(\boldsymbol{r})$ and $n_\beta(\boldsymbol{r})$ are the charge densities of α and β spin components, respectively. We found that all the porous hydrocarbon sheets show spin polarization. Polarized electrons are localized on the phenalenyl units; the α and β spins are distributed on one of two sublattices of the phenalenyl units, as in the case of the spin density of an isolated phenalenyl. Because of the spin density of the phenalenyl unit, each phenalenyl unit possesses $S = 1/2$ radical spin corresponding to the difference between the numbers of two sublattices. Furthermore, the $S = 1/2$ spin of the phenalenyl unit exhibits antiferromagnetic (AF) and ferromagnetic (F) spin ordering throughout the sheets.

The total energies of the porous hydrocarbon sheets with AF and F states are listed in Table 4.1. The total energy of each sheet with spin polarization is about 300 meV lower than that of the corresponding sheet with non-magnetic states for all phenyl conformations. Furthermore, the total energy of the AF state is lower than that of the F state by 14, 9, and 4 meV for the planar, chain, and dimer conformations, respectively. These values indicate that the $S = 1/2$ spin on the phenalenyl unit interacts with its neighboring sites with weak singlet spin interaction J. The calculated spin interaction J per phenalenyl pair is about 10 meV. Note that the AF and F states are degenerate for the sheet with monomer conformation, because the total energies of theses states are the same within numerical error. Thus, this sheet does not exhibit long-range magnetic ordering. In addition, the rotation of the phenyl unit may turn off the spin interaction between adjacent phenalenyl units because of the monotonic decrease of the energy difference between the AF and F states. Therefore, the magnetic states of the porous hydrocarbon sheets can be tuned by controlling the orientation of phenyl units with respect to the phenalenyl units: the planar, chain, and dimer conformations are a $S = 1/2$ AF sheet, magnetically independent array of $S = 1/2$ AF chains, and magnetically isolated singlet-spin dimer network, respectively.

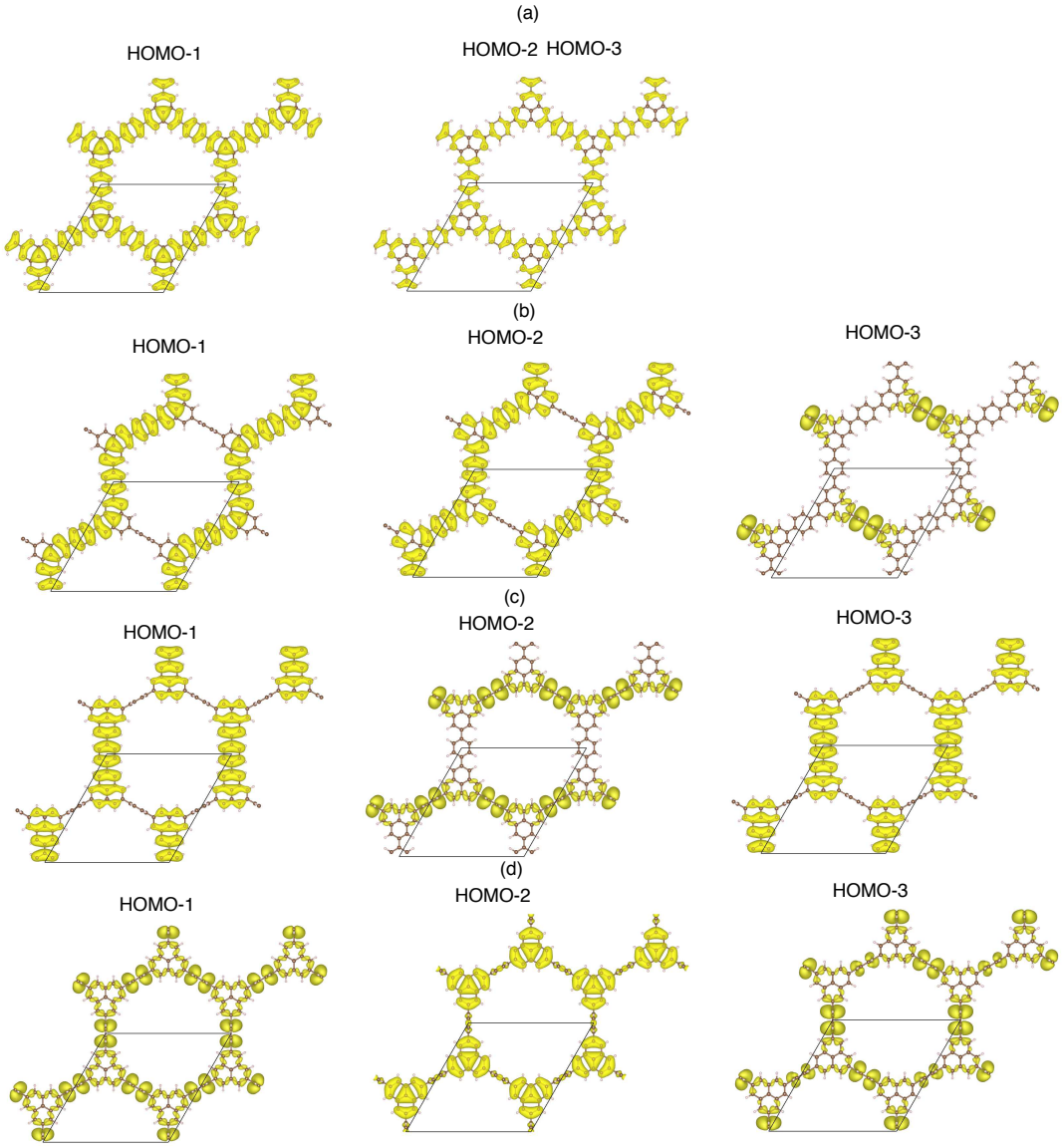

Figure 4.4: Isosurfaces of the wave function of the Kagome flat dispersion band of porous hydrocarbon sheets consisting of phenalenyl and phenyl groups with (a) planar, (b) chain, (c) dimer, and (d) monomer conformation at the Γ point.

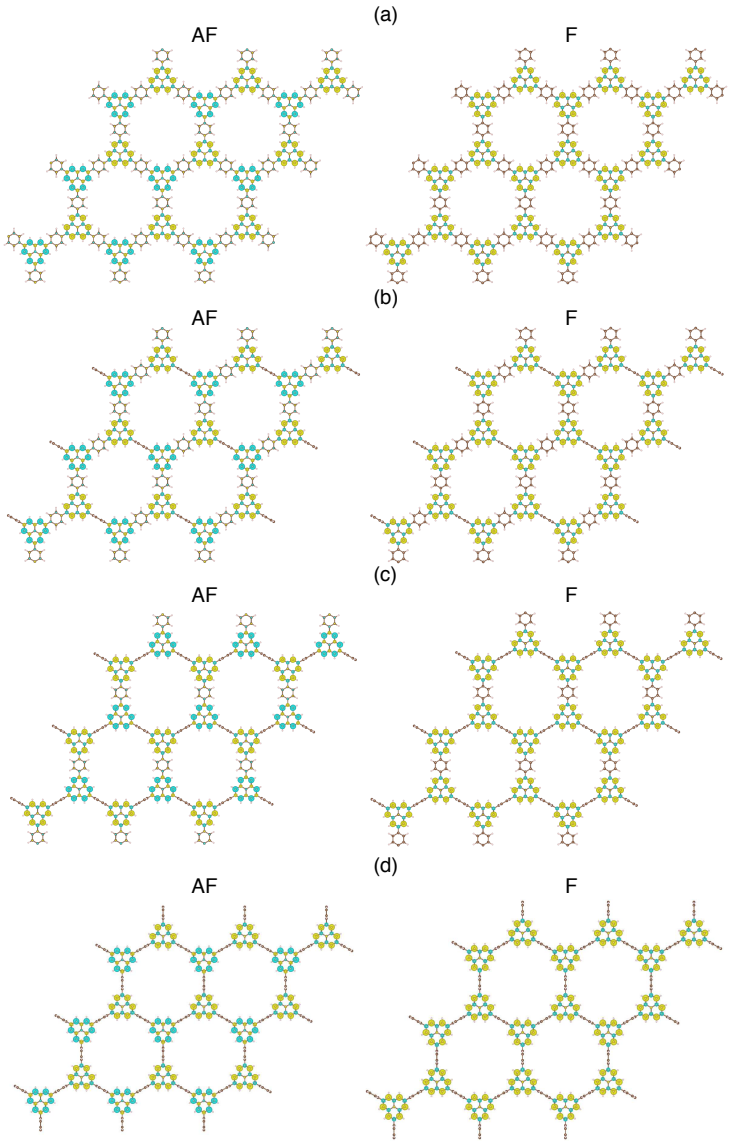

Figure 4.5: Spin densities of porous hydrocarbon sheets consisting of phenalenyl and phenyl groups with (a) planar, (b) chain, (c) dimer, and (d) monomer conformation with antiferromagnetic and ferromagnetic states. Colors indicate the sign of the polarized electron spin.

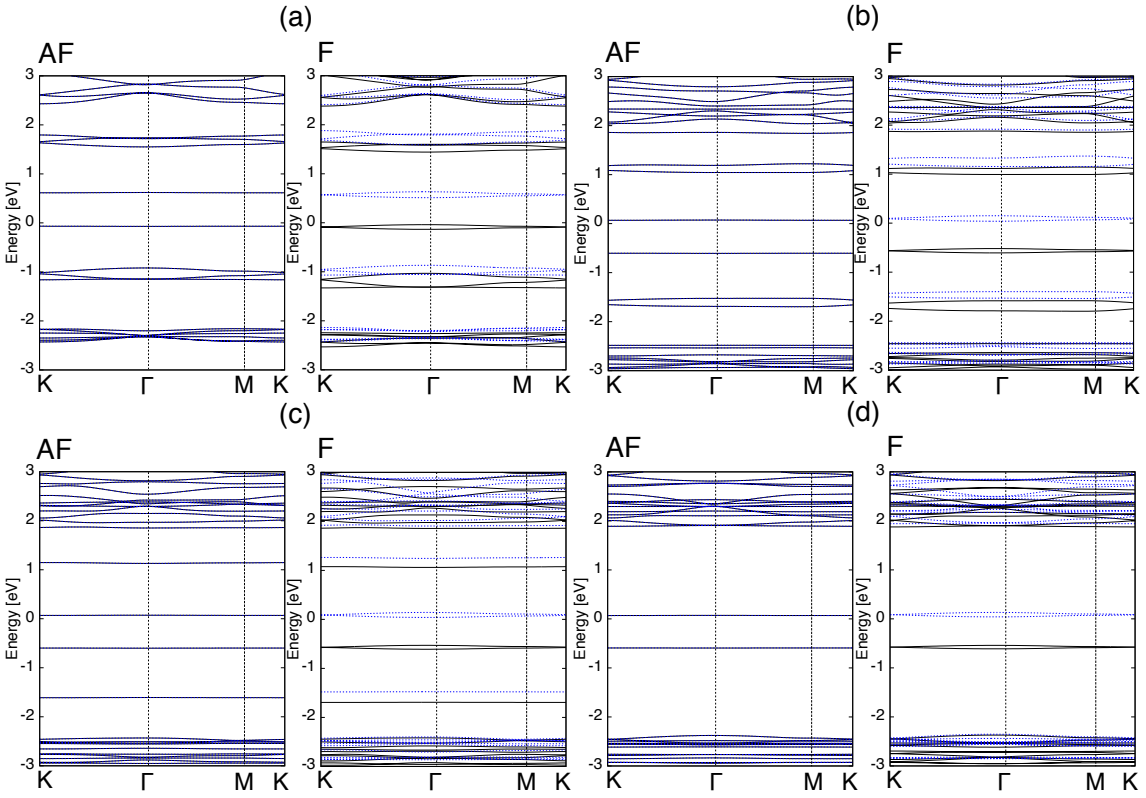

Figure 4.6: Electronic structures of porous hydrocarbon sheets consisting of phenalenyl and phenyl groups with (a) planar, (b) chain, (c) dimer, and (d) monomer conformation with antiferromagnetic and ferromagnetic states. The Fermi level is located at zero. Black lines and blue dotted lines denote majority and minority spin bands, respectively.

Figure 4.6 shows the electronic energy bands of the AF and F states of the porous hydrocarbon sheets with various phenyl conformations calculated by the spin-dependent GGA. In all cases, the spin polarization modulates the pair of linear dispersion bands at E_F. For the AF state, flat dispersion bands emerge above and below E_F instead of a Dirac cone because of the antiparallel coupling between two $S = 1/2$ radical spins of phenalenyl units. The energy gap between the upper and lower branches of the states associated with the spin polarization is 0.69-0.67 eV. For the F state, the Dirac cone is split into α and β spin states with a spin exchange energy of 0.65 eV, almost retaining its characteristic shape. In addition to the Dirac cone, electronic states near E_F are also modulated by the spin polarization. For instance, the Kagome band is split into α and β spin states with an energy difference of 0.16 eV.

The unusual electronic properties near E_F of the porous hydrocarbon sheets may exhibit further interesting physical properties upon hole injection into the Dirac cone and Kagome band. Because of the localized and extended natures of the electronic states associated with the Dirac cone and Kagome band, respectively, hole injection changes spin polarization in the porous hydrocarbon sheet. By injecting holes into the porous hydrocarbon sheet with the flat conformation by a counter

Table 4.2: Dependence of the number of polarized electron spins ($\Delta\rho$) on hole concentration.

Number of hole doping	1	2	3	4	5	6	7
$\Delta\rho$	1	0	1	2	3	2	1

planar electrode, we find that the number of polarized electron spins strongly depends on the number of holes injected [Table 4.2]. The spin density in the porous hydrocarbon sheet also strongly depends on the hole concentration [Figure 4.7]. For a low hole concentration corresponding to hole injection into the Dirac cone, the polarized electron spin exhibits qualitatively the same distribution as that of the undoped system. For a high hole concentration at which E_F crosses the Kagome band, the spin density exhibits different characteristics to that of the undoped case: The polarized electron spin is distributed on not only the phenalenyl but also the phenyl units, reflecting the extended nature of the wave functions associated with the Kagome band. Furthermore, in contrast to the non-doped network, the porous hydrocarbon sheet with a high hole concentration exhibits F spin ordering in its ground state. It should be noted that the carrier density to induce the magnetism associated with the Kagome flat band is about 0.8×10^{14} cm^{-2}. Thus, the magnetic state of the porous hydrocarbon sheet is tunable using ionic gating by the formation of electrical double layers (EDLs) which can inject carrier density up to 8×10^{14} cm^{-2} [61].

4.5 Energetics and magnetic property of phenalenyl dimer connected via phenyl

Since the phenyl prefers the tilted/rotated conformation in their ground state owing to the steric hindrance between hydrogen atoms attached to phenalenyl and phenyl, we further investigate the detailed energetics and spin interaction of a constituent unit of the porous hydrocarbon network. Here, we consider a phenalenyl dimer connected via phenyl as for the structural model of the the porous hydrocarbon network [Figure 4.8(a)]. Figure 4.8(b) show the total energy of the model molecule as a function of the rotational angle of phenyl with respect to the phenalenyl moieties. By rotating the phenyl, the total energy of the molecule monotonically decreases and possesses a minimum at the angle of about 35 degree. The total energy of the molecule with the rotation angle of 35 degree is lower by about 120 meV than that of the flat arrangement. Then, by further increase the angle, the total energy monotonically increase. Therefore, the phenyl connecting the phenalenyl units of the free-standing porous hydrocarbon sheet may be rotated by about 35 degree under the ambient condition as their ground state conformation. On the other hand, the porous hydrocarbon sheet may retain its flat conformation by adsorbing on appropriate substrates, such as graphene and h-BN, since the energy gain upon the interaction between the sheet and substrates compensate the energy loss upon the rotation of phenyl.

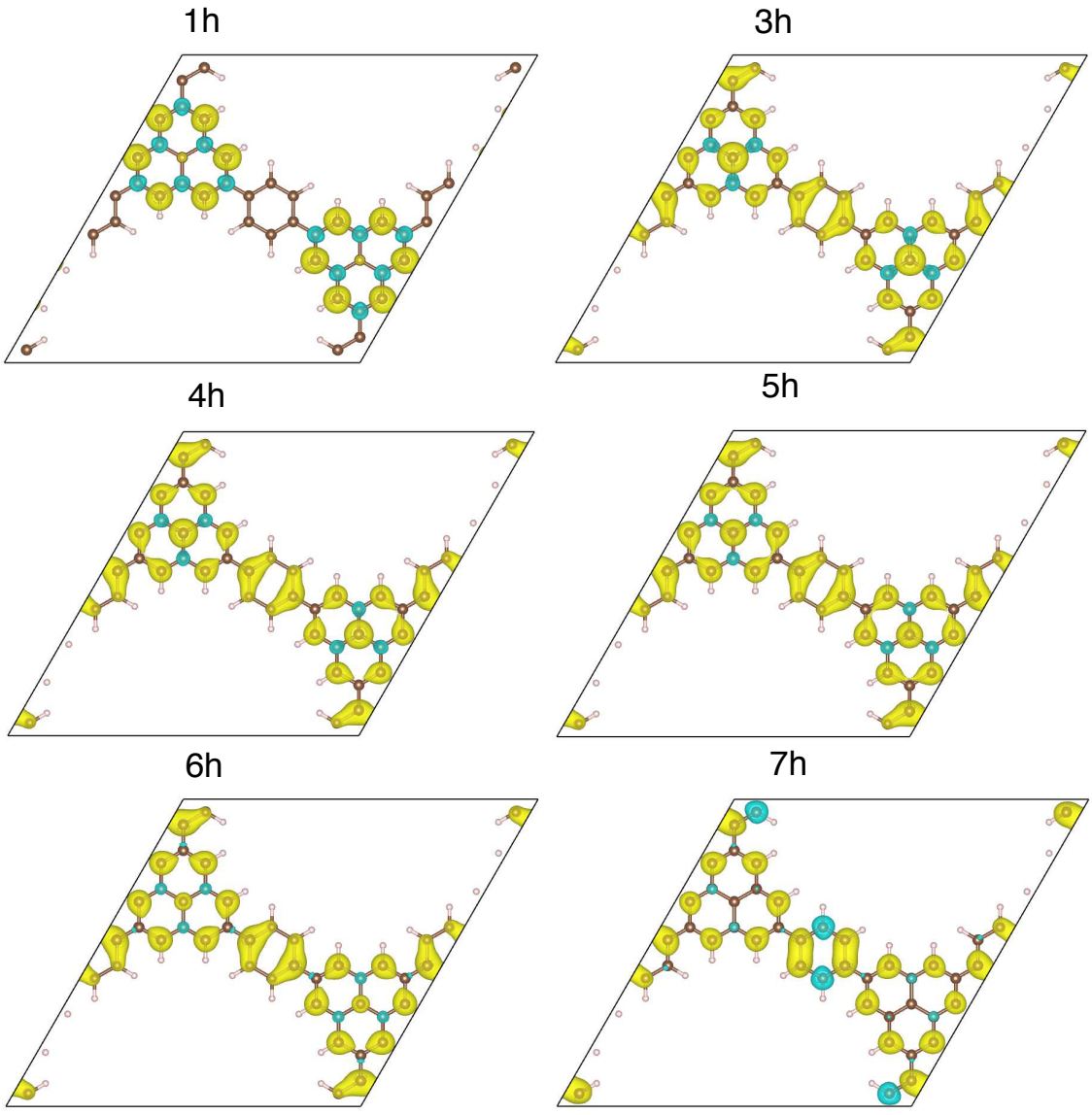

Figure 4.7: Spin densities of a porous hydrocarbon sheet consisting of phenalenyl and phenyl groups with planar conformation and hole concentrations of $1h$ to $7h$.

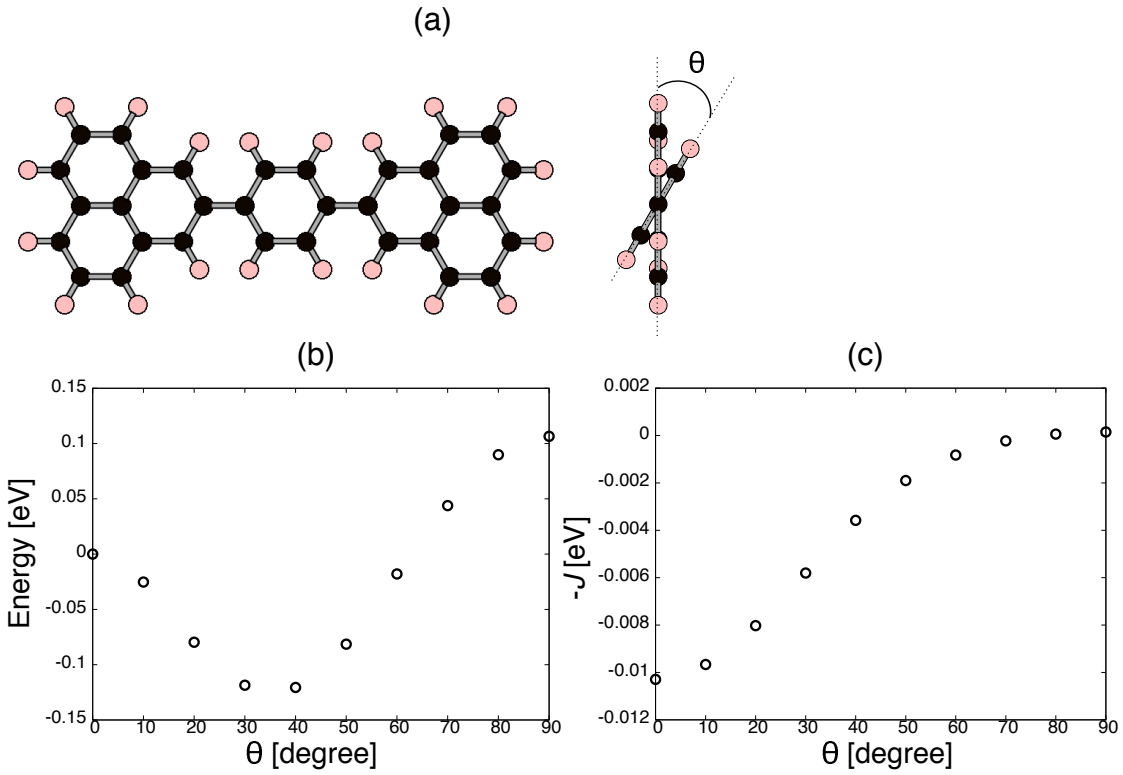

Figure 4.8: (a) A geometric structure of a phenalenyl dimer connected via phenyl (phenalenyl-phenyl-phenaleny). Black and pink circles denote carbon and hydrogen atoms, respectively. (b) Calculated total energy of phenalenyl-phenyl-phenaleny as a function of the rotational angle of phenyl unit. Energy is measured from that under the flat conformation. (c) Spin exchange energy of phenalenyl-phenyl-phenaleny as a function of the rotational angle of phenyl unit.

In addition to the energetics, it is worth to investigate how the spin interaction depends on the mutual rotational angle of the phenyl, because the spin interaction is terminated by the phenyl with the angle of 90 degree. Figure 4.8(c) shows the antiferromagnetic spin exchange energy J of the localized electron spin on phenalenyl moiety as a function of the rotational angle. The antiferromagnetic spin exchange interaction is the largest at the planar conformation and monotonically decrease with increasing the rotational angle of phenyl. The spin exchange interaction at the stable angle of 35 degree is approximately half of that of the flat conformation, indicating that the spin interaction among the phenalneyl still extend throughout the sheet under the conformation with tilted phenyl. Thus, the sheet still exhibit the AF spin ordering under the ground state conformation.

4.6 Conclusion

In this chapter, we theoretically investigated the possible structures of 2D porous hydrocarbon networks of sp^2 C consisting of phenalenyl and phenyl units. Phenalenyl formed a hexagonal lattice while phenyl formed a Kagome lattice because of their

alternating arrangement in which each phenalenyl is connected to three adjacent phenalenyls via phenyls. Our density functional theory calculations showed that the sheet exhibited unusual electronic structure near E_F: Radical electron states localized on phenalenyl units led to a Dirac cone at E_F. The Fermi velocity of the Dirac cone was one hundred times lower than that of graphene. Simultaneously, flat dispersion bands emerge below and above the Dirac cone arising from the HO and LU states of phenyl, respectively, which form a Kagome lattice. Slow massless electrons at E_F lead to magnetic spin ordering on the porous hydrocarbon sheet with AF and F states. The spin exchange interaction between adjacent radical spins on phenalenyl units is $J = 10$ meV per pair, preferring the singlet coupling. We also demonstrated that the electronic structures and spin states of the porous hydrocarbon networks can be tuned by tilting the phenyl unit connecting adjacent phenalenyl via a single bond, lowering the dimensionality of the electron system near E_F.

Chapter 5

Magnetic Properties of Graphene Quantum Dots Embedded in h-BN Sheet

In this chapter, we study the energetics and magnetic properties of two graphene dots with triangular shapes embedded in an h-BN sheet, using density functional theory with generalized gradient approximation.

5.1 Introduction

Because of the similar ionic radii, boron (B) and nitrogen (N) atoms are the representable elements used to form hybrid structures with graphene. BC_3 and BC_2N compounds with graphitic networks have been synthesized, and their physical properties have been intensively studied [62, 63, 64, 65, 66, 67, 68]. In such compounds, the π network of graphene is segmented by the foreign B and N atoms because of their electronic structure difference. Thus, their electronic structures strongly depend on the atomic arrangements of consistent elements in a hexagonal network. Furthermore, recent advances in the synthesis techniques for 2D materials with atom thickness have realized a bulk grain boundary between graphene and h-BN [69, 70, 71, 72, 73, 74, 75, 76, 77]. It has been theoretically predicted that the h-BN domain perfectly terminates the π states of graphene at the border, leading to border-localized states at the zigzag border of C and B/N that possess similar characteristics to the edge state of graphene with a zigzag edge [78]. Furthermore, by designing the border shape, graphene domains can exhibit ferrimagnetic spin ordering because of the imbalance between two sublattices of the domain [17, 79]. Therefore, graphene domains embedded in h-BN may be utilized for nanoscale spin dots in spin devices. Indeed, an isolated triangular graphene domain embedded in h-BN possess spin polarized states as their ground states. However, it is unclear whether there is a spin exchange interaction between graphene dots in h-BN, which are important for utilizing the hybrid structures for spin devices. Therefore, in this chapter, we aim to investigate the energetics and spin exchange interaction J of triangular graphene dots in terms of their spacing and arrangement using the DFT

with the GGA.

All calculations were performed within the framework of DFT [19, 20] using the STATE code [37, 60, 80, 81]. For calculation of the exchange-correlation energy among the interacting electrons, we used the GGA with a Perdew-Burke-Ernzerhof functional form [23]. To investigate the spin polarized states of graphene dots in h-BN, the spin degree of freedom was taken into account for all calculations except for calculations of non-magnetic states as the energy reference. Vanderbilt ultrasoft pseudopotentials were used to describe the electron-ion interaction [26]. The valence wave functions and charge density were expanded in terms of the plane waves with cutoff energies of 25 and 225 Ry, respectively, which sufficiently describe the electronic structure and energetics of h-BN and graphene [80, 81]. Structural optimization was performed until the remaining forces on each atom were less than 5 mRy/Å for each dot configuration. Integration over the Brillouin zone was carried out using the Γ point sampling which corresponds with 8×8 $\boldsymbol{k}$-point mesh for the primitive cell of h-BN, resulting in the sufficient convergence in the total energy of h-BN within 1 meV per atom to the total energy obtained by the equidistance 40×40 $\boldsymbol{k}$-point mesh.

5.2 Structural model

In this chapter, we focused on a triangular graphene dot consisting of 13 C atoms (a phenalenyl structure) as a representative dot with spin polarization embedded in h-BN because h-BN possesses triangular vacancies with zigzag edges that can be filled by the phenalenyl unit. To investigate the energetics and spin–spin interaction of graphene dots in h-BN in terms of the inter-dot spacing, we placed two phenalenyl units with five inter-unit distances, ranging from 2.5- to 12.5-Å spacing between dots, in a super cell of h-BN sheet with 16× $4\sqrt{3}$ (40 × 17 Å) lateral periodicity [Figure 5.1]. To elucidate the influence of the border atomic arrangements, we considered border configurations consisting dominantly of NC [Figure 5.1(a)], BC [Figure 5.1(b)], and mixed [Figure 5.1(c)] borders. Depending on the choice of h-BN sheet with graphene dots, the unit cell contains 26 C, 116 N, and 114 B atoms for the heterosheet with the NC border, 26 C, 114 N, and 116 B atoms for the heterosheet with the BC border, and 26 C, 115 N, and 115 B atoms for the heterosheet with the mixed border. To exclude the unphysical effects arising from the periodic images normal to the sheet, the lattice parameter normal to the sheet was set at 10.0 Å.

5.3 Energetics

First, we check the stability and atomic structures of graphene dots in h-BN with NC and BC borders. The heterosheets of h-BN and a triangle graphene dot possess 6 N-C and 3 B-C bonds for the NC border, and 3 N-C and 6 B-C bonds for the BC border. The heterosheets retain their planar structure irrespective of the border structure, indicating that the structure is energetically stable. This fact indicates that the most of the graphene dots embedded in h-BN act as isolated quantum dots. Table 5.1 lists the optimized bond lengths of heterosheets consisting of h-BN and

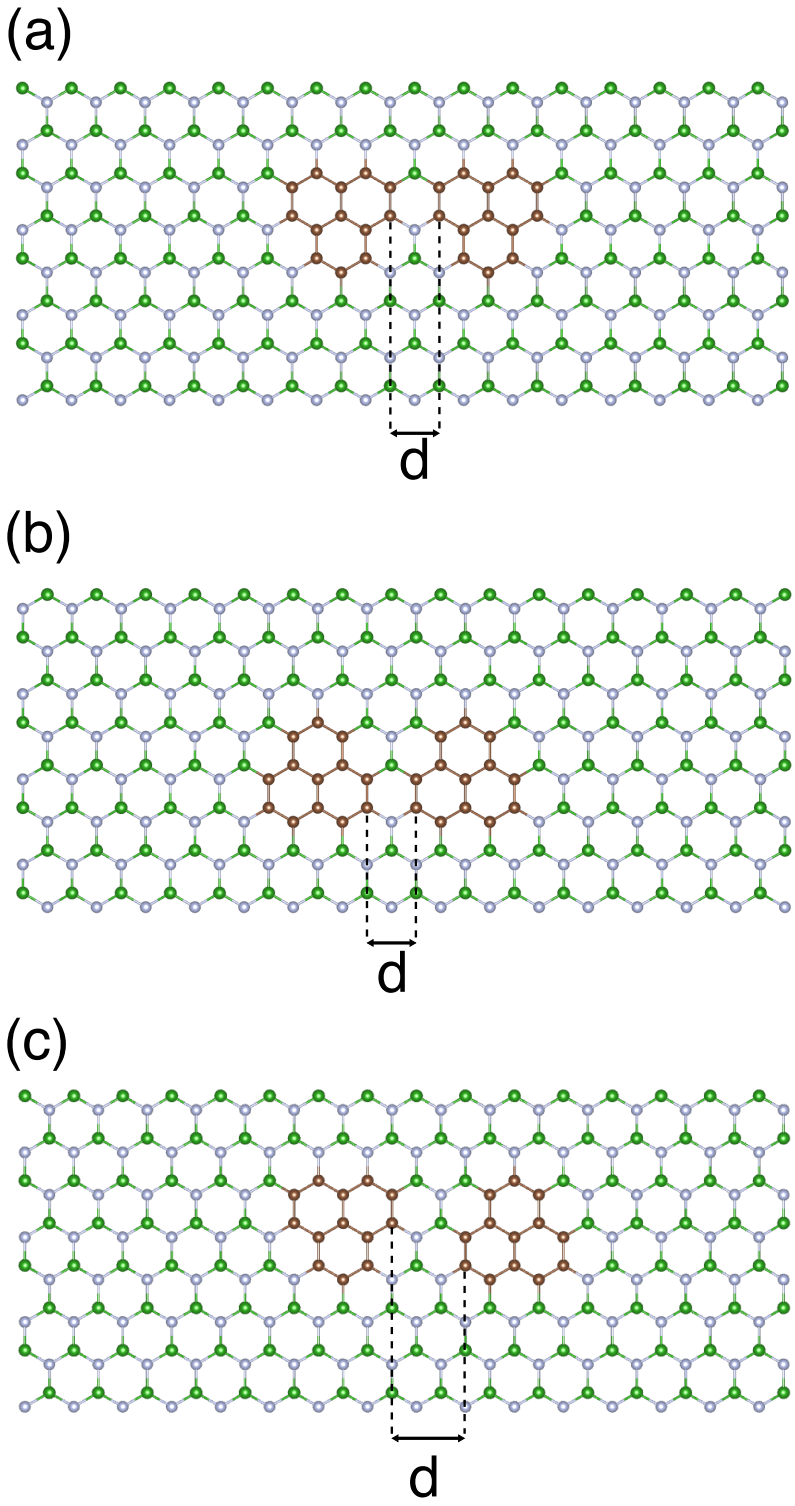

Figure 5.1: Structural models of geometries of two graphene dots embedded into h-BN with (a) NC border, (b) BC border, and (c) mixed border. Brown, gray, and green balls denote C, N, and B atoms, respectively. d denotes the inter-dot spacing of adjacent graphene dots.

Table 5.1: Bond lengths of NC border d_{NC} (Å) and Bond length of BC border d_{BC} (Å)

bond	d_{NC}	d_{BC}
B-C [Å]	1.52	1.53
N-C [Å]	1.42	1.43
C-C [Å]	1.42-1.45	1.44-1.47

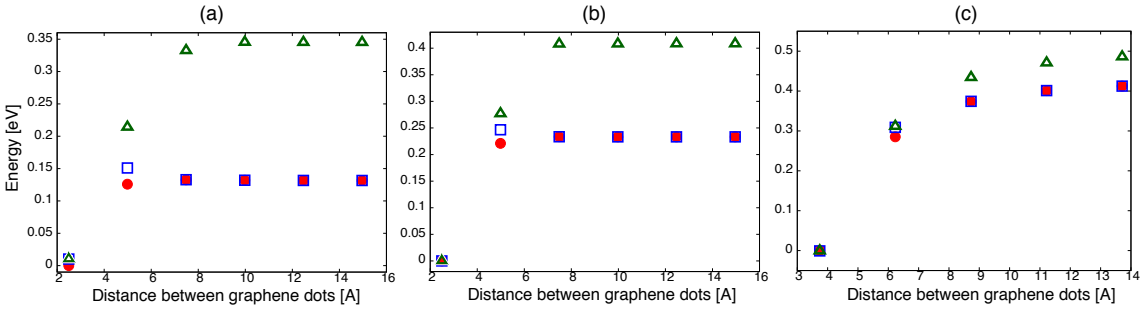

Figure 5.2: Relative total energies of graphene dots embedded in h-BN with (a) NC, (b) BC, and (c) mixed borders as a function of inter-dot spacing. Energies are measured from that of the dots with the closest inter-dot spacing. Circles, squares, and triangles denote the total energies calculated for the antiparallel initial spin configuration, parallel initial spin configuration, and non-magnetic calculations, respectively.

graphene dots with a triangular shape. The optimized bond lengths of B-C and N-C bonds are 1.52 Å and 1.42 Å, respectively. The heterobonds at the border lead to variation in the C-C bond lengths in the graphene dot ranging from 1.42 to 1.47 Å.

Figure 5.2 shows the relative total energy of graphene dots in h-BN as a function of the distance between dots. The total energy has the lowest value at the closest inter-dot spacing, i.e. 2.5 Å, for NC and BC borders and at 3.75 Å for the mixed border. The energy monotonically increases with increasing inter-dot spacing and immediately becomes saturated at 0.21 and 0.12 eV for NC and BC borders, respectively, at the inter-dot spacing of 7.5 Å. These energies correspond to the inter-dot binding energies of graphene dots in h-BN. The lower total energy of the dots under the closest arrangement arises from the fact that the electronic states of the dots interact with each other, leading to a decrease in the kinetic energy of the dots. The deep local potential of the N atoms at the border leads to a larger binding energy of the dots with the NC border than those with BC borders because the N atoms at the border efficiently connect the two graphene dots. For the mixed border, the energy exhibits a different feature: It gradually increases with increasing inter-dot spacing and saturates at 0.4 eV under the spacing of 11.0 Å. In this case, the presence of both NC and BC borders causes the mixture of the two sublattices on graphene dot networks, leading to substantial mixing of the wave functions.

For dots with spacings of 5.0 Å or larger, the total energies of spin polarized

states are lower than that of the nonmagnetic states, as obtained by the GGA in which the spin degree of freedom is taken into account. This fact indicates that graphene dots with triangular shape embedded in h-BN exhibit spin polarization: By evaluating the numbers of electrons of majority and minority spin components, it can be concluded that triplet and singlet spin states may exist as the stable states. For dots with the inter-dot spacing of 5.0 Å, the total energy of the antiparallel spin coupling state (the singlet spin arrangement) is lower than that of the parallel spin coupling state (the triplet spin arrangement) by 25 meV for both the NC and BC borders, so that the singlet arrangement is the ground state spin arrangement for the two dots under small inter-dot spacing. On the other hand, the total energy of both spin states degenerates under larger inter-dot spacings, indicating that the dots can be regarded as isolated spin dots in h-BN.

5.4 Magnetic properties

It is important to directly check the distribution of the polarized electron spins on the graphene dots in h-BN. Figures 5.3, 5.4, and 5.5 show the spin densities of graphene dots in an h-BN sheet with NC, BC, and mixed borders, respectively. It is clear that the majority spin is distributed on the sublattice A of graphene dots (edges and the center of the dot), while the minority spin is distributed on the sublattice B of the dot. The absolute value of the spin density at the border is larger than that for the inner region. According to the ferrimagnetic spin density through two sublattices of the graphene dot and the imbalance between the numbers of sublattices, each dot possesses an $S = 1/2$ spin state as its ground state. Thus, each graphene dot can be regarded as an $S = 1/2$ localized spin system, leading to the various spin states by arranging them into the h-BN sheet. Hereafter, we investigate the spin interaction between two $S = 1/2$ graphene dots embedded into h-BN with NC and BC borders.

For the shortest inter-dot distance, the graphene dots do not show parallel spin coupling states for all borders. On the other hand, the dot with NC borders possesses an antiparallel spin coupling state at the inter-dot spacing of 2.5 Å [Figure 5.3(a)], while, for the BC border, the antiparallel spin coupling state is absent at that inter-dot spacing [Figure 5.4(a)]. In addition, for the mixed border, the dots exhibit an antiparallel spin coupling state at the inter-dot spacing of 3.74 Å [Figure 5.5(a)]. The dots with a separation of 5.0 Å or larger possess both parallel and antiparallel spin arrangements, in which polarized electron spins are distributed at the border between graphene dots and h-BN. At the borders, the polarized electron spins exhibit different features for NC and BC borders: For the NC border, the spin distribution has a nodal line along the triangular border between the graphene dots and h-BN [Figure 5.3]. In contrast, for the BC border, the spins are distributed at the border with bonding nature leading to a bonding π charge density on the heterobonds at the border [Figure 5.4]. The characteristic spin densities are also found in the NC and BC borders in the heterosheet with mixed borders [Figure 5.5].

By considering the energy difference between antiparallel and parallel spin coupling states, we can estimate the spin–spin interaction or the spin exchange interac-

tion J for a 2D Heisenberg model between two graphene dots with triangular shape embedded in an h-BN sheet. Figure 5.6 shows the spin exchange interaction J between graphene dots as a function of inter-dot spacing. With an inter-dot spacing of 5.0 Å, the spin–spin interaction between dots is the largest among all inter-dot spacings. The calculated energy J is 50 meV with antiparallel spin coupling for dots with both NC and BC borders. For the mixed border, the maximum J is 46 meV with antiparallel coupling at the spacing of 6.25 Å. With increasing spacing, J rapidly decreases and vanishes: For dots with the inter-dot spacing of 7.5 Å, the calculated J is 8 meV with antiparallel spin coupling for both NC and BC borders. The J is exactly zero for dots with the inter-dot spacing of 10.0 Å or larger. This indicates that the spin exchange interaction J between graphene dots in h-BN is a short-range interaction of which the range is less than 10.0 Å. Therefore, to apply graphene dots in h-BN as 2D arranged quantum spin dots, graphene dots have to be arranged with inter-dot spacings of 10.0 Å or less. In addition, the interaction J is tunable by controlling the inter-dot spacing.

5.5 Electronic structures

To clarify the origin of the spin polarization and the characteristic spin distribution, we investigate the partial density of states (PDOS) and the wave function distribution of graphene dots embedded in h-BN sheet near the E_F. Figure 5.7 shows the PDOS of the antiparallel and parallel spin coupling states of graphene dots in h-BN near the E_F. All heterosheets are semiconductors with gaps of approximately 0.3 eV depending on the inter-dot spacing and arrangement. The small gap is ascribed to the presence of the graphene dots, because pristine h-BN is an insulator with a large energy gap of 5.0 eV. We also find that the most of Kohn–Sham states in the energy gap between valence and conduction states of h-BN in Figure 5.7 possess localized nature on C atoms with small B/N components. This indicates that the states near the gap are mainly localized on the graphene dots and that the h-BN sheet perfectly terminates the states associated with the graphene dots. The electronic structures of the sheets depend on the inter-dot spacing: PDOS peaks near the gap of the sheet with NC and BC borders for the inter-dot spacing of 5.0 Å is broader than those for the inter-dot spacing of 10.0 Å. This fact indicates that the dot substantially interacts with the other dot under the inter-dot spacing of 5.0 Å.

Figures 5.8, 5.9, and 5.10 show the squared wave functions of the HO and LU states of graphene dots embedded in h-BN. These states attributed to the spin polarization are localized on one of two dots, indicating that the dots are perfectly separated from each other except at inter-dot spacings of 2.5 and 5.0 Å. In the case of the closest dot arrangement, the wave function slightly spills out to the adjacent dots. This characteristic of the HO and LU states suppresses the spin polarization of the dots. For dots with a parallel spin coupling state under 5.0 Å spacing, the wave functions slightly overlap on B and N atoms situated at the middle of the dots for NC and BC borders, respectively, leading to substantial band splitting in the HO states, as discussed above. In addition to the localized nature of the HO and LU states, they are primarily distributed at the NC and BC borders with antibonding and bonding

natures, respectively, which corresponds to the distribution of the polarized electron spins. The emergence of the antibonding and bonding natures of the NC and BC borders, respectively, can be interpreted using the simple electron counting model on the schematic band diagram shown in Fig. 5.7 (j). Because of the covalent nature of B-C and N-C bonds, the states at the border split into bonding and antibonding states that are filled by electrons depending on the border atom species. Accordingly, the partially occupied states localized on the borders of the triangular graphene dots and h-BN cause the antiparallel and parallel spin polarization on the graphene dots with the border distribution nature of the polarized electron spin.

5.6 Conclusion

We studied the electronic structures and energetics of 2D heterosheets consisting of h-BN and triangle graphene dots, which are known to be phenalenyl molecules, as polycyclic hydrocarbon molecules with radical spin based on first-principles total-energy calculation in the framework of density functional theory. Our spin polarized density functional theory calculations with GGA revealed that the graphene dots exhibit spin polarization on the border and the spins between the dots possess parallel and antiparallel spin arrangements as metastable states. Our calculations also show that the spin exchange interaction J between two spins has the largest value of $J = 50$ meV with antiparallel spin coupling at the inter-dot spacing of 5.0 Å. This spin interaction is a short-range interaction, of which the range is less than 10.0 Å, indicating that the precise nanometer-scale control of the inter-dot spacing is necessary for designing spin devices associated with the localized spin on the graphene dots in h-BN. The graphene dots in h-BN prefer the closest arrangements because of the localized nature of the electron states at the borders. The results indicate that triangle graphene dots in h-BN can act as spin dots operating at temperatures up to approximately 250 K.

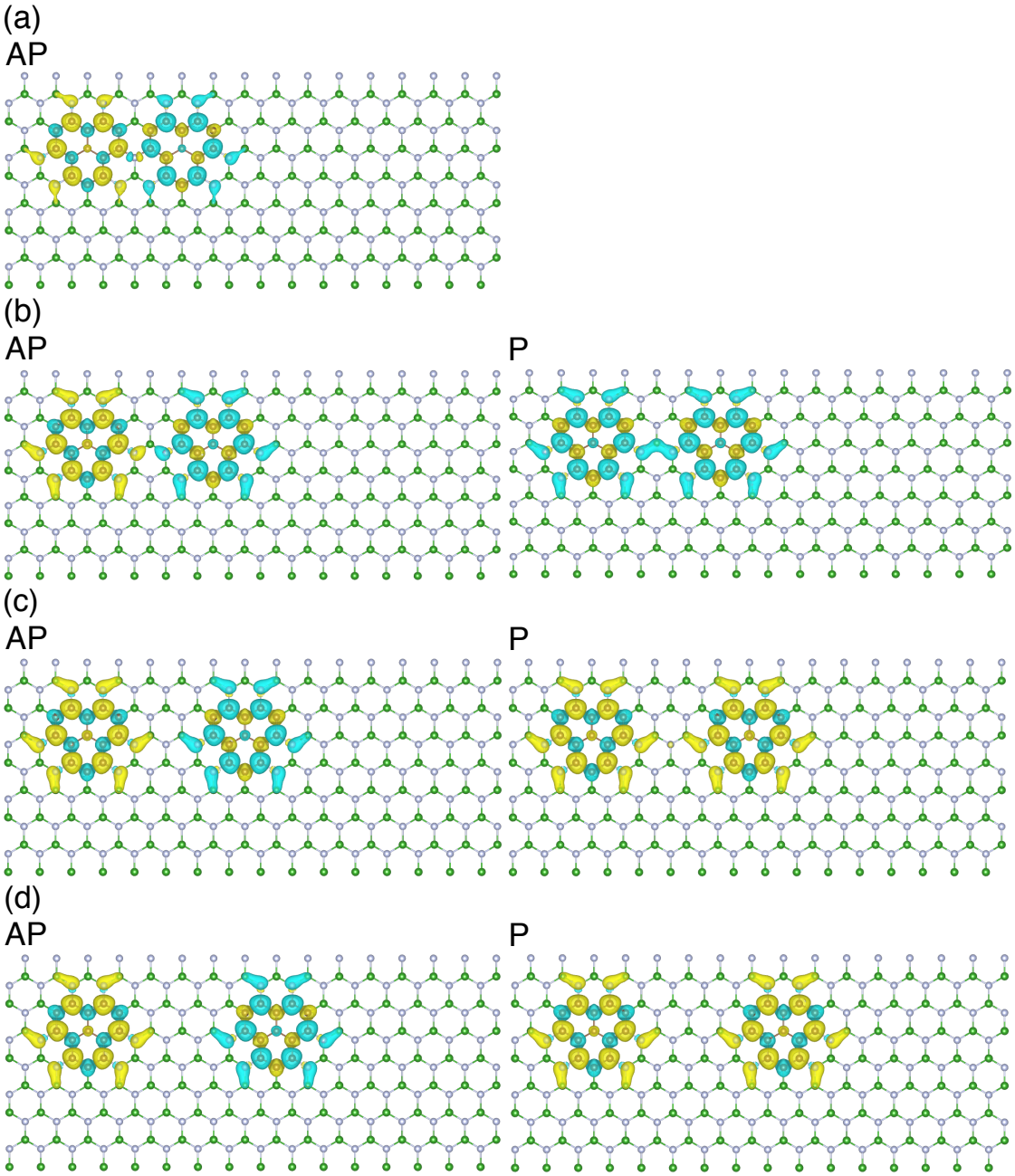

Figure 5.3: Isosurfaces of spin densities of graphene dots in h-BN with NC borders and inter-dot spacings of (a) 2.5, (b) 5.0, (c) 7.5, and (d) 10.0 Å. In each panel, left and right isosurfaces denote the spin density of antiparallel and parallel spin coupling states, respectively. Brown, gray, and green circles denote C, N, and B atoms, respectively.

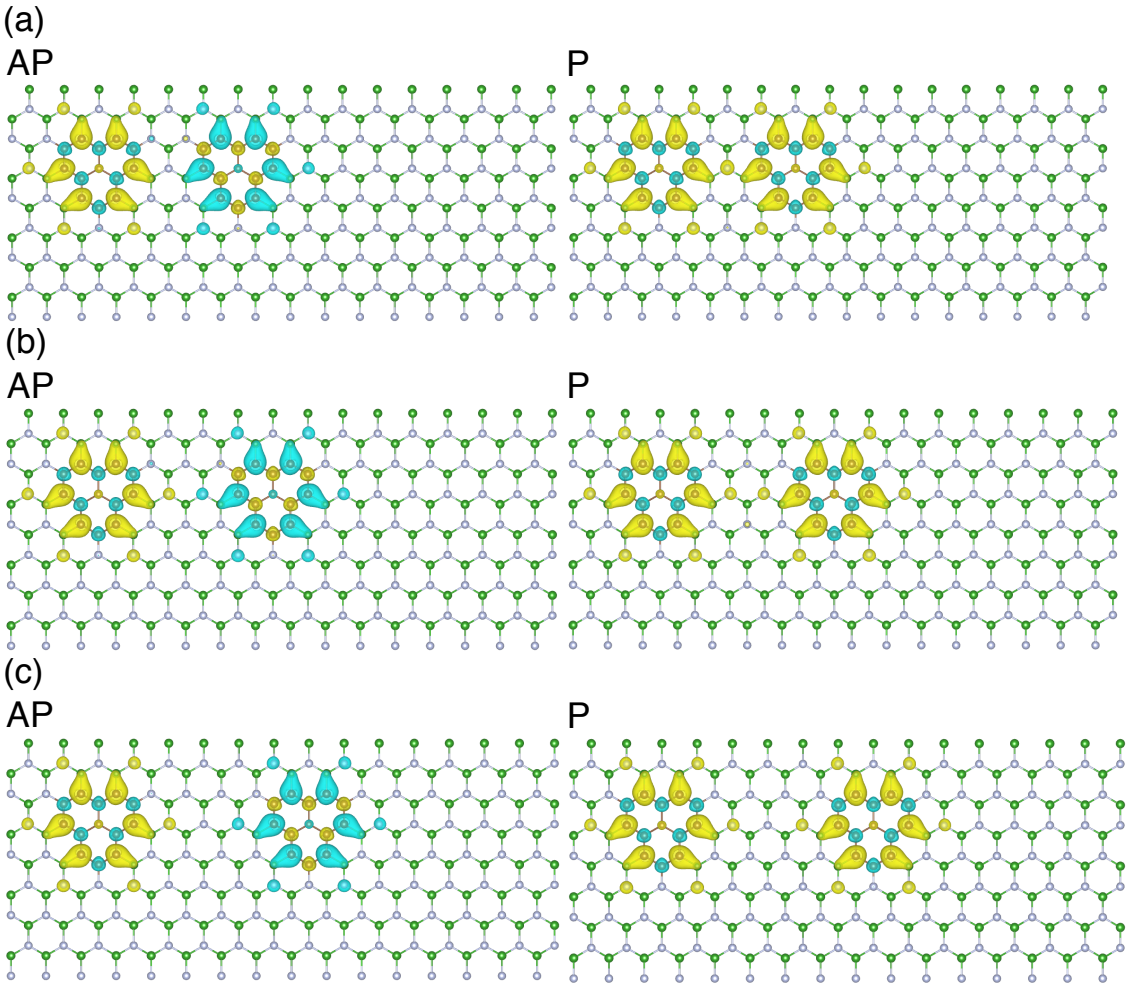

Figure 5.4: Isosurfaces of spin densities of graphene dots in h-BN with BC borders and inter-dot spacings of (a) 5.0, (b) 7.5, and (c) 10.0 Å. In each panel, left and right isosurfaces denote the spin density of antiparallel and parallel spin coupling states, respectively. Brown, gray, and green circles denote C, N, and B atoms, respectively.

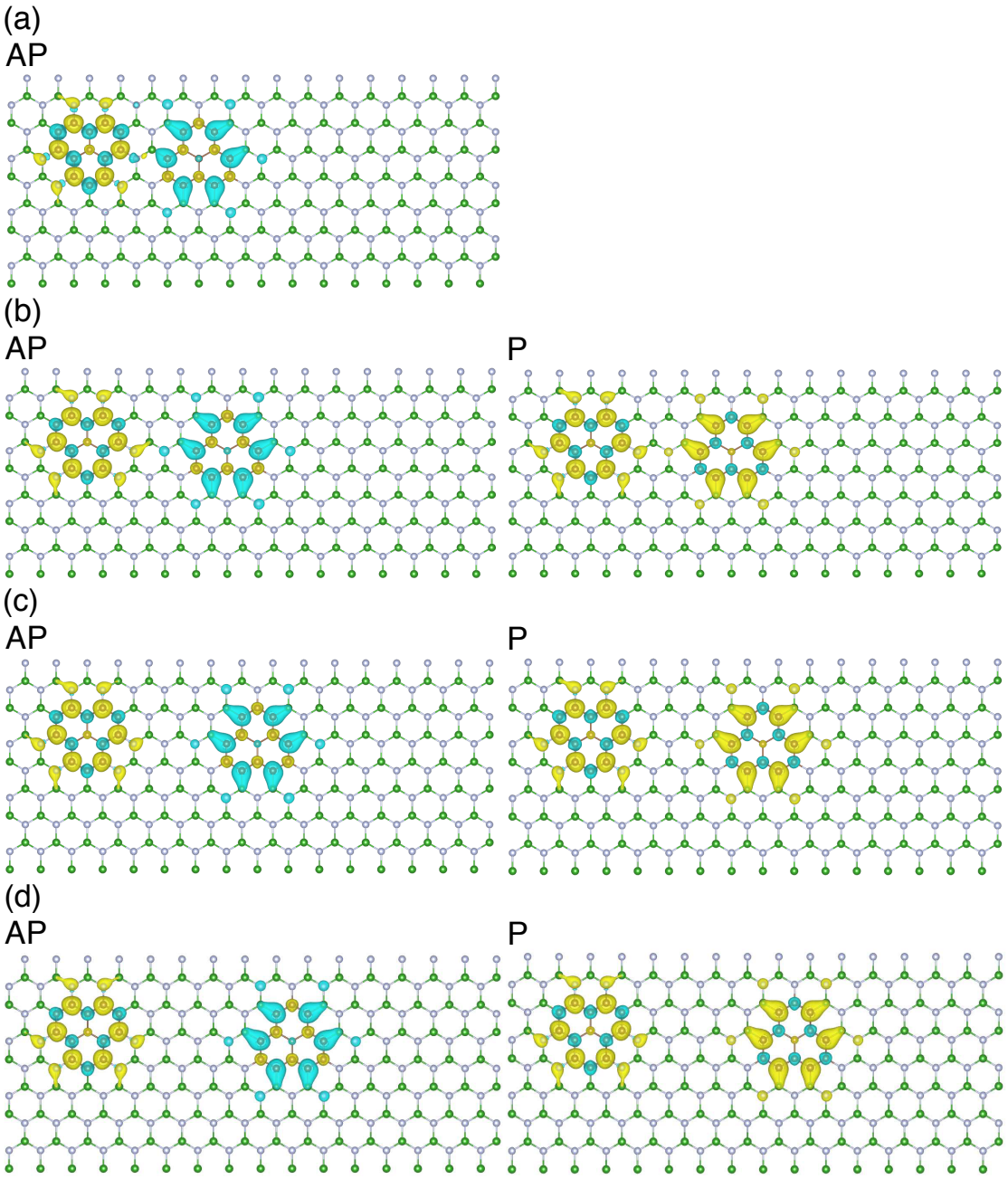

Figure 5.5: Isosurfaces of spin densities of graphene dots in h-BN with mixed borders and inter-dot spacings of (a) 3.75, (b) 6.25, (c) 8.75, and (d) 11.25 Å. In each panel, left and right isosurfaces denote the spin density of antiparallel and parallel spin coupling states, respectively. Brown, gray, and green circles denote C, N, and B atoms, respectively.

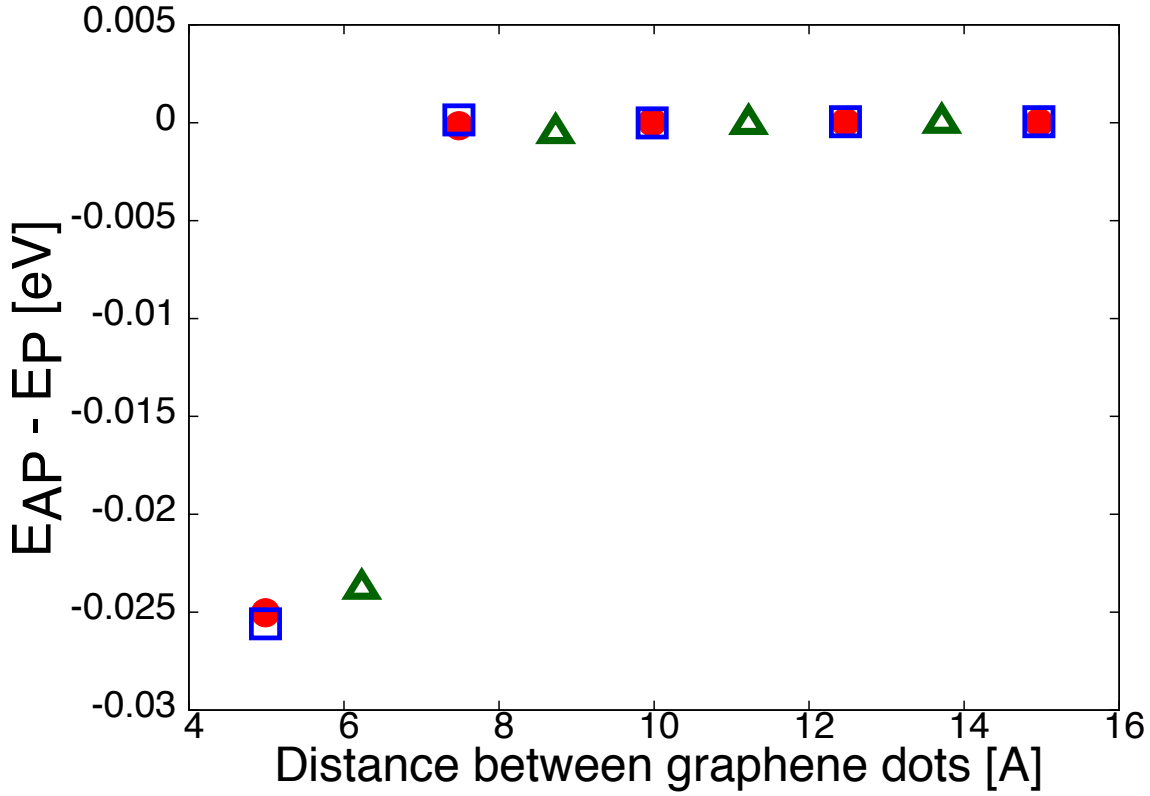

Figure 5.6: Energy difference between antiparallel and parallel spin coupling states as a function of the inter-dot spacing. Circles, squares, and triangles denote the J for NC, BC, and mixed borders, respectively.

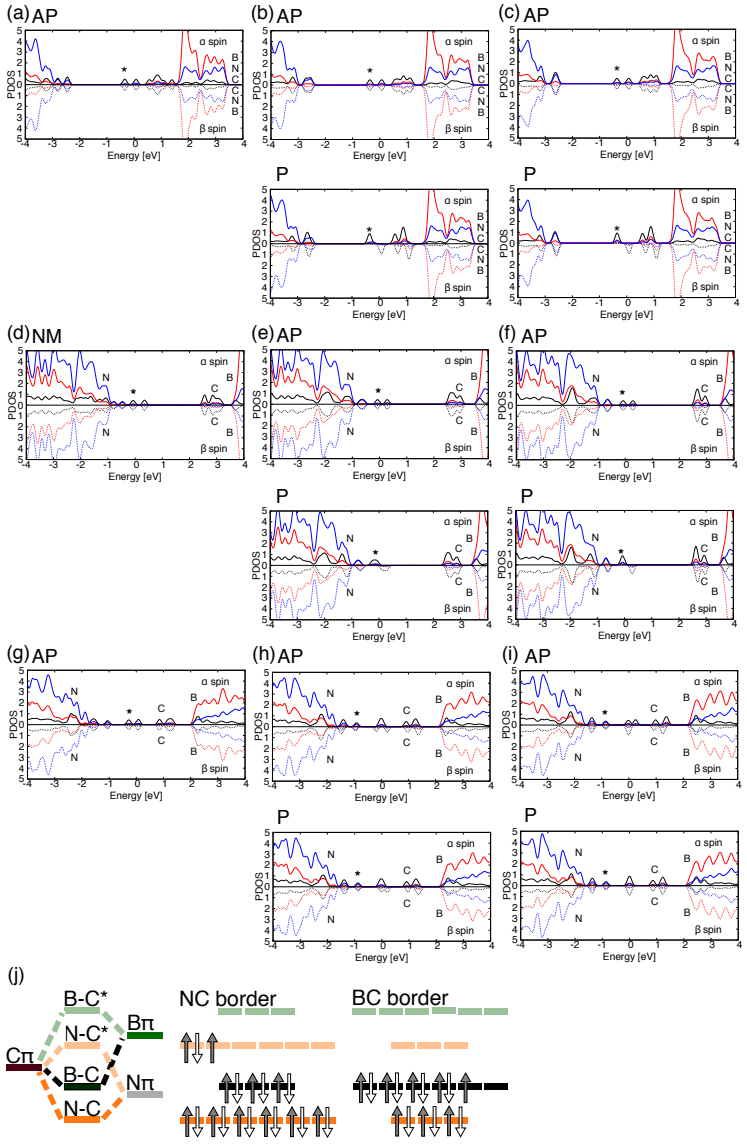

Figure 5.7: Partial density of states (PDOS) of the antiparallel (AP) and parallel (P) spin coupling states of graphene dots in h-BN with NC borders and inter-dot spacings of (a) 2.5, (b) 5.0, and (c) 10.0 Å. PDOS of the AP and P spin coupling states of graphene dots in h-BN with the BC borders and inter-dot spacings of (d) 2.5, (e) 5.0, and (f) 10.0 Å. For the inter-dot spacing of 2.5 Å, PDOS of the non-magnetic (NM) state is only shown, since it does not exhibit any magnetic ordering. PDOS of the AP and P spin coupling states of graphene dots in h-BN with mixed borders an inter-dot spacings of (g) 3.75, (h) 6.25, and (i) 11.25 Å. Unit of the PDOS is states/eV. Energies are measured from that of the Fermi level. Red, blue, and black lines denote PDOS for N, B, and C atoms, respectively. Solid and dotted lines denote the α and β spin states for each atomic element, respectively. Asterisks denote the highest occupied states. (j) A schematic energy diagram of the border between graphene dots and h-BN.

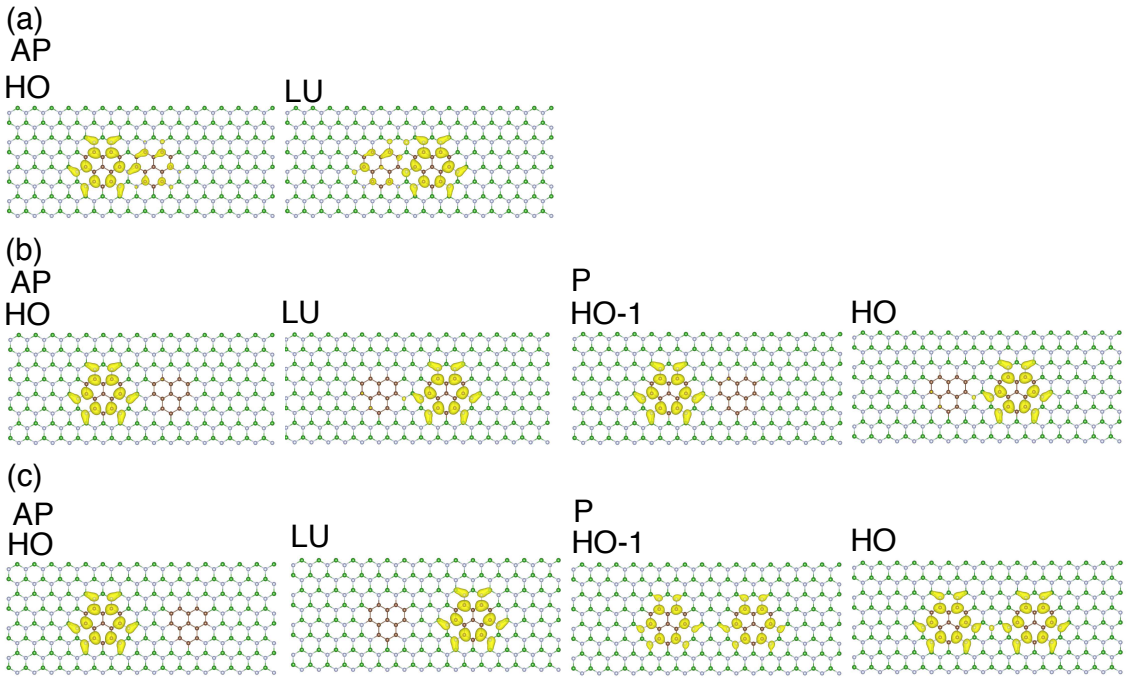

Figure 5.8: Isosurfaces of squared wave functions of antiparallel (AP) and parallel (P) spin coupling states of graphene dots in h-BN with NC borders and inter-dot spacings of (a) 2.5, (b) 5.0, and (c) 10.0 Å. Brown, gray, and green circles denote C, N, and B atoms, respectively.

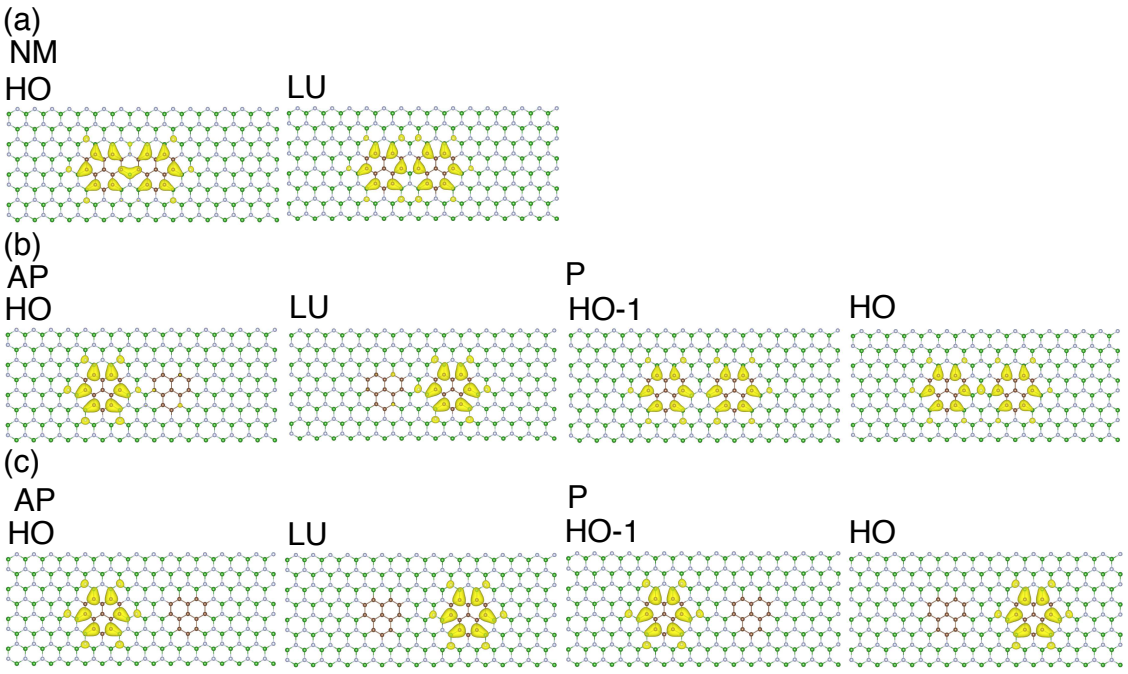

Figure 5.9: Isosurfaces of squared wave functions of antiparallel (AP) and parallel (P) spin coupling states of graphene dots in h-BN with BC borders and inter-dot spacings of (a) 2.5, (b) 5.0, and (c) 10.0 Å. Brown, gray, and green circles denote C, N, and B atoms, respectively.

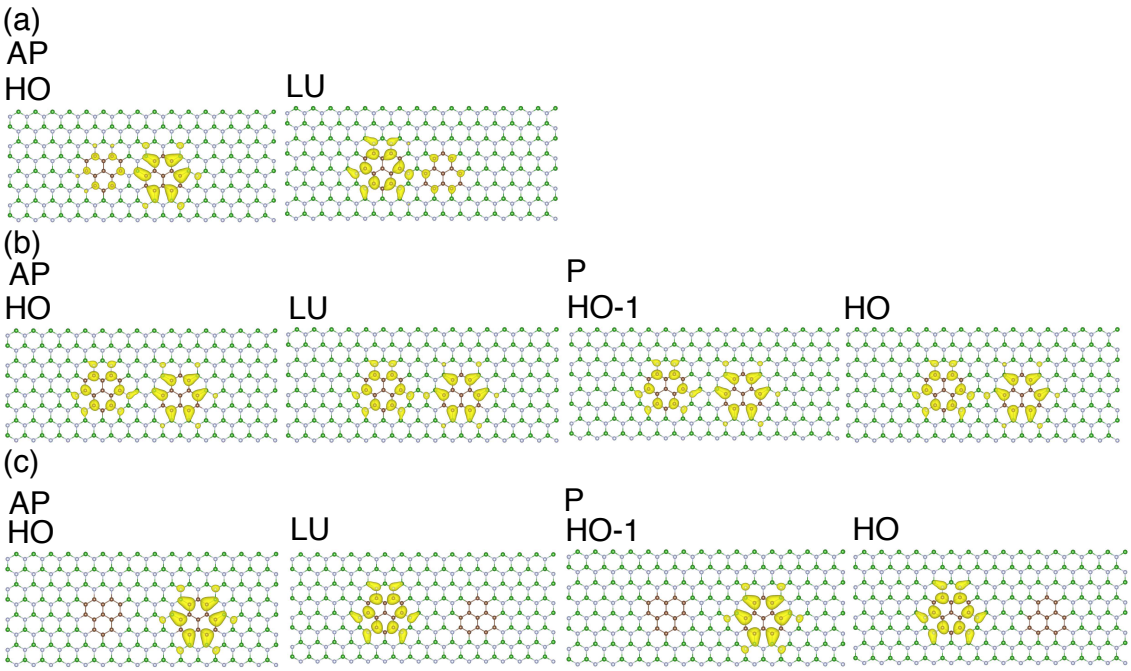

Figure 5.10: Isosurfaces of squared wave functions of antiparallel (AP) and parallel (P) spin coupling states of graphene dots in h-BN with mixed borders and inter-dot spacings of (a) 3.75, (b) 6.25, and (c) 11.25 Å. Brown, gray, and green circles denote C, N, and B atoms, respectively.

Chapter 6

Conclusion

In this thesis, we investigated geometric and electronic structures of 2D networks consisting of sp^2 C atoms using by the first-principle total-energy calculations based on the DFT.

In chapter 3, we investigate geometric and electronic structures of 2D stable C allotropes comprised of pentagonal rings. We found that the sp^2 C sheet has slightly higher total energy than C_{60} and retains its planar structure up to 1000 K, indicating that the sheet is both energetically and kinetically stable. The electronic structure of the sheet is found to be a metal with a flat dispersion band at E_F, leading to spin polarization on the sheet. The polarized electron spin is ferromagnetically aligned and extends throughout the sheet with a spin moment of 0.62 μ_B/nm^2.

In chapter 4, we investigated the geometric and electronic structures of porous graphene networks consisting of phenalenyl and phenyl groups, which are connected alternately with C_3 symmetry via single bonds to form a honeycomb network with an internal degree of freedom. The networks possess both Dirac cones and Kagome flat bands near E_F because the phenalenyl and phenyl form hexagonal and Kagome lattices, respectively. The large spacing between phenalenyl units leads to very slow massless electrons/holes at E_F, the Fermi velocity of which is a hundred times lower than that of graphene, leading to spin polarization on the networks with AF and F ordering as their stable states. Our calculations show the AF state is the ground state whose energy is lower by 14 meV than that of the F state. We also demonstrate that the electronic structure of the 2D networks is sensitive to the rotation of the phenyl units connecting phenalenyl units by changing the π electron network topology.

In chapter 5, we showed the energetics and magnetic properties of two graphene dots with triangular shapes embedded in an h-BN sheet. Our first-principles total-energy calculations show that the graphene dots in h-BN prefer the closest inter-dot spacing as their ground state arrangement. Furthermore, total energy of the heterosheet monotonically increases with increasing inter-dot spacing and immediately becomes saturated at 0.21 and 0.12 eV for NC and BC borders, respectively, at the inter-dot spacing of 7.5 Å. We also find that ferrimagnetic spin polarization occurs on each graphene dot with $S = 1/2$ magnetic moment, which are aligned in singlet and triplet arrangement between two dots under inter-dot spacings of 5.0 Å or larger. The spin polarization energy becomes saturated at approximately 100

meV per graphene dot at an inter-dot spacing of 8.0 Å. The spin-spin interaction J prefers a singlet spin coupling to a triplet one with an energy of 50 meV at an inter-dot spacing of 5.0 Å.

Acknowledgment

I would like to express my greatest appreciation to my supervisor, Professor Susumu Okada, for his continuing guidance and encouragement throughout these works. I am deeply grateful to Professor Takazumi Kawai, Dr. Nguyen Thanh Cuong, Dr. Satoru Konabe, and Dr. Tomoe Yayama for their kind discussions. I also would like to express my appreciation to all the members of the research group under Professor Susumu Okada. Especially, I wish thank Ms. Ayaka Yamanaka for frequent and helpful discussions and advices. I would like to thank laboratory secretary, Ms. Reiko Wada, for her supports.

Bibliography

[1] J.-C. Charlier, X. Gonze, and J.-P. Michenaud, "First-principle study of the electronic properties of graphite", *Phys. Rev. B* **43**, 4579–4589 (1991).

[2] H. W. Kroto, J. R. Heath, S. C. O'Brien, R. F. Curl, and R. E. Smalley, "C_{60}: Buckminsterfullerene", *Nature* **318**, 162–163 (1985).

[3] W. Krätschmer, L. D. Lamb, K. Fostiropoulos, and D. R. Huffman, "Solid C_{60}: anew form of carbon", *Nature* **347**, 354–358 (1990).

[4] S. Iijima, "Helical microtubules of graphitic carbon", *Nature* **354**, 56–58 (1991).

[5] N. Hamada, S.-I. Sawada, and A. Oshiyama, "New one-dimensional conductors: Graphitic microtubules", *Phys. Rev. Lett.* **68**, 1579–1581 (1992).

[6] R. Saito, M. Fujita, G. Dresselhaus, and M. S. Dresselhaus, "Electronic structure of chiral graphene tubules", *Appl. Phys. Lett.* **60 (18)**, 2204–2206 (1992).

[7] K. S. Novoselov, A. K. Geim, S. V. Morozov, D. Jiang, Y. Zhang, S. V. Dubonos, I. V. Grigorieva, and A. A. Firsov, "Electric Field Effect in Atomically Thin Carbon Films", *Science* **306**, 666–669 (2004).

[8] A. K. Geim and K. S. Novoselov, "The rise of graphene", *Nature Mater.* **6**, 183–191 (2007).

[9] A. Yamanaka and S. Okada, "Energetics and electronic structure of graphene nanoribbons under a lateral electric field", *Carbon* **96**, 351–361 (2014).

[10] K. Wakabayashi, M. Fujita, H. Ajiki, and M. Sigrist, "Electronic and magnetic properties of nanographite ribbons", *Phys. Rev. B* **59**, 8271–8282 (1999).

[11] M. Fujita, K. Wakabayashi, K. Nakada, and K. Kusakabe, "Peculiar Localized State at Zigzag Graphite Edge", *J. Phys. Soc. Jpn.* **65**, 1920–1923 (1996).

[12] K. Nakada, M. Fujita, G. Dresselhaus, and M. Dresselhaus, "Edge state in graphene ribbons: Nanometer size effect and edge shape dependence", *Phys. Rev. B* **54**, 17954–17961 (1996).

[13] E. Clar: *The Aromatic Sextet* (John Wiley & Sons, New York, U. S. A.1972)

[14] E. Clar and R. Schoental: *Polycyclic Hydrocarbons* (Springer-Verlag, Berlin, Germany, 1964).

[15] S. Okada, T. Kawai, and K. Nakada, "Electronic structure of graphene with a topological line defect", *J. Phys. Soc. Jpn.* **80**, 013709-1–4 (2011).

[16] P. Y. Huang, C. S. Rulz-Vargas, A. M. van der Zande, W. S. Whitney, M. O. Levendorf, J. W. Kevek, S. Garg, J. S. Alden, C. J. Hustedt, Y. Zhu, J. Park, P. L. McEuen, and D. A. Muller, "Grains and grain boundaries in single-layer graphene atomic patchwork quilts", *Nature* **469**, 389–392 (2011).

[17] S. Okada and A. Oshiyama, "Magnetic Ordering in Hexagonally Bonded Sheets with First-Row Elements", *Phys. Rev. Lett.* **87**, 146803-1–4 (2001).

[18] N. Shima and H. Aoki, "Electronic structure of super-honeycomb systems: a peculiar realization of semimetal/semiconductor classes and ferromagnetism", *Phys. Rev. Lett.* **71**, 4389–4392 (1993).

[19] P. Hohenberg and W. Kohn, "Inhomogeneous electron Gas", *Phys. Rev.* **136**, B864–B871 (1964).

[20] W. Kohn and L. J. Sham, "Self-consistent equations including exchange and correlation effects", *Phys. Rev.* **140**, A1133–A1138 (1965). ", *Appl. Surf. Sci.* **169-170**, 11-15 (2000).

[21] J. P. Perdew and A. Zunger, "Self-interaction correction to density-functional approximations for many-electron systems", *Phys. Rev. B* **23**, 5048–5079 (1981).

[22] D. M. Ceperley and B. J. Alder, "Ground state of the electron gas by a stochastic method", *Phys. Rev. Lett.* **45**, 566–569 (1980).

[23] J. P. Perdew, K. Burke, and M. Ernzerhof, "Generalized gradient approximation made simple", *Phys. Rev. Lett.* **77**, 3865–3868 (1996).

[24] W. E. Pickett, "Pseudopotential methods in condensed matter applications", *Comp. Phys. Rep.* **9**, 115–198 (1989).

[25] N. Troullier and J. L. Martins, "Efficient pseudopotentials for plane–wave calculations", *Phys. Rev. B* **43**, 1993–2006 (1991).

[26] D. Vanderbilt, "Soft self-consistent pseudopotentials in a generalized eigenvalue formalism", *Phys. Rev. B* **41**, 7892–7895 (1990).

[27] M. Otani and O. Sugino, "First-principles calculations of charged surfaces and interfaces: a plane-wave nonrepeated slab approach", *Phys. Rev. B* **73**, 115407-1–11 (2006).

[28] P. W. Fowler and D. E. Manolopoulos: *An Atlas of Fullerenes* (Oxford University Press, Oxford, U. K.,1995).

[29] S. Saito and A. Oshiyama, "Cohesive Mechanism and Energy Bands of Solid C_{60}", *Phys. Rev. Lett.* **66**, 2637–2640 (1991).

[30] S. Saito, S. Okada, S.-I. Sawada, and N. Hamada, "Common Electronic Structure and pentagon pairing in Extractable Fullerenes", *Phys. Rev. Lett.* **75**, 685–688 (1995).

[31] S. Okada and S. Saito, "Number of extractable fullerene isomers and speciality of C_{84}", *Chem. Phys. Lett.* **252**, 94–100 (1996).

[32] S. Okada and S. Saito, "Electronic structure of C_{78} abd C_{78}-graphite cointercalation compound", *J. Phys. Soc. Jpn.* **64**, 2100–2105 (1995).

[33] V. H. Crespi, L. X. Benedict, M. L. Cohen, and S. G. Louie, "Prediction of a pure-carbon planar covalent metal", *Phys. Rev. B* **53**, R13303-R13305 (1996).

[34] E. Ertekin, D. C. Chrzan, and M. S. Daw, "Topological description of the Stone-Wales defect formation energy in carbon nanotubes and graphene", *Phys. Rev. B* **79**, 155421-1–17 (2009).

[35] K. Kusakabe, K. Wakabayashi, M. Igami, K. Nakada, and M. Fujita, "Magnetism of nanometer-scale graphite with edge or topological defects", *Mol. Cryst. Liq. Cryst.* **305**, 445–454 (1997).

[36] S. Okada, K. Nakada, K. Kuwabara, K. Daigoku, and T. Kawai, "Ferromagnetic spin ordering on carbon nanotubes with topological line defects", *Phys. Rev. B* **74**, 121412-1–4(R) (2006).

[37] Y. Morikawa, K. Iwata, and K. Terakura, "Theoretical study of hydrogenation process of formate on clean and Zn deposited Cu(1 1 1) surfaces", *Appl. Surf. Sci.* **169-170**, 11–15 (2001).

[38] A. de Meijere, F. Gerson, P. R. Schreiner, P. Merstetter, and F.-M. Schüngel, "The radical anion of acepentalene", *Chem. Commun.* 2189-2190 (1999).

[39] C. Su, H. Jiang, and J. Feng, "Two-dimensional carbon allotrope with strong electronic anisotropy", *Phys. Rev. B* **87**, 075453-1–5 (2013).

[40] H. Kollmar and V. Staemmler, "A theoretical study of the structure of cyclobutadiene", *J. Am. Chem. Soc.* **99 (11)**, 3583-3587 (1977).

[41] Y. Liu, G. Wang, Q.-S. Huang, L.-W. Guo, and X. Chen, "Structural and electronic properties of T graphene: a two-dimensional carbon allotrope with tetrarings", *Phys. Rev. Lett.* **108**, 225505-1–5 (2012).

[42] S. Okada, M. Igami, K. Nakada, and A. Oshiyama, "Border states in heterosheets with hexagonal symmetry", *Phys. Rev. B* **62**, 9896–9899 (2000).

[43] J. Wu, W. Pisula and K. Müllen, "Graphenes as potential material for electronics", *Chem. Rev.* **107**, 718–747 (2007).

[44] K. Müllen and J. P. Rabe, "Nanographenes as active components of single-molecule electronics and how a scanning tunneling microscope puts them to work", *Acc. Chem. Res.* **41**, 511–520 (2008).

[45] M. Fujihara, Y. Miyata, R. Kitaura, Y. Nishimura, C. Camacho, S. Irle, Y. Iizumi, T. Okazakim, and H. Shinohara, "Dimerization-initiated preferential formation of coronene-based graphene nanoribbons in carbon nanotubes", *J. Phys. Chem. C* **116**, 15141–15145 (2012).

[46] H. E. Lim, Y. Miyata, M. Fujihara, S. Okada, Z. Liu, Arifin, K. Sato, H. Omachi, R. Kitaura, S. Irie, K. Suenaga, and H. Shinohara, "Fabrication and optical probing of highly extended, ultrathin graphene nanoribbons in carbon nanotubes", *ACS Nano* **9**, 5034–5040 (2015).

[47] A. I. Cooper, "Conjugated microporous polymers", *Adv. Mater.* **21**, 1291–1295 (2009).

[48] J. Gao and D. Jiang, "Covalent organic frameworks with spatially confined guest molecules in nanochannels and their impacts on crystalline structures", *Chem. Commun.* **52**, 1498–1500 (2016).

[49] X. Liu, J. Tan, A. Wang, X. Zhang, and M. Zhao, "Electron spin-polarization and spin lattices in the boron- and nitrogen-doped organic framework COF-5", *Phys. Chem. Chem. Phys.* **16**, 23286–23291 (2014).

[50] C. Sánchez-Sánchez, S. Brüller, H. Sachdev, K. Müllen, M. Krieg, H. F. Bettinger, A. Nicolaï, V. Meunier, L. Talirz, R. Fasel, and P. Ruffieux, "On-surfaces synthesis of BN-substitued heteromatic networks", *ACS Nano* **5**, 9228–9235 (2015).

[51] Y. Morita, S. Suzuki, K. Sato, and T. Takui, "Synthetic organic spin chemistry for structurally well-defined open-shell graphene fragments", *Nature Chem.* **3**, 197–204 (2011).

[52] V. Boekelheide and C. E. Larrabee, "An investigation of the preparation and some properties of perinaphthene[1]", *J. Am. Chem. Soc.* **72**, 1245–1249 (1950).

[53] D. H. Reid, "Stable π-electron systems and new aromatic structures", *Tetrahedron* **3**, 339–352 (1958).

[54] K. Nakasuji, M. Yamaguchi, I. Murata, K. Yamaguchi, T. Fueno, H. Ohya-Nishiguchi, T. Sugano, and M. Kinoshita, "Synthesis and characterization of phenalenyl cations, radicals, and anions having donor and acceptor substituents: three redox states of modified odd alternant systems", *J. Am. Chem. Soc.* **111**, 9265–9267 (1989).

[55] Z. Sun and J. Wu, "Open-shell polycyclic aromatic hydrocarbons", *J. Mater. Chem.* **22**, 4151–4160 (2012).

[56] T. Kubo, "Phenalenyl-based open-shell polycyclic aromatic hydrocarbons", *Chem. Rec.* **15**, 218–232 (2015).

[57] T. Kubo, A. Shimizu, M. Uruichi, K. Yakushi, M. Nakano, D. Shiomi, K. Sato, T. Takui, Y. Morita, and K. Nakasuji, "Singlet biradical character of phenalenyl-based Kekule' hydrocarbon with naphthoquinoid structure", *Org. Lett.* **9**, 81–84 (2007).

[58] Z. Mou, K. Uchida, T. Kubo, and M. Kertesz, "Evidence of σ- and π-dimerization in a series of phenalenyls", *J. Am. Chem. Soc.* **136**, 18009–18022 (2014).

[59] Z-H. Cui, A. Gupta, H. Lischka, and M. Kertesz, "Concave or convex π-dimers: the role of the pancake bond in substituted phenalenyl radical dimers", *Phys. Chem. Chem. Phys.* **17**, 23963–23969 (2015).

[60] N.-T. Cuong, M. Otani, and S. Okada, "Semiconducting electronic property of graphene adsorbed on (0001) surfaces of SiO_2", *Phys. Rev. Lett.* **106**, 106801-1–4 (2011).

[61] H. Yuan, H. Shimotani, J. Ye, S. Yoon, H. Allah, A. Tsukazaki, M. Kawasaki, and Y. Iwasa, "Electrostatic and electrochemical nature of liquid-gated electric-double-layer transistors based on oxide semiconductors", *J. Am. Chem. Soc.* **132**, 18402–18407 (2010).

[62] J. Kouvetakis, T. Sasaki, C. Chen, R. Hagiwara, M. Lerner, K. M. Krishnan, and N. Bartlett, "Novel aspects of graphite intercalation by fluorine and fluorides and new B/C, C/N and B/C/N materials based on the graphite Network", *Synth. Metals* **34**, 1–7 (1989).

[63] K. M. Krishnan, "Structure of newly synthesized BC_3 films", *Appl. Phys. Lett.* **58**, 1857–1859 (1991).

[64] D. Tománek, R. M. Wentzcovitch, S. G. Louie, and M. L. Cohen, "Calculation of electronic anti structural properties of BC_3", *Phys. Rev. B* **37**, 3134–3136 (1988).

[65] Y. Miyamoto, A. Rubio, S. G. Louie, and M. L. Cohen, "Electronic properties of tubule forms of hexagonal BC_3", *Phys. Rev. B* **50**, 18360–18366 (1994).

[66] H. Nozaki and S. Itoh, "Structural stability of BC_2N", *J. Phys. Chem. Solids* **57**, 41–49 (1996).

[67] M. Benkraouda, "Electronic properties of a new structure of BC_2N and its intercalation with magnesium: possibility for a new high-Tc superconductor", *J. Surperco.* **15**, 650–662 (2002).

[68] A. Y. Liu, R. M. Wentzcovitch, and M. L. Cohen, "Atomic arrangement and electronic structure of BC_2N", *Phys. Rev. B* **39**, 1760–1765 (1989).

[69] S. M. Kim, A. Hsu, P. T. Araujo, Y.-H. Lee, T. Palacios, M. Dresselhaus, J.-C. Idrobo, K. K. Kim, and J. Kong, "Synthesis of patched or stacked graphene and hBN flakes: A route to hybrid structure discovery", *Nano Lett.* **13**, 933–941 (2013).

[70] J. Park, J. Lee, L. Liu, K. W. Clark, C. Durand, C. Park, B. G. Sumpter, A. P. Baddorf, A. Mohsin, M. Yoon, G. Gu, and A.-P. Li, "Spatially resolved one-dimensional boundary states in graphene-hexagonal boron nitride planar heterostructures", *Nature Commun.* **5**, 5403-1–6 (2014).

[71] C. Tönshoff, M. Müller, T. Kar, F. Latteyer, T. Chassé, K. Eichele, and H. F. Bettinger, "B_3N_3 borazine substitution in hexa-peri-hexabenzocoronene: computational analysis and scholl reaction of hexaphenylborazine", *Chem. Phys. Chem.* **13**, 1173–1181 (2012).

[72] C. Sánchez-Sánchez, S. Brüller, H. Sachdev, K. Müllen, M. Krieg, H. F. Bettinger, A. Nicolaï, V. Meunier, L. Talirz, R. Fasel, and P. Ruffieux, "On-surface synthesis of BN-substituted heteroaromatic networks", *ACS Nano* **9**, 9228–9235 (2015).

[73] T. Gao, X. Song, H. Du, Y. Nie, Y. Chen, Q. Ji, J. Sun, Y. Yang, Y. Zhang, and Z. Liu, "Temperature-triggered chemical switching growth of in-plane and vertically stacked graphene-boron nitride heterostructures", *Nature Commun.* **6**, 6835 (2015).

[74] L. Ci, L. Song, C. Jin, D. Jariwala, D. Wu, Y. Li, A. Srivastava, Z. F. Wang, K. Storr, L. Balicas, F. Liu, and P. N. Ajayan, "Atomic layers of hybridized boron nitride and graphene domains", *Nature Mater.* **9**, 430–435 (2010).

[75] Y. Gao, Y. Zhang, P. Chen, Y. Li, M. Liu, T. Gao, D. Ma, Y. Chen, Z. Cheng, X. Qiu, W. Duan, and Z. Liu, "Toward single-layer uniform hexagonal boron nitride-graphene patchworks with zigzag linking edges", *Nano Lett.* **13**, 3439–3443 (2013).

[76] Y. Liu, S. Bhowmick, and B. I. Yakobson, "BN white graphene with "colorful" edges: the energies and morphology", *Nano Lett.* **11**, 3113-3116 (2011).

[77] S. Bhowmick, A. K. Singh, and B. I. Yakobson, "Quantum dots and nanoroads of graphene embedded in hexagonal boron nitride", *J. Phys. Chem. C* **115**, 9889–9893 (2011).

[78] S. Okada, M. Igami, K. Nakada, and A. Oshiyama, "Border states in heterosheets with hexagonal symmetry", *Phys. Rev. B* **62**, 9896–9899 (2000).

[79] Y. Zhou, Z. Wang, P. Yang, and F. Gao, "Novel electronic and magnetic properties of graphene nanoflakes in a boron nitride layer", *J. Phys. Chem. C* **116**, 7581–7586 (2012).

[80] I. Hamada and M. Otani, "Comparative van der Waals density-functional study of graphene on metal surfaces", *Phys. Rev. B* **82**, 153412-1–4 (2010).

[81] M. Otani and S. Okada, "Gate-controlled carrier injection into hexagonal boron nitride", *Phys. Rev. B* **83**, 073405-1–4 (2011).

List of Publications

1. Mina Maruyama and Susumu Okada, "Two-dimensional sp^2 carbon networks of fused pentagons", *Jpn. J. Appl. Phys.* **53**, 06JD02-1–4 (2014).

2. Mina Maruyama and Susumu Okada, "Geometric and electronic structures of polymerized C_{32} fullerenes: Electronic structure tuning by fullerene and carbon nanotube filling", *Jpn. J. Appl. Phys.* **54**, 06FF02-1–4 (2015).

3. Mina Maruyama, Nguyen Thanh Cuong, and Susumu Okada, "Geometric and electronic structures of two-dimensional networks of fused C_{36} fullerenes", *J. Phys. Soc. Jpn.* **84**, 084706-1–6 (2015).

4. Mina Maruyama and Susumu Okada, "Magnetic properties of graphene quantum dots embedded in h-BN sheet", *J. Phys. Chem. C* **120**, 1293–1302, (2016).

5. Mina Maruyama, Nguyen Thanh Cuong, and Susumu Okada, "Coexistence of Dirac cones and Kagome flat bands in a porous graphene", *Carbon* **109**, 755–763 (2016).